Doctoral theses at NTNU, 2020:56

Petros Tesfamichael Yemane

Ultrasound for the delivery of a nanocarrier across biological barriers in tumors: impact of cavitation and acoustic radiation force

Doctoral thesis

Petros Tesfamichael Yemane

Doctoral theses at NTNU, 2020:56

NTNU
Norwegian University of
Science and Technology

NTNU
Norwegian University of Science and Technology
Thesis for the Degree of
Philosophiae Doctor
Faculty of Natural Sciences
Department of Physics

ISBN 978-82-326-4466-7 (printed ver.)
ISBN 978-82-326-4467-4 (electronic ver.)
ISSN 1503-8181

NTNU
Norwegian University of
Science and Technology

Petros Tesfamichael Yemane

Ultrasound for the delivery of a nanocarrier across biological barriers in tumors: impact of cavitation and acoustic radiation force

Thesis for the Degree of Philosophiae Doctor

Trondheim, February 2020

Norwegian University of Science and Technology
Faculty of Natural Sciences
Department of Physics

NTNU
Norwegian University of
Science and Technology

NTNU
Norwegian University of Science and Technology

Thesis for the Degree of Philosophiae Doctor

Faculty of Natural Sciences
Department of Physics

ISBN 978-82-326-4466-7 (printed ver.)
ISBN 978-82-326-4467-4 (electronic ver.)
ISSN 1503-8181

Doctoral theses at NTNU, 2020:56

Printed by NTNU Grafisk senter

Ultrasound for the delivery of a nanocarrier across biological barriers in tumors: impact of cavitation and acoustic radiation force.

Petros Tesfamichael Yemane

PhD thesis
Trondheim, February 2020

Norwegian University of Science and Technology
Faculty of Natural Science

Department of Physics

Abstract

Cancer is one of the world's leading cause of death, even though immense progress has been made in the field of cancer research during the last few decades. Although conventional chemotherapy is still one of the most important treatment modalities, it is limited by its lack of specificity and the insufficient accumulation of chemotherapeutic agents in deadly tumor cells. Drug nanocarriers can enable more targeted delivery to minimize side effects on healthy tissue and to improve efficacy. Cancer therapy using this approach is limited, however, by uneven drug delivery through blood vessels, heterogeneous drug transport into the tumor interstitium from the vascular compartment, and obstructed transport through the tumor interstitium to the target cells. Recently, ultrasound (US) has been demonstrated as a noninvasive therapeutic modality and has shown promising results in enhancing therapeutic efficacy when used in combination with drug nanocarriers. Through various mechanisms, US alone or combined with MBs can produce a variety of biological effects on tissue that can result in transiently enhanced permeability of biological barriers, including blood vessel walls, the extracellular matrix (ECM), cell membranes, and the blood-brain barrier, facilitating improved drug delivery efficacy in tumor sites. Despite the promise of US by itself and/or combined with MB-enhanced drug delivery, a full understanding of how US alone and alongside injected MBs improves the therapeutic effect of drugs against tumors is lacking.

In this thesis, a nanocarrier delivery study assessing the performance of the combination of US with nanoparticles (NPs), NP-stabilized microbubbles (MBs) (NPMB) or commercial contrast agents (SonoVue) in overcoming the natural barriers, including blood vessel walls and the ECM, to the extravasation and transport of NPs as a model therapeutic agent is conducted. US-induced cavitation in the vasculature and the behavior of the nanoscale particles injected together with MBs were observed in real time during US exposure with an optoacoustic setup. The recorded images revealed the importance of the acoustic, MB, and vascular parameters. We found significant extravasation and penetration of NPs under the range of pressures applied, and in general, the extravasation took place at vessel branching points. A higher mechanical index is required to achieve extravasation from smaller blood vessels than from larger vessels. Moreover, US alters NP flow velocity and blood flow direction. Furthermore, the penetration depth and rate of nanoscale particles in the ECM increased with increasing mechanical index. In addition, we investigated the impact of US and MBs on the ECM and found insignificant changes in the collagen content and structure for the acoustic pressures applied.

The acoustic radiation force (ARF) can translate particles or tissues; thus, the potential of ARF for affecting the transport and distribution of the NPs in solid tumors and in collagen gel was investigated. We found that the mechanical effect of US through ARF and acoustic streaming improved the transport of NPs across the blood vessels and enhanced the microdistribution of NPs in the tumor ECM. This penetration of the NPs might facilitate enhanced therapeutic efficacy against tumor sites. However, we found no effect of ARF on the transport of NPs in the tissue-mimicking collagen gel phantom, whereas a large deformation of the collagen gel was found for the acoustic parameters

tested. ARF could play an important role in overcoming the barriers created by the vasculature and ECM if the US parameters are well optimized.

Using several experimental investigations, important insights were gained concerning the mechanisms involved in the nonthermal effect of US on enhancing drug delivery. Interestingly, the results are highly useful for understanding the mechanisms, optimizing the US-mediated delivery of NPs and supplying important insights for future studies. It is also noted that the US-mediated drug delivery of nanocarriers across biological barriers can enhance cancer treatment.

Acknowledgments

This thesis submitted to the Norwegian University of Science and Technology (NTNU) as part of the requirement for the degree of *philosphiae doctor*. The work presented in the thesis has been done from 2015 to 2019 at the Department of Physics, NTNU, in collaboration with the Department of Circulation and Diagnostic Imaging, NTNU, and SINTEF. Funding has been provided by the Norwegian Research Council.

This work resented herein would not have been possible without valuable contributions from many people, who I would like to acknowledge.

First of all, I would like to thank my supervisor, Catharina, for allowing me to do this work; for your immense guiding, support and mentorship throughout these years with your contagions enthusiasm and optimism. Thanks for generously giving your time and advice as I learn to do research. It was a great pleasure working with you.

Special thanks to my co-supervisor Bjørn, thank you for your assistance and support, and you were the one who introduced to me to this exiting ultrasound field. Thanks for your contribution with your expertise in ultrasound and in mathematical modeling and your insightful discussions about the simulations. My co-supervisor Rune, thank you for assistance and contribution with your expertise in ultrasound, and the valuable input to our discussion has been valuable in my work.

Astrid B and Kristin, thank you both of you for all your support and help in the labs both for participating in doing the experiments and keeping the lab running smoothly. Your competence and expertise have also been valuable to my work. I would also like to thank Robin and Johannes for your valuable input and discussion for the simulations.

To other previous and present group members, co-authors and master students, thanks to you Sofie, Sigrid, Mercy, Ola, Mia, Annemieke, Andreas, Yrr, Sverre, Sylvie Lelu and Einar, for all your contribution to this work. I would also like to mention Sjoerd, Stein Martin, Habib, Marieke, Melina, Astrid H and Ellen. I have been fortunate enough to work with you over the years, thanks for creating a good atmosphere in the group. I would also to thank for my colleagues at the Biophysics group.

Department of physics, Department of Circulation and Medical Imaging, Department of Comparative Medicine, Cellular and Molecular Imaging Core Facility, and NTNU are acknowledged for technical assistance, access to equipment and care of animals in various experiments. The Norwegian Research Council is acknowledged for financial support.

I would like also to thanks to my family and friends who support me throughout this wonderful journey. And last but not least, my wife, Elsa, my kids, Yosief and Arsema, thank you for everything. It truly wouldn't have been possible without you.

List of papers included in the thesis

Publications:

1. **Effect of ultrasound on the vasculature and extravasation of nanoscale particles imaged in real time**.
   Petros T. Yemane, Andreas Åslund, Sofie Snipstad, Astrid Bjørkøy, Kristin Grendstad, Sigrid Berg, Yrr Mørch, Sverre H. Torp, Rune Hansen, Catharina de Lange Davies.
   Ultrasound in Medicine & Biology 2019; 45:3028-41.
   PY, AÅ, and CD designed the experimental setup and the experiments, PY experimented and analyzed the images and results. AÅ, SS, SB, and RH participated in the experimental work and in analyzing results. AB participated in the experimental work, especially the multiphoton microscopy. KG participated in the experimental work, implanting the dorsal window chamber. YM optimized and synthesized nanoparticles and microbubbles for the experiments, and contributed to the manuscript. ST analyzed the histological sections, contributed to the manuscript. PY wrote the manuscript together with CD, AÅ, SS, SB, RH, YM and AB. All authors have read and approved the final manuscript.

2. **Effect of ultrasound and microbubbles on the collagen network in solid tumors**
   Petros T. Yemane, Astrid Bjørkøy , Kristin Grendstad, Einar Sulheim, Sofie Snipstad, Catharina de Lange Davies
   Manuscript in preparation.
   PY, KG, AB, CD designed the experiments. PY conducted the experiments, analyzed the images and results. AB participated in the experimental work, especially the multiphoton microscopy. KG participated in the experimental work, implanting a skin flap model. PY wrote the manuscript together with AB, ES, SS, and CD. All authors have read and approved the final manuscript.

3. **Effect of acoustic radiation force on the distribution of nanoparticles in solid tumors.**
   Mercy Afadzi, Ola Finneng Myhre, Petros T. Yemane, Siri Vea, Astrid Bjørkøy, Sverre H. Torp,, Annemieke van Wamel, Sylvie Lelu, Bjørn Angelsen, Catharina de Lange Davies
   Submitted to IEEE Transactions on Ultrasonics, Ferroelectrics, and Frequency control.
   MA, OM, SV, AW, SL, BA, CD designed the experiments. MA, OM, SV conducted the experiments, analyzed the images and results. PY participated in the analysis of the images and results, conducted in the temperature measurement. MA wrote the manuscript together with OM, PY and CD. ST analyzed the histological sections, contributed to the manuscript. PY and OM did the simulations. All authors

have read and approved the final manuscript.

4. **Effect of acoustic radiation force on displacement of nanoparticles in collagen gels.**
Mia Kvåle Løvmo*, Petros T. Yemane*, Rune Hansen, Robin Cleveland, Bjørn Angelsen, Catharina de Lange Davies.
Manuscript in preparation.
* Equal contribution.
ML, PY, BA, RC, CD designed the experiments. ML conducted the ultrasound experiments, analyzed the images and results. PY conduced the indentation experiments, analyzed the results, and did the simulations. PY wrote the manuscript together with ML, RH, RC, and CD. All authors have read and approved the final manuscript.

Other related conference publications and posters not included in this thesis

1. **The Effect of Sonication on Extravasation and Distribution of Nanoparticles and Dextrans in Tumor Tissue Imaged by Multiphoton Microscopy.**
Yemane, Petros T., Åslund, Andreas, Sæterbø, Kristin Grendstad, Bjørkøy, Astrid, Snipstad, Sofie, van Wamel, Annemieke, Berg, Sigrid, Mørch, Ýrr Asbjørg, Hansen, Rune, Angelsen, Bjørn Atle Johan, Davies, Catharina de Lange.
Proceedings - IEEE Ultrasonics Symposium. 2018, 4 pp.
DOI:10.1109/ULTSYM.2018.8580082.

2. **Sonoporation enhances delivery of nanomedicine for improved cancer treatment**.
Snipstad, Sofie; Yemane, Petros Tesfamichael; Åslund, Andreas; Grendstad, Kristin; Berg, Sigrid; Mørch, Ýrr Asbjørg; Bjørkøy, Astrid; Sulheim, Einar; Hansen, Rune; van Wamel, Annemieke; Torp, Sverre Helge; Davies, Catharina de Lange.
11th European and Global Summit for Clinical Nanomedicine, Targeted Delivery and Precision Medicine (CLINAM); 2018-09-02 - 2018-09-05 NTNU

3. **Extravasation and distribution of nanoparticles and 2MDa dextran in tumor imaged by multiphoton microscopy during ultrasound sonication.**
Yemane, Petros Tesfamichael; Åslund, Andreas; Sæterbø, Kristin G.; Bjørkøy, Astrid; Snipstad, Sofie; van Wamel, Annemieke; Berg, Sigrid; Mørch, Ýrr Asbjørg; Hansen, Rune; Angelsen, Bjørn Atle Johan; Davies, Catharina de Lange.
CIUS spring conference 2018; 2018-04-25 - 2018-04-26 NTNU.

4. **Effect of acoustic radiation force on the distribution of nanoparticles in solid tumors.**
Afadzi, Mercy; Myhre, Ola Finneng; Yemane, Petros Tesfamichael; Bjørkøy, Astrid; Vea, Siri; van Wamel, Annemieke; Berg, Sigrid; Hansen, Rune; Angelsen, Bjørn

Atle J.; Davies, Ruth Catharina de Lange.
ISTU 2016; 2016-03-14 - 2016-03-16 NTNU.

5. **Simulation of ultrasound radiation force: for transport of drugs and nanoparticles in tumors.**
Yemane, Petros Tesfamichael; Angelsen, Bjørn Atle J.; Kvam, Johannes; Afadzi, Mercy; Myhre, Ola Finneng; Davies, Ruth Catharina de Lange.
The 8th National PhD Conference in Medical Imaging 2016 NTNU UiO.

6. **Ultrasound radiation force transport of drugs and nanoparticles in tumors: characterization of transducer and simulation of ultrasound waves and radiation force.**
Yemane, Petros Tesfamichael; Angelsen, Bjørn Atle Johan; Davies, Catharina De Lange.
The 7th National PhD Conference in Medical Imaging - NTNU; 2015-10-17 - 2015-10-18 NTNU.

List of Abbreviations

ARF	Acoustic radiation force
ECM	Extracellular matrix
EPR	Enhanced permeability and retention
FITC	Fluorescein isothiocyanate
FUS	Focused ultrasound
HES	Hematoxylin, eosin and saffron
HIFU	High-intensity focused ultrasound
MB	Microbubble
MI	Mechanical index
MRI	Magnetic resonance imaging
NP	Nanoparticle
NPMB	Nanoparticle-stabilized microbubble
PEBCA	Poly(ethylbutyl cyanoacrylate)
PEG	Polyethylene glycol
RES	Reticuloendothelial system
SHG	Second-harmonic generation
UCA	Ultrasound contrast agent
US	Ultrasound

Contents

1 INTRODUCTION

1.1 Background

Cancer is a group of diseases resulting from uncontrolled cell growth with the potential to invade or spread to other parts of the body. These tumors are called malignant tumors, in contrast to benign tumors, which do not spread to other parts of the body. According to the World Health Organization, cancer is one of the world's leading causes of death and is accountable for an estimated 9.6 million deaths in 2018 [1]. This high mortality primarily results from a lack of effective therapy against many cancer types. The most routinely used treatments of cancer include chemotherapy, radiation therapy, and surgery. Unfortunately, the effectiveness of current cancer treatments depends on the early diagnosis and the type of cancer. Both chemotherapy and radiation therapy lack specificity towards the tumor tissue, and surgical intervention cannot always be successful without a certain risk of complications within the surrounding healthy tissue or with removing the whole cancer tissue. Hence, the development of an alternative treatment method that minimizes the unwanted side effects on healthy tissue is desired.

Chemotherapy is a systemic treatment and is used to treat metastatic malignancies, inoperable tumors, circulating tumor cells and radiotherapy-resistant tumors. Chemotherapeutic drugs are administered systematically to the body to kill cancerous cells. Since chemotherapeutic drugs are distributed throughout the body, they affect both healthy and cancer cells [2]. Moreover, chemotherapeutics also have an unfavorable biodistribution in tumors and are generally rapidly removed from the body by renal filtration due to their low molecular weight [3–5]. Thus, the dose achievable within the solid tumor is limited, resulting in far from optimal treatment. Although conventional chemotherapy is still one of the most important treatment modalities, an alternative drug delivery system that overcomes the lack of specificity and the insufficient dose of conventional chemotherapeutic agents is needed.

Improvements in the therapeutic index (ratio of therapeutic benefit to side effects) of drugs have been sought by encapsulating chemotherapeutic drugs in nanocarriers. Such a delivery system could minimize exposure to healthy cells and simultaneously increase the concentration of chemotherapeutics specifically at the tumor site; hence, it can result in enhanced treatment efficacy with reduced side effects [3]. However, nanocarrier-based cancer treatment is not always successful, and an improved therapeutic response has not been demonstrated in the clinic [5, 6]. For example, a recent meta-analysis of the last ten years of publications found that only 0.7% of the injected NPs accumulated in the tumor [7]. This finding indicates that sufficient amounts of drugs may not reach all parts of the tumor to kill all cancer cells. It has been reported that drugs and macromolecular anticancer agents (nanocarriers, antibodies, and viral vectors) administered intravenously face several hindrances created by the tumor microenvironment before reaching the tumor cells, thereby complicating efficient delivery. The aspects of the tumor microenvironment that complicate efficient delivery include the vasculature, interstitial fluid pressure, and multifactorial increase in the composition of the extracellular matrix (ECM) [6, 8–12]. Having a specific nanosize or functionality alone might not be enough to guarantee good

drug delivery to target tumors. The tumor microenvironment is too complex to overcome [6, 13]; thus, a strategy for overcoming these barriers either by modifying the physicochemical properties of a drug or nanocarrier, such as molecular weight, shape, or charge, or by modulating the tumor microenvironment itself to enhance the delivery and effectiveness of drugs in tumors is needed.

Different approaches have been explored to increase the tumor accumulation and cellular uptake of drugs and drug delivery systems [14–16]. In recent years, in addition to drug-encapsulating nanocarrier strategies, nanocarriers responsive to locally applied external physical stimuli, such as ultrasound (US) [17–20], light [21] and magnetic fields [22], have been developed to deliver drugs or genes to targeted tumor locations. Among these methods, due to its nonionization and noninvasive nature and its potential to reach considerable depths inside the body with high spatial precision compared to most external stimuli, US has attracted much attention for such purposes in recent years [23]. US with or without US contrast agents (UCAs) has shown its potential for enhancing the delivery of drugs and drug carriers to the whole tumor with drug delivery systems. US exposure in the presence or absence of MBs has been previously used in several preclinical applications in small animals [24–28]. Importantly, US alongside MBs was used recently in clinical trials to investigate its feasibility in the treatment of pancreatic and liver cancer patients [29, 30]. However, although various mechanisms have been proposed, the exact mechanisms remain to be resolved.

1.2 Nanocarriers in dug delivery

A nanocarrier is a nanomaterial composite that is used as a transport module for another substance, such as a drug or an imaging agent, to specific targeted regions. Since the advancement of nanotechnology, multifunctional nanocarriers have been developed for such applications. They have improved the diagnostics and therapy of various diseases by incorporating contrast agents for imaging and drugs for therapy [31–33]. For clinical use, nanocarriers should be made from a material that is biocompatible (nontoxic and non-immunogenic), well characterized, easily functionalized and preferably biodegradable. Some of the commonly used types of nanocarriers include liposomes, polymeric nanoparticles (NPs), micelles, antibodies, and microbubbles (MBs). They are designed with various materials, such as polymers, lipids, and proteins, and with different sizes, typically from 50-300 nm [34]. Drugs, fluorescent dyes, contrast agents or targeting ligands can be encapsulated or bound to their surface. A schematic overview of a multifunctional NP, as an example of a nanocarrier platform, is illustrated in Figure 1.

Nanocarriers have been shown to offer many advantages over free drugs if they are designed in such a way to prevent rapid degradation in the circulation and rapid renal clearance [2]. Based on the enhanced permeability and retention (EPR) effect (see section 1.3 for a detailed description of the EPR effect), nanocarriers may extravasate through the leaky blood vessels in tumors, where they are preserved due to a lack of lymphatic drainage [2]. In addition, if they are designed to be responsive to internal or external stimuli, delivery of the drugs and nanocarriers into the target regions can be enhanced via nanocarriers releasing their contents upon stimulation [35, 36] and/or

via external stimuli (e.g., US alone or combined with MBs) manipulating the biological barriers [17–19, 37]. Several therapeutic nanocarriers have been approved for clinical use [38]. However, currently, there are only a few clinically approved nanocarriers that incorporate molecules for selectively binding or targeting cancer cells [2].

1.2.1 Polymeric NPs

NPs have been widely used as nanocarriers in recent years, and polymers are the most promising and commonly explored materials for synthesizing NPs. The main characteristic that gives polymeric NPs advantages over other carriers is their ease of synthesis, high therapeutic agent loading capacity, biodegradability, biocompatibility, and improved reproducibility[39]. They can be synthesized for multiple functionalities by combining tumor-targeting agents (such as binding small peptides and antibodies), tumor imaging agents (encapsulation of metals such as iron oxide, gold, and gadolinium as MRI or fluorescent probes for optical imaging) and tumor therapeutics (encapsulation of anticancer drugs). Polymeric NPs made for drug delivery have shown significant therapeutic potential in recent years [33, 35, 39]. Therapeutic agents can be dissolved, entrapped, encapsulated or attached to the NP matrix (Figure 1). The NPs can be made slowly degradable, stimuli-responsive (biological, mechanical or thermal triggering source such PH, light, US), and even targeted, for example, by conjugating them with specific ligands that interact with a receptor that is characteristic of the area of interest. Many multifunctional polymeric NPs are now in various stages of preclinical and clinical development [34, 38, 40, 41].

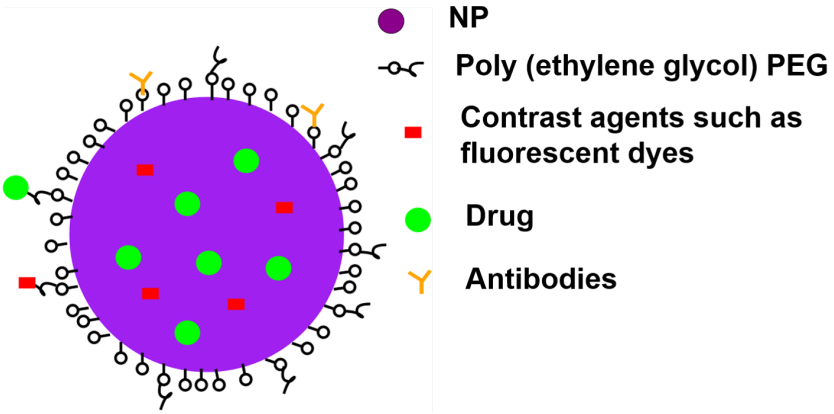

Figure 1: A schematic overview of a multifunctional NP platform.

1.2.2 Poly(ethylbutyl cyanoacrylate) (PEBCA) NPs

In this thesis, a polymeric NP formulation that consists of PEBCA NPs was used. They are synthesized by miniemulsion polymerization of alkyl cyanoacrylate monomers commonly used in medicine as tissue glues. The monomers are hydrophobic; hence, PEBCA NPs are well suited for the encapsulation of hydrophobic drugs [42].

A polyethylene glycol (PEG) coating increases NP circulation time by decreasing excretion by the reticuloendothelial system (RES) [6]. The bioavailability of NPs for imaging and therapy is increased by minimizing their accumulation in the liver and spleen. The effect of PEG on increasing the hydrophilicity of the agent also makes NPs more soluble in body fluids [6]. Moreover, the formulation has the potential to encapsulate dyes, hydrophilic drugs for therapy, or magnetic resonance imaging (MRI) contrast agents for imaging. This particle formulation can also be endowed with multifunctionality by extending the NPs' ability to encapsulate gas and thereby stabilized MBs that can serve as contrast agents or cavitation nuclei (see section 1.7.2) [42].

1.3 Targeted drug delivery

Targeted drug delivery of chemotherapeutics is an emerging area in the field of cancer treatment research. Several approaches, such as passive targeting, active targeting, and triggered drug delivery, are currently being evaluated to achieve local delivery to tumor cells [3, 4, 14, 20].

Passive targeting is one of the most common approaches for targeted delivery of drugs to tumors and benefits from the EPR effect. The EPR effect enables the accumulation of nanocarriers in tumor tissue to a much greater extent than in normal tissues because tumors have leaky blood vessels and poor lymphatic drainage. The rapid formation of abnormal blood vessels (angiogenesis) increases the permeability of the blood vessels in the tumor, allowing extravasation of nanocarriers, and the dysfunctional lymphatic drainage in tumors continues to retain the accumulated nanocarriers and allows them to release drugs locally into the tumor cells [2]. A pore cutoff size ranging between 380 nm and 780 nm has been observed in a large number of tumors [43]. However, due to the heterogeneity of the tumor vasculature within and among tumor types, the existence and clinical application of the EPR effect in humans are in doubt [5, 44–46].

Another approach that makes use of the EPR effect for improving the specificity of the drugs is active targeting. In this approach, drug delivery systems can actively bind to and subsequently be internalized into tumor cells using specific antibodies or other ligands that recognize tumor-associated receptors, which are either uniquely expressed or overexpressed on the target cells relative to normal cells [2, 5, 44]. Since ligand-receptor interactions are highly selective, this approach could allow more precise targeting of the region of interest, and it minimizes the undesired and strong side effects of cancer therapy. However, despite benefiting from the EPR effect, the transport of NPs (or nanocarriers) from the vasculature into tumors is still suboptimal [5–7].

The third approach for increasing the specificity is the use of triggered drug delivery with stimuli-responsive nanocarriers or modulation of the microenvironment by an ex-

ternal stimulus [15, 47], as described in sections 1.1 and 1.2. In this thesis, the focus is more on US-mediated modulation of the microenvironment for enhancing the transport of nanocarriers and (to some extent) for releasing therapeutic agents from nanocarriers to improve the delivery of nanomedicines.

1.4 Barriers to drug delivery

Most solid tumors are composed of proliferating tumor cells, angiogenic vessels and ECM, which are different from healthy tissue. Oftentimes, less than half the volume of a tumor is occupied by cancer cells [48]. The remaining volume is occupied by blood vessels (1-10 % of the tumor volume) and the interstitium [48]. After chemotherapeutic drugs and nanocarriers are administered intravenously, they travel through the bloodstream to reach their targets. To destroy the tumor completely, the therapeutic agents must distribute throughout the tumor with a high enough dose and enter into target cells. Hence, they have to pass several biological barriers, including the vasculature, interstitium, cell membrane, and others, to reach the target [8, 49–51]. An illustrated overview of the normal and tumor microenvironments and the physical barriers to drug delivery is shown in Figure 2.

1.4.1 Vasculature

The vasculature plays a crucial role in tumor growth and metastasis and drug delivery. One of the major barriers to delivery of the administered drug and nanocarriers is the vasculature. Drugs and drug carriers must travel through the circulation and extravasate from the vasculature to reach the tumor cells. However, a tumor blood vessel is highly heterogeneous in distribution and has several abnormalities in comparison with normal vessels, often including relatively atypical branching, organization, diameter, and length [33, 52–54]. These abnormal organizations and structures of the tumor vasculature result in torturous and leaky vessels and rather heterogeneous blood flow, leaving parts of tumors that are very poorly perfused [48]. In addition, proliferating tumor cells can generate solid stress on the blood vessel that will impair blood flow [49]. Compared to the distance from the blood vessels in normal tissue, the mean distance between the tumor cells and the blood vessels is increased, leading to a reduction in blood vessel density and limiting the access of drugs to distant tumor cells. Hence, for drug delivery systems, the first barrier to overcome to realize the delivery of uniform and sufficient levels of anticancer agents to cancer cells is the tumor vasculature.

Once chemotherapeutic drug nanocarriers have been delivered intravenously, the permeability of the vasculature walls is critical for delivering the drug to the target tissue. The permeability of the tumor vessels is shown to be higher than that of normal vessels, but these vessels are heterogeneous with abnormal distribution, leaving avascular spaces of varying sizes [55].

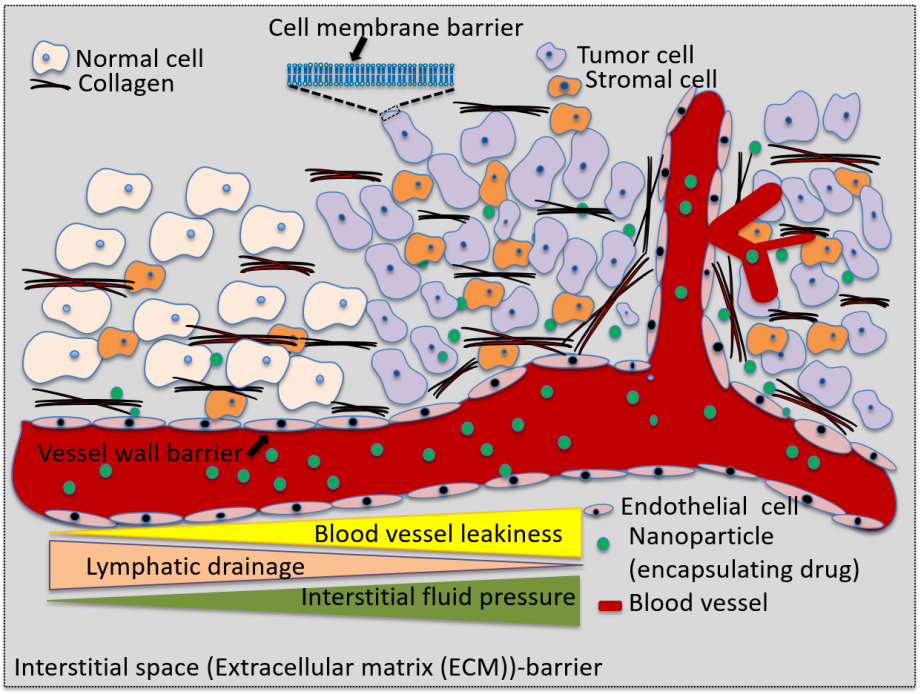

Figure 2: The normal tissue has narrow vessel pores and lower cell density, whereas tumors have relatively leaky blood vessels with dysfunctional lymphatic drainage, higher interstitial fluid pressure, and higher cancer and stromal cell density. The tumor vessels also have wide and irregular pore sizes, and tumors undergo angiogenesis. This figure also illustrates the obstacles to delivery in tumors, including the blood vessel walls, the interstitium, and the cell membranes.

1.4.2 Extracellular matrix (ECM)

Another barrier that can limit the interstitial transport of drug carriers and, as a result, prevent the sufficient and uniform distribution of anticancer agents is the ECM. After crossing the blood vessel wall, the drug carriers must travel through the tumor ECM and enter the target cancer cells. The ECM is a structure that surrounds cancer cells and can separate them from blood vessels. It provides essential physical scaffolds to maintain tissue structure as well as various biochemical signals to modulate cellular function. It is mainly composed of mesenchyme (fibroblasts and inflammatory cells), a complex assembly of collagen and elastic fiber networks, and within this cross-linked structure are the interstitial fluid and macromolecular constituents, such as glycosaminoglycans (hyaluronate) and proteoglycans, which form a hydrophilic gel [56]. The ECM in tumors

is usually more extensive than the ECM of healthy tissue [48] because fibroblasts are upregulated by the tumor microenvironment and deposit fibers that further augment the density of the ECM [10]. ECM compositions play a major role in hampering drug penetration [10, 57].

Collagen is the most abundant protein in the ECM [58]. Collagen content and structure are key determinants of macromolecular transport in tumors [59]. It can influence ECM hydraulic conductivity [59] and can physically obstruct the transport of nanocarriers by trapping them in the network, especially when the sizes of nanocarriers, for example, are larger than the space between the fibers [60]. Another ECM component, hyaluronic acid, which is in the stromal compartment of the ECM, increases the toughness of tumor microenvironment tissue, making the penetration of nanocarriers and drugs difficult [59].

The main mechanisms for the movement of small and large molecules in the ECM are diffusion and convection. However, convection is poor due to interstitial fluid pressure (see section 1.4.3), so diffusion becomes the main mechanism for transporting molecules into cells. Diffusion of large molecules in tumors has been correlated with collagen content and organization [59]. It is believed that diffusion within the tumor ECM is not efficient for delivery [51, 59]. The diffusion of nanocarriers is also considerably hindered by interactions with the ECM. As a result of these hindrances, considerable efforts have been made to modify the ECM to enhance the interstitial transport of large agents. For example, treating with the ECM enzymes such as collagenase or hyaluronidase chemically disrupted the collagen fibers or hyaluronic acid and increased interstitial transport of large agents such as antibodies and oncolytic viruses [50, 59, 61, 62]. This approach might not be useful in clinical applications due to a lack of specificity of the enzymes for tumor tissue [63]. Other strategies that have been developed for increasing local drug delivery involve external sources of energy in combination with specially designed carriers to respond to that energy for local drug release or transport [64]. Focused ultrasound (FUS) by itself or in combination with MBs, for example, is one such strategy that can be used as an alternative approach to disrupt the ECM for increased extravasation and interstitial penetration into tumors [65]. For instance, thermal absorption and mechanical agitation (both due to US) have been reported to influence the ECM, particularly collagen integrity [65, 66], which can influence ECM hydraulic conductivity for enhancing penetration. However, this thesis focuses on the potential of US or MBs for altering the ECM due to nonthermal (mechanical) forces for interstitial penetration, thereby enhancing the delivery of therapeutic agents.

1.4.3 Interstitial fluid pressure

The combination of hyperpermeable vessels, lack of functional lymphatic vessels, interstitial fibrosis and contraction of the interstitial matrix mediated by stromal fibroblasts results in an increase in interstitial fluid pressure in tumors, which reduces the effectiveness of drug transport. Interstitial fluid pressure restricts the extravasation and penetration of large molecules across the blood vessels due to the establishment of outward fluid motion from the core of the solid tumor to the periphery and the reduction in

fluid infiltration across the vascular wall [8, 10, 51]. For more detail, refer to the review by Baronzio [10]. Several methods have been proposed to decrease the interstitial fluid pressure, including normalizing blood vessels [49, 67], decreasing the content of collagen fiber and hyaluronic acid in the ECM [61, 62], recovering the lymphatic function, and using US combined with MBs [68].

1.4.4 Cell membrane

The cell membrane is another natural biological barrier that makes the transport of drugs into the cell insufficient [69]. When drugs penetrate deep into the ECM, they need to enter the cell. However, the cell is separated from the outside environment by a cell membrane that controls the movement of particles in and out from the cell. The movement of a particle into cells is mainly due to diffusion and endocytosis mechanisms. The diffusion mechanism, which is concentration driven (movement of a particle from high concentration to low concentration), is preferable for small lipophilic agents but not for large molecules that are mainly taken up by endocytosis. Endocytosis is the process of transporting molecules into the cell by engulfing them with the cell membrane and is the most common mechanism for the internalization of large molecules. Different approaches have been attempted to enhance the cellular uptake of NPs, such as molecular targeting of the particle to cancer cells, thereby inducing cellular uptake through receptor-mediated endocytosis; US-mediated cellular uptake through sonoporation; or US-induced endocytosis [18]. Describing all the mechanisms involved in cell membrane transport is not the focus of this thesis.

1.5 Physical principles of US

This section provides a basic introduction of the general description of US, which forms the basis for understanding the topics presented in this thesis.

1.5.1 Physics of US

US is a mechanical wave that can transmit through different materials, such as fluids, soft tissues, and solids. It has frequencies above human hearing or above 20 kHz [70]. US waves have numerous applications both in the medical field (diagnostic and therapy) and in industrial applications. Medical US is generated by applying an alternating voltage across a piezoelectric crystal, such as lead zirconate titanate. Such a crystal oscillates in thickness at the same frequency as the driving current, and this type of device is known as a transducer. A transducer changes electrical signals to mechanical vibrations, and vise versa. The US wave generated by an ultrasonic transducer propagates through tissue at a speed (c) depending on the tissue compressibility and density and causes the movement of molecules as the medium is compressed (at high pressure) and expanded (at low pressure), as illustrated in Figure 3, and the relationship between wavelength (λ) and frequency (f) is given by Eq. 1 [70]:

$$\lambda = \frac{c}{f} \tag{1}$$

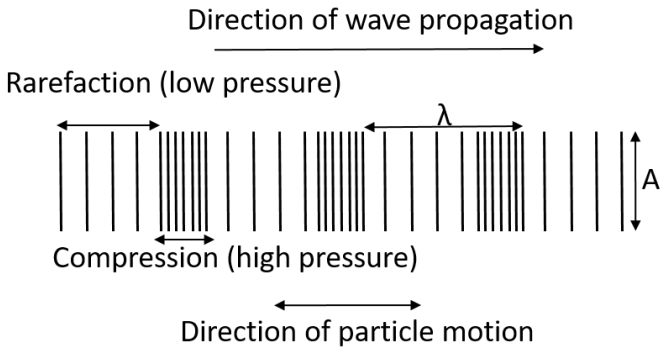

Figure 3: Schematic representation of US plane longitudinal wave propagation. The particle moves along the propagation direction of the wave. A and λ are the amplitude and wavelength of the US wave, respectively.

For medical applications, the US frequencies used are usually in the range of 0.1-40 MHz. Lower frequencies provide a greater chance of generating bioeffects and are limited in their resolution [37]. On the other hand, the attenuation of US in soft tissue increases at higher frequencies [37]. Depending on the specific medical application of US, the generation of US waves from medical US transducers can be in either pulsed or continuous mode. A pulsed US wave is generated by driving the transducer with an electrical sine wave for a short time and turning the sine wave off for a certain time before repeating the excitation. Continuous US is emitted by driving the transducer with an electrical sine wave continuously at a constant amplitude. Continuous US waves are used in Doppler and therapy applications, but primarily, medical US utilizes pulsed US. Several important parameters describe US waves, such as the amplitude of the acoustic pressure, wavelength (λ), driving center frequency (f), duration of the pulse (t), pulse repetition frequency (PRF), and duty cycle (DC). The duration of the pulse is given by $t = N/f$, where N is the number of cycles. The duty cycle is the proportion of time during which the pulse is activated and is expressed by Eq. 2:

$$DC = \frac{t}{PRP} = t * PRF \tag{2}$$

where PRP is the pulse repetition period.

Several properties of US are useful in clinical applications. Similar to the characteristics of light, US waves are transmitted in a straight line and can be focused, reflected, refracted (bent), and absorbed. Unlike light waves, US waves are physical; they are the actual movement of molecules as the medium is compressed and expanded, as illustrated in Figure 3, and thus, US can act physically on biomolecules, cells, MBs and nanocarriers. Most importantly, compared to visible light waves, US waves can be precisely transmitted through the body to a region with relatively little absorption. The noninvasive and safe delivery of mechanical forces to cells deep into the body in the form of an acoustic

pressure wave, which can result in numerous bioeffects, both thermal and nonthermal (mechanical), depending on the specific pulsing regime, is the key to US-mediated drug delivery.

1.5.2 Energy and intensity of US in a medium

US waves carry energy and are transported in the form of kinetic energy (particle motion) and potential energy (fluid compression). Hence, US waves can be described in terms of energy density and the rate at which they transmit energy. For harmonic plane waves, the average energy density (acoustic energy per unit volume) (ε) is given by Eq. 3:

$$\varepsilon = \frac{P^2}{2\rho c^2} \tag{3}$$

where P is the acoustic pressure amplitude; ρ and c are the density and speed of sound in the medium, respectively; and the average sound intensity (I), which is the rate at which power passes through a unit area perpendicular to the direction of propagation, is expressed by Eq. 4:

$$I = c\varepsilon \tag{4}$$

This means that the sound energy is transported at the speed of sound. Combining Eqs. 3 and 4, the intensity is given by Eq. 5:

$$I = \frac{P^2}{2\rho c} \tag{5}$$

For a pressure wave propagating in a medium, the acoustic intensity($\vec{I}(\vec{r};t)$) is

defined as the product of the sound pressure $p(\vec{r};t)$ and the particle velocity $u(\vec{r};t)$ in the medium through which the sound wave is traveling (Eq. 6):

$$\vec{I}(\vec{r};t) = p(\vec{r};t)u(\vec{r};t) \tag{6}$$

The average intensity over a cycle is given by Eq. 7:

$$< \vec{I}(\vec{r};t) >= Re[\frac{p(\vec{r};t)u(\vec{r};t)^*}{2}] \tag{7}$$

Where <>,* and Re indicates average, complex conjugate, and real part of the product, respectively.

With pulsed US waves, the intensity not only has spatial variation but also varies with time, and it can be reported in several different ways by considering the average and peak intensities and the pulse shape and duration. FUS is usually applied as pulses at low duty cycles to prevent extreme thermal energy deposition in the tissue.

As US waves propagate, some of their energy is lost by several mechanisms. For waves propagating through a heterogeneous medium, such as biological tissue, the waves are attenuated with distance by acoustic absorption and scattering. For a plane wave

propagating in the z-direction, the intensity I decreases exponentially as:

$$I = I_0 e^{-2\alpha z} \tag{8}$$

where I_0 is the initial intensity, $\alpha = \alpha_a + \alpha_s$ is the total attenuation coefficient, α_a is the absorption coefficient, and α_s is the scattering coefficient of the medium. However, the acoustic scattering coefficient for many tissues is relatively small compared with the absorption coefficient [71].

1.5.3 Attenuation of US wave in tissue

Biological tissue shows a strong acoustic attenuation process, and acoustic attenuation due to absorption in most biological tissue exhibits a power-law frequency dependence in the form of Eq. 9:

$$\alpha(f) = \alpha_0 f^b \qquad\qquad Np/cm/MHz^b \tag{9}$$

where α_0 is the attenuation constant, b is the frequency power-law exponent, and f is the frequency in MHz. The frequency power-dependent exponent b is typically in the range of $1 \leq b \leq 1.6$ in most biological tissues and 2 in water [71].

Some of the US energy is absorbed by the tissues and converted to heat. The loss due to absorption increases with the frequency and the density of the medium. Hence, it is a limiting factor for the depth penetration of a US wave. Moreover, it is important to note that the absorbed energy has to remain within limits that do not heat the tissue to dangerous temperatures.

The propagation of US waves is also affected by changes in the acoustic medium through which the waves are propagating. When a US wave reaches an interface, part of the energy carried by the wave will be reflected, while the remaining energy is transmitted. The amount of energy reflected by a structure that lies in the US wave path is determined by the change in acoustic impedance at its surface. For the special case of a plane wave, the acoustic impedance, Z, has the same magnitude as the characteristic impedance of the medium, $\pm\rho$c, where ρ is the tissue density and c is the speed of sound. A large difference in acoustic impedance results in a high degree of reflection, for example, at soft tissue-bone and soft tissue-air interfaces. These are seen as the brightest echoes in a US image.

1.6 US induced effects

US can result in the deposition of both mechanical and thermal energy in the medium through which it propagates. The effects of US on the medium, such as heating, cavitation and acoustic radiation force (ARF), are presented.

1.6.1 US heating

Heating is the direct effect of US absorption on the medium. As a result, US in the form of hyperthermia and HIFU therapy has become a useful technique for the treatment of

cancer and other diseases. When US propagates through tissue, energy will be absorbed by that tissue. The US energy absorbed by tissue is transformed into thermal energy, and this energy deposition can elevate the tissue temperature. If the US beam is focused, the amount of thermal energy can be higher primarily in a small region of tissues with little or no deposition at all in the surrounding tissues. The heat generated at the focus may induce bioeffects on the surrounding tissue and cells. Therefore, to develop an US technique that can be used for a specific purpose, it is also necessary to know the temperature distribution in biological tissues generated by US exposure so that the temperature effect on the tissue can be correctly controlled. The ultrasonic heat deposited in the medium as the rate per unit volume (q) is proportional to the local acoustic intensity (I) and is given by Eq. 10 [72]:

$$q = 2\alpha I \tag{10}$$

where α is the absorption coefficient (Np/m).

As a result of this heat deposition, the temperature at a point in the field will rise. The temperature distribution in the soft tissue can be estimated based on the well-known Pennes bioheat transfer equation. Since high-intensity US can potentially cause tissue alterations due to US-associated heating effects, the FDA has regulated that the intensity must cause a less than 1°C rise in temperature [73–75]. Commonly, the intensities of US used for delivery applications range between 0.3 and 3 W/cm^2. Heating has several therapeutic applications, which are presented in section 1.9.

1.6.2 Cavitation

US waves can produce direct physical effects in fluids through cavitation. At high acoustic pressures, it can also cause cavitation events in the tissue or at interfaces. Acoustic cavitation describes the interaction of a US field with a gas bubble. It is defined as the formation, oscillation, growth, and collapse of the bubble under the influence of the varying acoustic pressure field in the medium. The threshold for acoustic cavitation depends on the peak negative pressure, frequency and duration of the US wave and is also sensitive to the medium. The commonly used parameter originally developed to determine the likelihood of the occurrence of acoustic cavitation during single-cycle diagnostic US assuming all gas nuclei sized present a *priori* in a medium is the mechanical index (MI). It is determined by Eq. 11 [76]:

$$MI = \frac{P_{neg}}{\sqrt{f}} \tag{11}$$

where Pneg is the peak negative pressure (MPa) and f is the frequency (MHz). MI =1.9 is the upper limit for conventional US imaging [73].

Cavitation behavior can be generally classified into one of two categories: non-inertial cavitation or inertial cavitation (see section 1.7). A schematic representation of the response of a bubble to acoustic pressure that demonstrates the two cavitation types is

illustrated in Figure 4. Non-inertial cavitation describes when the bubbles oscillate stably around a resonant diameter at low acoustic pressure (Figure 4A). When the pressure amplitude increases, the bubble oscillatory behavior starts to become more unstable, the radius of excursion becomes more nonlinear, and the bubble fragments or forcibly collapses, which is called inertial cavitation (Figure 4B) [9]. Depending mainly on the US parameters, a cavitating bubble can generate extreme pressure and temperature, which can result in mechanical and chemical effects in addition to heating. These effects are the basis for the thermal effect-induced therapeutic applications of US.

More recently, a novel application of US combined with exogenous gas bubble (see section 1.7)-induced delivery of therapeutic agents utilizes the advantage of the remarkable ability of US to produce cavitation activity that can result in several bioeffects in tissue through a series of mechanical effects. These effects are obtained by applying typically short pulses in the range of microseconds to milliseconds with low peak negative pressures. These cavitation mechanical effects play a vital role in localized drug release and enhanced extravasation of drugs and drug carriers by permeabilizing natural barriers such as blood vessel walls, the blood-brain barrier or cell membranes en route to the target [18, 77–79]. Moreover, these effect may enable real-time monitoring of the drug delivery system [80]. The focus of this thesis is the therapeutic application of cavitation for improving drug and drug carrier delivery. The mechanism will be described more in section 1.9.

1.6.3 Acoustic radiation force (ARF)

If US is propagating through a inhomogeneous medium, the wave interacts with the medium, and the wave attenuates through three main processes: absorption, scattering, and reflection. ARF exists when a gradient of acoustic energy density is produced by the aforementioned mechanisms. The rate of change of momentum transferred from the wave to the medium due to these mechanisms gives rise to the ARF. It is a time-averaged second-order process [81] and can induce various effects on the fluids and solids around the medium. In viscous fluids, ARF induces time-averaged movement of fluids, which is known as acoustic streaming, whereas in solids and elastic media, in general, time-averaged stress induces strains, with the material deformed in not only the direction of the wave but also the traversal direction. In an object suspended in the medium, ARF induces time-averaged force, displacing (transporting) the object in the direction of wave propagation.

For an exponentially attenuating plane wave in soft tissue modeled as a viscous fluid, ARF can be expressed in terms of the time-averaged intensity ($\vec{I}$, in W/m^2) at any given spatial location by Eq. 12 [82–84]:

$$\vec{F} = \frac{2\alpha\vec{I}}{c} \tag{12}$$

where α represents the absorption coefficient (Np/m) and c is the speed of sound in the medium (m/s).

The ARF per unit volume from a quasi-plane wave on a medium can be calculated by Eq. 13:

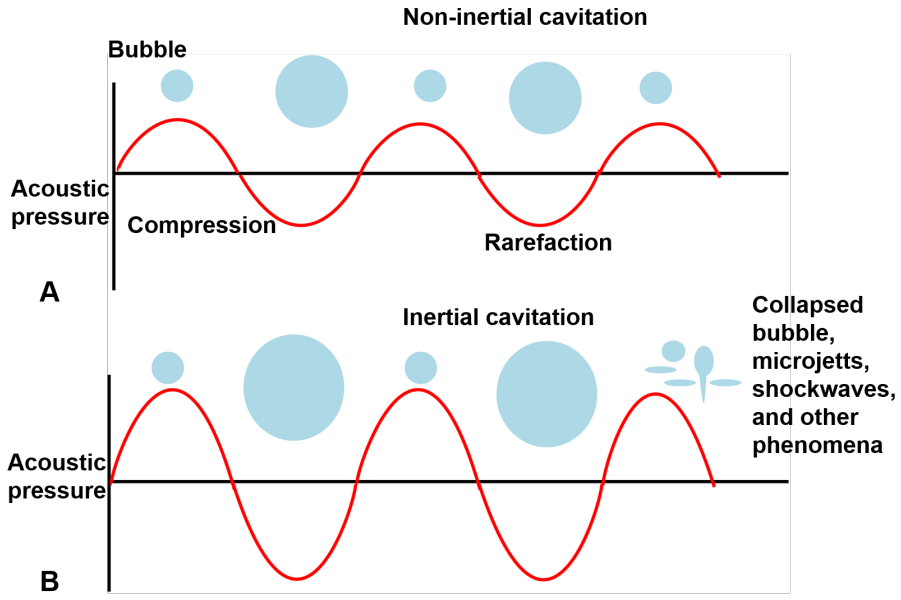

Figure 4: Response of a bubble to a US field (varying the acoustic pressure while keeping the other parameters such as frequency and bubble type constant). A) Volumetric oscillation of bubbles due to changes in US pressure. B) Under a higher US pressure field, the bubble collapses violently, producing shock waves and jetting and other inertial phenomena.

$$\frac{\Delta F(r,w)}{\Delta V} = \frac{1}{2\pi T_p \rho c^2} \int \sigma_e(r,w) \mid P(r,w) \mid^2 dw \tag{13}$$

where

$$\sigma_e(r,w) = \sigma_a(r,w) + \sigma_s(r,w) \tag{14}$$

where $\sigma_e(r,w)$ in Eq. 13 and Eq. 14 is the extinction cross-section, which is the sum of absorption and scattering; w is the angular frequency; ρ is the density; c is the speed of sound; P(r,w) is the Fourier transform of the pressure at point r; and T_p is the pulse length. The absorption cross-section is shown in Eq. 9. Whereas the scattering cross-section is dependent on the size of the scattering relative to the wavelength because the frequency depends on the scattering, it is more difficult to give a simple model. Moreover, the contribution to the ARF in bulk biological tissue is mainly caused by absorption rather than scattering [71, 84]. Eq. 13 was used to simulate the ARF in this thesis. There are a large number of practical uses of ARF-related phenomena and acoustic streaming in biomedical US applications. The uses of ARF include the power

calibration of high-intensity focused US (HIFU) devices by radiation force balance [85], the induction of excitation in shear wave elasticity imaging [86], molecular imaging, the stimulation of sensory receptors, or improvements in drug and gene delivery [84, 87]. On the other hand, acoustic streaming can be used for differentiating cysts from solid lesions [88], for stirring and mixing liquids [89], for characterizing HIFU transducers [90], and for transporting particles within fluids. It is worth noting here that in some of the aforementioned techniques, the effects of the ARF and acoustic streaming are closely linked. The focus of this thesis is the medical US application of ARF and acoustic streaming for improving drug and drug carrier delivery. The therapeutic application of ARF and acoustic streaming for drug delivery will be further presented in section 1.9.

1.7 US contrast agents and their applications

1.7.1 US contrast agents

The development of US contrast agents (UCAs) can increase the capabilities of diagnostic and therapeutic platforms. UCAs are small gas-filled microspheres (typical diameter of 1-10 μm) coated with lipid, protein or polymer shells to reduce gas dissolution and lower the surface tension, permitting prolonged circulation. The most commonly used commercial US contrast agents (UCA) are MBs and are used clinically to enhance diagnostic images due to their high echogenicity in blood and their nonlinear scattering [91]. For such applications, small MBs are required to allow them to circulate within the bloodstream and to function by strongly scattering the ultrasonic waves because of the large difference in characteristic acoustic impedance between the gas in their interior and the surrounding tissue.

The first-generation UCA, Albunex with an air core coated with albumin, was the first UCA that was commercially available and approved by the Food and Drug Administration (FDA) for clinical use [92]. Since then, a variety of different types of UCAs have been developed, and great efforts have been made to improve the stability and size of UCAs. To improve these properties, second-generation UCAs have been developed by changing the air core to a gas core containing a relatively high-molecular-weight, low-solubility gas such as perfluoropropane or sulfur hexafluoride gas [93, 94] encapsulated by a biocompatible material such as lipids, proteins, and polymers. UCAs can typically stay in the circulation on the order of several minutes before their gas content dissolves into the blood and is rapidly excreted by exhalation from the lungs. The shell is cleared by the RES in the spleen and liver [95].

The UCAs that have been approved to date by the FDA for clinical diagnostics in the United States/North America and Europe include shells of either protein (Optison) or lipids (Definity and SonoVue) [95]. By contrast, Sonazoid with a lipid shell was approved for clinical diagnostics in Japan and Korea [95]. However, the development of many other types of contrast agents is currently ongoing in various sectors. Figure 5 shows an optical image of MBs and an illustration of an MB consisting of a gas coated by a shell.

The SonoVue (phospholipid shell, sulfur hexafluoride gas, diameter of 2.5 μm) UCA was used in this thesis. SonoVue has applications in Doppler and echocardiography [96]

and appears to have no significant effect on pulmonary hemodynamics, cardiac or pulmonary function, blood pressure, oxygen saturation, or electrocardiographic parameters.

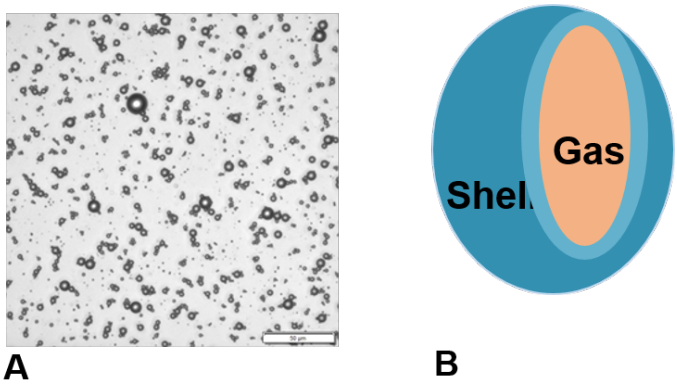

Figure 5: A) Optical microscopic image of MBs (SonoVue). Scale bar = 50 μm. B) Schematic illustration of an MB consisting of a gas coated by a shell.

MB oscillations have been investigated theoretically and experimentally by many research groups, and they occur very rapidly on the scale of microseconds [97–100]. More details about MB physics during sonication can be found elsewhere [101, 102]. The oscillatory behavior of MBs is governed by many factors, such as the US parameters (frequency, pressure amplitude, pulse length, PRF), the MB parameters (radius, type of gas core, damping coefficients, shell properties), and the environment. They undergo volumetric oscillations when exposed to US due to the compressible nature of their gas core (Figure 4). The amplitude of the oscillation depends on the acoustic pressure, the MB size, and the relationship between the driving frequency and the resonance frequency of the MB. The resonance frequency of a bubble is directly related to its size (1-10μm diameter) and coincides with the optimum imaging frequencies used in medical US imaging (1-10 MHz). The larger the size of the MB is, the lower the resonance frequency, and vice versa. Among other factors, the resonance frequency of the MB also depends on the encapsulation shell properties and the surroundings of the MB, such as vessel walls and endothelial cells [103, 104]. When MBs are located within microvessels, for instance, they experience a higher level of damping and have a shifted resonance frequency [103].

Stable oscillating bubbles can generate linear and/or nonlinear backscattered acoustic signals, which can be used to further enhance the contrast between the MB and the surrounding tissue [91]. The volumetric oscillations and the collapse of the MB can also induce various biomechanical effects that are useful for drug delivery.

UCAs are mostly MBs and have a short circulation half-life. Due to their size, even relative to human vessel pore sizes, MBs cannot extravasate into the ECM of tumors and are mainly localized in the vasculature of the tumor [105]. This is true even in vessels with

large pore sizes, such as those found in the leaky vasculature of cancer tumors, where the pore sizes range from approximately 100 to 1200 nm [2, 106]. Therefore, the application of MBs is limited to intravascular systems [105]. To extravasate MBs into the tumor ECM, the bubbles need to be in the nanoscale (i.e., 400-800 nm in diameter), which are named nanobubbles (NBs) [95, 107]. In addition to the support they give to imaging and diagnostics, NBs have received increased interest for therapeutic applications [108], and such NBs are currently under development and investigation [107, 109–112].

1.7.2 NP-stabilized MBs (NPMB)

The NPs described in section 1.2.2 were used to make the NP-stabilized MBs used in this thesis by mixing a protein such as casein and perfluoropropane gas using an Ultra-Turrax and were made at SINTEF Biotechnology and Nanomedicine (Figure 6) [42]. The resulting NPMB solution contained an excess of free NPs, and approximately 1% of the NPs were attached to MBs.

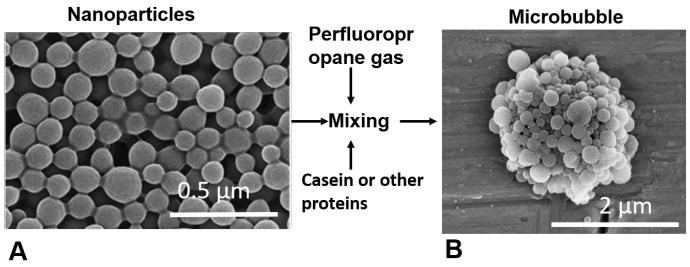

Figure 6: Optical microscopy images of A) NPs and B) NPMBs (photo: SINTEF). The NPMBs consist of the NPs as the shell and perfluoropropane as the gas core stabilized by proteins, casein in this case. Figure A) is adapted from reference [42], with permission from John Wiley and Sons.

1.7.3 Application of MBs

During the past two decades, the development of MB UCAs has enhanced the potential of US as a medical imaging modality and initiated innovative strategies for cancer detection, therapy, and post-therapy monitoring. UCAs have applications primarily in noninvasive cardiovascular imaging, such as electrocardiography and quantitative tissue perfusion and microvascular blood flow and blood volume [95, 113].

Interestingly, the potential of MBs in combination with US to produce localized bioeffects for therapeutic applications, particularly for the treatment of cancer, including breast, prostate, and liver cancer; [113–115]; drug and gene delivery [17, 95, 116, 117]; opening of the blood-brain barrier (BBB)[27, 118, 119]; and others [95, 120], has been widely tested in preclinical studies with promising results. MBs can be used with

coadministration of a drug for indirect delivery by employing non-inertial and inertial cavitation effects on enhancing the permeability of the surrounding tissues. Moreover, MBs can also serve as drug delivery vehicles that carry drugs in the blood circulation [37, 121–125], and they can be destroyed by US pulses to locally release the loaded, embedded, or entrapped agent for enhanced local delivery [37, 122–125] or in combination with an effect induced by cavitation on opening up biological barriers. This effect causes increased extravasation of drugs and drug carriers and provides the possibility for localized delivery of drugs and drug carriers. Several MB platforms, including nanoparticle-loaded [126–128] or nanoparticle-stabilized MBs [26], hard-shelled MBs [129], clusters of MBs and emulsions of liquid droplets [130], have also been demonstrated for such purposes. The first clinical case study utilizing SonoVue MBs combined with chemotherapy using gemcitabine treatments showed potential for reducing tumor sizes in patients with inoperable pancreatic cancer [29].

In addition, new applications of UCAs in molecular imaging have been realized by coupling targeting ligands to their shell, which bind to marker molecules in the area of interest [95, 116, 131], and UCAs may also be targeted to a molecular marker expressed on endothelium of specific diseases [122, 132, 133]. It is also suggested that nonlinear MB oscillations during ultrasonic compression and rarefaction phases are responsible for the generation of narrowband (harmonic and potential sub-and ultra-harmonic) emissions and broadband emissions from non-inetrial and inertial cavitating bubbles, respectively [91, 134, 135]. Hence, there is a strong interest in monitoring these emissions as a means of treatment monitoring [80].

1.8 Therapeutic US

US has been used to image the human body for more than 50 years and has become an essential and widely used diagnostic tool. US diagnostics are used, for example, to examine fetal development, and they can detect problems in the breast, liver, heart, neck, kidney, or abdomen [132]. The technology is relatively cheap and portable, especially compared with other diagnostic techniques such as magnetic resonance imaging (MRI), computed tomography (CT), and nuclear medicine imaging (PET/SPECT) [136]. The tremendous progress in engineering and computing power coupled with ultrasound transducer technology and imaging modalities over the past years has encouraged a revival of clinical interest in ultrasound therapy. Today, in addition to the well-known and widespread use of US in diagnostics, the therapeutic use of US has recently emerged and is being investigated for noninvasive therapy [137]. The therapeutic use of US that has been investigated includes thermal ablation of tissue [138, 139], breaking up of large kidney stones [139, 140], surgical tissue cutting and homeostasis (stopping of blood flow) [141, 142], treatments of tumors and cysts [143–145], drug and gene delivery to target tissue [25, 146–148], etc.

For the past few decades, US has been researched as a mechanism for the delivery of a variety of therapeutic agents to diseased cells throughout the body. US-mediated drug delivery mechanisms have enabled the delivery of small drugs, proteins, and large nanocarriers, such as gene complexes or drug-loaded liposomes, to various parts of the

body [18, 24, 26, 28, 30, 146, 147]. Recently, however, research on US-induced drug delivery using mechanical effects has increased with the introduction of MBs as US contrast agents due to their amplification of the biophysical effects of US waves that are essential for drug delivery. Preclinical studies have shown that US-MB treatment leads to an increase in the delivery of large-sized particles or molecules for the treatment of a number of diseases, such as unresectable pancreatic cancer [149], hepatocellular carcinoma [150], breast cancer [26], breast cancer metastasis in the brain [151], and Alzheimer's disease [78]. Importantly, clinical trials in pancreatic [29, 152] and liver cancer patients [30] and the first initiation of clinical BBB disruption [153] in the brain have also shown that the method has great promise. Several studies have been initiated in patients suffering from liver metastasis from primary colon cancer, pancreatic cancer, and breast cancer (NCT02233205, NCT03477019, NCT03385200). Although US and MB cavitation have been studied extensively in the US field, understanding of the underlying physical mechanism involved both in US alone and US-MB-mediated drug delivery is not yet clear. Moreover, it has been reported that MB destruction can induce bioeffects, such as microvascular leakage, petechiae, and inflammatory cell infiltration, in small animals at diagnostic US levels [154]. Understanding the mechanism and the potential side effects that arise from such treatments is therefore important to optimize US parameters and move further research into a clinical setting.

1.9 Mechanisms of US-enhanced drug delivery

Therapeutic applications of US depend on the interaction of the US field with the tissue to produce the desired beneficial bioeffect. Knowledge of the acoustic mechanisms underlying the interaction of US with tissues is needed to safely use these bioeffects for therapeutic applications. The exact mechanisms of US-induced drug/gene delivery with nanocarriers are still not fully understood. The mechanisms for inducing bioeffects are typically divided into thermal and nonthermal (mechanical) mechanisms. The thermal effects are due to heat generation, whereas the mechanical effects are mainly through ARF and cavitation mechanisms [155]. These three mechanisms can be used to enhance the delivery of therapeutic agents. Hence, they will briefly be covered as an introduction to describe how these mechanisms are involved in therapeutic US applications, especially with regard to improving the delivery of therapeutic agents.

1.9.1 Thermal effect

The thermal dose delivered by US is typically measured in cumulative equivalent minutes at 43^oC (CEM 43), which is given by the integral of $R^{(43-T)}$ with respect ot treatment time t. T is the average temperature during treatment, and R is a constant that equals 0.5 above 43^oC and 0.25 below 43^oC [156]. The two commonly used therapeutic applications of the thermal effects of US due to high intensities (10-1000 W/cm^2) are ablation and hyperthermia [137].

Ablation

Ablation therapy with real-time temperature mapping through magnetic resonance imaging (MRI) can be used to selectively destroy targeted tissue by raising the temperature of the region without affecting the surrounding tissue. Continuous exposure of tissue to high-intensity focused ultrasound (HIFU) produces heat, resulting in coagulative necrosis and soft tissue ablation [138]. If the tissue temperature is elevated above a threshold of 56^{o}C for at least 1 second, it can result in irreversible cell death [157]. Today, HIFU for thermal ablation is being used in the clinic for the treatment of uterine fibroids and prostate and breast tumors [143–145].

Hyperthermia

In addition to ablation, US can also be exploited to induce hyperthermia. Hyperthermia is the elevation of temperature between 40 and 45^{o}C. For drug delivery application, it has been shown to enhance blood flow locally and microvascular permeability, which can improve the delivery of NPs, drug carriers such as liposomes, and macromolecular drugs such as antibodies and drug-carrying polymers [146, 147, 158]. Additionally, local mild hyperthermia can be used as an external trigger for drug release from temperature-sensitive carriers, for example, thermosensitive liposomes [30]. The biological effects of US that result from heat production are not the primary focus of this thesis; however, it has to be well controlled, particularly for ARF applications that may require high intensity, to avoid unwanted side effects on the tissue.

1.9.2 Nonthermal effect

A more widely investigated approach for US-induced drug delivery is achieved using mechanical mechanisms. This approach uses ARF or US combined with gas-encapsulated bubbles to induce openings in a nearby surface, allowing increased permeability across natural barriers such as the cell membrane, the vessel wall, and the blood-brain barrier. Often, pulsed US with short duty cycles is used to minimize heat generation and allow the mechanical effect of US (ARF) to predominate, and it can be further enhanced by combining US with MBs (cavitation). The basis of the key nonthermal mechanisms that are relevant to the biological effects of US, focusing on the delivery of therapeutic agents, is presented below.

Acoustic radiation force

The use of ARF for investigation of the mechanical properties of soft tissue and for therapeutic application is becoming a widely investigated research area. It has been shown that ARF that results from the transfer of momentum from the US field to the object [81] can create mechanical forces that induce nonuniform displacement of the tissue resulting from a strain difference, as well as acoustic streaming. The degree of displacement will primarily be determined by the elasticity (Young's) modulus of the tissue [159, 160]. Pulsed HIFU-generated ARF can enhance the permeability in endothelial cells, open cell membranes [161], widen intercellular spaces [162], expand the extracellular and perivascular spaces in the brain [163], and disrupt the ECM for increased extravasation and diffusion of drugs and/or NPs through the interstitium [164]. It has also been

demonstrated that ARF can induce acoustic streaming through the ECM and has the potential to increase convective transport [165], thereby improving the biodistribution of extravascular drugs in the target tissue [28].

Moreover, ARF can also push circulating MBs or drug-loaded MBs toward the endothelial wall [166–168] and promote the delivery of liposomal doxorubicin (DOX) [169, 170], liposomes encapsulating gadopentetate dimeglumine (an MRI-detectable model representing pharmaceutical agents) [171], and naked DNA [172]. Moreover, ARF has also been shown to enhance the penetration as well as accumulation of small molecules in both *ex vivo* and *in vivo* healthy porcine kidneys [173]. Recently, it has been shown that US improved the distribution of polymeric NPs in a healthy brain [27, 28].

Cavitation

As described in section 1.6.2, cavitation is a series of complex phenomena used to describe the reaction of gas-filled bubbles during US exposure, which is considered the main impetus to advance targeted delivery [174]. The physical basis of cavitation-induced drug delivery is the mechanical forces (shear and circumference forces) induced on the surrounding tissue by bubble oscillation imposed by US exposure. The bubble oscillations also generate a flow, which is known as microstreaming, in the surrounding liquid that, through pressure and friction forces, facilitates drug release and transport and enhances drug uptake [175]. Microstreaming can have velocity and shear rates proportional to the amplitude of oscillation. Moreover, ARF that can translate the MBs can be generated. The collapse of a bubble can also cause shockwaves as well as liquid microjets when in proximity to physical boundaries such as vessel walls, the blood-brain barrier, or cell membranes [176]. It is also associated with the formation of radicals [104].

Cavitation is considered the most important and well-studied nonthermal US mechanism that enhances drug delivery by producing various effects on biological tissue. Multiple physical mechanisms, as described above, are reported to cause temporary disruption of nearby physical structures such as blood vessels or the blood-brain barrier and cell membranes to enhance local drug or drug carrier extravasation and intracellular uptake of drugs, respectively [25, 37, 176]. The cavitation-induced increase in cell membrane permeability is also called sonoporation [77, 105]. The mechanical forces acting on the cellular membrane may result in membrane opening and/or invagination resulting in endocytosis [177, 178]. Transmembrane transport is therefore believed to be associated with these two mechanisms [177, 178]. Transvascular transport can be enhanced due to cavitation-induced increases in the gap junction distance between vascular endothelial cells and/or temporary disassembly of the molecular structure of tight junctions (BBB disruption). Inertial cavitation-induced microstreaming has also been shown to be the most effective approach for transporting macromolecular therapeutics against elevated intratumoral pressure and across the dense ECM away from the vasculature [179]. Cavitating bubbles close to the endothelial wall have also been reported to induce antivascular effects in tumors such as vascular disruption, invagination, vasoconstriction, or even shutdown of the vessels [104].

Although cavitation can contribute to the effectiveness of therapy by opening biological barriers, the mechanisms of this effect are not fully understood. Many factors affect the magnitude of the permeabilization of natural barriers, including the US parameters (pressure, exposure time, US frequency, burst length, pulse repetition frequency, etc.) and MB properties (concentration, average size of the MB, composition of the MB shell, etc.). A wide range of US parameters and MB types have been evaluated in drug delivery both *in vitro* and *in vivo*. Among them, the pressure and MB concentrations are considered the most important factors to induce blood vessel wall, cell membrane, and BBB opening [180]. Increasing the pressure amplitude and the sonication time increases the magnitude of the vessel permeation; however, unwanted side effects such as hemorrhage, erythrocyte extravasation, ischemia, edema formation, cell apoptosis, and inflammation could be induced at higher pressure amplitudes and upon prolonged sonication [154, 181, 182]. Moreover, it was reported that excessive MB concentration could result in higher BBB opening levels and damage [183]. Therefore, further efforts are required to optimize the US treatment strategy and explicitly demonstrate the mechanisms underlying MB-cell interactions in order to establish suitable standard parameters for US combined with MB-induced drug delivery.

2 OBJECTIVE OF THE STUDY

The overall aim of this thesis is to contribute to the understanding of the mechanisms involved in US-mediated delivery of nanoscale particles and drugs into diseased tissue. US alone or combined with MBs has been shown to increase the delivery of NPs and drugs to cancer tissues in various ways. However, this improvement in delivery necessitates an understanding of how US alone or in the presence of MBs can be used to ensure a safe and effective strategy for NP or drug delivery in tumor tissues. Hence, the impact of cavitation and ARF on the delivery of nanocarriers across biological barriers in tumors was studied.

Six specific objectives were addressed to accomplish the overall aim of this thesis;

- To obtain new knowledge of the mechanisms involved in US combined with MB-mediated delivery of drugs and drug carriers into tumor tissue.
- To record the behavior of nanoscale particles injected with MBs during US exposure.
- To determine the effect of acoustic parameters on the vasculature and the influence of vascular parameters on permeability induced by US combined with MBs to enhance extravasation and penetration of nanoscale particles into the ECM.
- To examine the effect of US combined with MBs on manipulating the collagen for enhancement in NP and drug penetration into the ECM.
- To investigate the impact of ARF on improving the transport and microdistribution of NPs in solid tumors.
- To test the effect of ARF on the transport of NPs in collagen gel as well as deformation of the collagen gel as a model for the ECM.

3 MATERIAL AND METHODS

This section includes the various techniques and models applied in the present work. More information about how the techniques were used in the present study can be found in the original papers.

3.1 Model Systems

3.1.1 Animal model

BALB/c nude mice were used for *in vivo* experiments in **Papers I-III**. These mice lack a thymus, are unable to produce T-cells and are therefore immunodeficient. They are hence useful for the implantation of foreign cells. The animals were housed in IVC cages under conditions free of specific pathogens according to the Federation of European Laboratory Animal Science Association's recommendations. They had free access to food and sterile water. All animal experiments were approved by The Norwegian Animal Research Authorities, i.e., the Norwegian Food Safety Authority.

3.1.2 Tumor cell line

The human osteosarcoma cell line (OHS) was grown as xenografts subcutaneously in athymic mice in a dorsal skinfold window chamber (**Paper I**) and in a mammary fat pad (**Paper II**). The KPC001s cell line derived from a genetically engineered mouse model (KPC mouse) as a model of pancreatic ductal adenocarcinoma (PDAC) and KPC closely replicates the genetic mutations, clinical symptoms, and histopathology found in human pancreatic cancer [184]. KPC cell lines were grown as xenografts subcutaneously in athymic mice in a mammary fat pad (**Paper II**). In **Paper III**, human prostate adenocarcinoma cells (PC3) were grown as xenografts subcutaneously on the lateral aspect of one hind leg.

3.1.3 Dorsal window chambers in mice

In **Paper I**, intravital microscopy was used to image the vasculature and NPs. Therefore, a window chamber was created in mice, and xenografts of OHS cells were grown in the chambers.

3.1.4 Skin flap model in mice

For the experiment involving intravital microscopy of the vasculature and collagen in **Paper II**, a window with a skin flap was created after the OHS and KPC tumors reached sufficient size for experimental procedures to be conducted.

3.1.5 Collagen gel

In **Paper IV**, collagen gel was used as a model for the ECM of tumors. This model was chosen to reduce the biological complexity and minimize the number of animals. Poly-

merization of collagen is achieved by changing the ionic strength, pH and temperature [185]. Collagen gels with concentrations (2.5 mg/ml) comparable to that of the tumor ECM were used as a model for the ECM (**Paper IV**).

3.2 NPs, fluorescent tracers, and MBs

3.2.1 Polymeric NPs

A novel platform of polymeric NPs (SINTEF Material and Chemistry, Trondheim, Norway) was used for the experiments in **Paper I** and **IV**. The NPs were made from PEPCA. The fluorescent dye encapsulated in the NPs (diameter approximately 160 nm) was NR668 (modified Nile Red, custom synthesis). In **Paper III**, PEGylated silica NPs (SiFluor 560, Active Motif, USA) with a diameter of 70 nm containing chromeoTM dyes were used.

3.2.2 Florescent labeling of vasculature

In **Paper I** and **II**, fluorescent labeling of blood vessels was performed by intravenous administration of 2 MDa FITC-dextran (Sigma-Aldrich, Oslo, Norway) to perform intravital microscopy. It was also used as a tracer for extravasation and penetration of the agent to study the mechanism of cavitation in **Paper I** and **II**. In **Paper III**, to stain the functional blood vessels, FITC-lectin (fluorescein-labeled Lycopersicon esculentum (Tomato) lectin; Vector Laboratories, USA) diluted in 0.9% NaCl was intravenously injected before the mice were euthanized by cervical dislocation.

3.2.3 MBs

In-house-made self-assembled NPMBs (mean diameter of 2.4 $\pm$0.2 μm; SINTEF, Trondheim, Norway) and the commercial phospholipid shell SonoVue (mean diameter of 2.5 μm; Bracco, Milan, Italy) were used. These MBs were used to study the effect of US on the vasculature and extravasation of nanoscale particles (**Paper I**), and SonoVue was also used to investigate the effect of US on the collagen network (**Paper II**).

3.3 US equipment

Three focused transducers were used in the thesis, and their specifications are shown in Table 1. The 10 MHz and 5 MHz transducers were supplied by Olympus (**Paper III-IV**), and the 1 MHz transducer was supplied by Precision Acoustics (Precision Acoustics Ltd, Dorchester, UK) (**Paper I-II**). The transducers were characterized in a water tank measurement system (Onda AIMS-III, Sunnyvale, CA, USA). The pressure and -3 dB beam width of the US beam at the region of interest were measured with a calibrated HGL-0200 hydrophone (Onda Corporation, Sunnyvale, CA, USA) and 20 dB AH-2010 preamplifier (Onda Corporation, Sunnyvale, CA, USA).

Table 1: Transducer parameters

Center frequency (MHz)	1	5	10
Aperture (mm)	60	29	19
Geometric focus (mm)	75	60	50
-3 dB beam width at focus (mm)	2.4	0.61	0.34

3.4 US exposure set up

A similar intravital microscopy setup set up was used in real time during US exposure in **Paper I** and **II** and is shown in the original papers. In **Paper III** and **IV**, the exposure setup is shown in the original papers. Generally, the setups have a signal generator (Hewlett Packard 33120A, San Jose, CA, USA), a power amplifier (ENI 2100L, Rochester, NY, USA), an oscilloscope (Lecroy WaveRunner, LT262, Long Branch, NJ, USA), a transducer, an insonication chamber, and, in most of the setups (**Paper I-III**), a calibrated fiber-optic hydrophone system (Precision Acoustics Ltd, Dorchester, UK). For more detail, see the original papers.

3.5 Confocal laser scanning microscopy

A sample is excited by a beam of laser light on a small focal plane, fluorescence is emitted at a point during the scanning process and detected by a photomultiplier tube, and the signal is reconstructed into an image by a computer. To minimize the unwanted signal from outside the focal plane, a pinhole is inserted between the detector and the sample. This technique was used in **Paper III** and **IV**.

3.6 Multiphoton scanning microscopy

Multiphoton scanning microscopy involves nonlinear excitation of molecules in a sample. This means that multiple photons are used in light-matter interactions. The primary signal source in multiphoton scanning microscopy is two-photon excited fluorescence. This technique was used in **Paper I** and **II**.

3.7 Second-harmonic generation (SHG) microscopy

SHG microscopy has emerged as a powerful technique for studying the important features of the collagen structure and content in tumors with subcellular resolution [186]. SHG imaging is a nonlinear optical imaging technique. SHG is a process that occurs when two photons of incident light interact with a triple-helix structure that is not centrosymmetric, such as collagen fibers [187], creating an SHG photon with a frequency exactly twice the excitation frequency, ω (or half the wavelength). SHG and two-photon excitation

fluorescence use a similar principle. However, the former is based on nonlinear scattering, whereas the latter is based on nonlinear absorption resulting in fluorescence emission.

SHG is a good alternative to conventional or fluorescence-based histology for studying and visualizing the molecular structure of collagen because it is an intrinsic signal, does not require the addition of any label or stain and has high sensitivity and specificity [188, 189]. The optical sectioning capability of SHG also permits 3-dimensional (3D) resolution *in vivo* [187]. The SHG imaging technique was used in **Paper II**.

3.8 Preparation of tissue sections

Solid tumors (**Paper I**) were harvested, preserved in formaldehyde and embedded in paraffin after the experimental animals were terminated. Five μm sections were prepared and stained with hematoxylin, eosin, and saffron (HES) for histology. In **Paper III**, 25 μm frozen sections from treated and unexposed tumors were stained for histological (HES) analysis.

3.9 Image analysis

Data acquisition in the present work is based on built-in software on the imaging systems **Paper I-IV**). Data processing and analysis were performed using custom-written MATLAB software (The Math Works, Natick, MA, USA) and ImageJ (NIH, Bethesda, MD, USA).

4 SUMMARY OF RESULTS

This section presents an overview of the most important results obtained. More detailed information is provided in the original papers.

PAPER I:-*Effect of ultrasound on the vasculature and extravasation of nanoscale particles imaged in real time*

In this paper, the focus was obtaining new knowledge on the behavior of nanoscale particles injected together with MBs during US exposure, studying the influence of vascular parameters on extravasation and elucidating the effect of acoustic pressure on the vasculature for extravasation and penetration of nanoscale particles into the ECM in real time. Intravital multiphoton microscopy was performed during sonication of tumors growing in dorsal window chambers, and FITC-dextran (2 MDa) was injected to visualize blood vessels. Tumors were sonicated at mechanical indexes (MIs) from 0.2 to 0.8 after injection of NPMBs or SonoVue plus NPs. The effect of the acoustic pressure and MB type on the vasculature was studied. In addition, the impact of vessel diameter, vessel structure, and blood flow was characterized. We found that the rate and extent of penetration of NPs and dextran into the ECM increased with increasing MI and that dextran penetrated deeper than NPs. Furthermore, we found that to achieve extravasation, smaller vessels required higher MIs than did blood vessels with larger diameters. Interestingly, the majority of extravasation occurred at vessel branching points. Moreover, we found that US changed the blood flow rate and direction for all MIs tested.

PAPER II:-*Effect of ultrasound and microbubbles on the collagen network in solid tumors*

The motivation for this work was to determine whether the enhanced penetration of large particles or molecules into the ECM induced by US combined with MBs was due to a change in the ECM. Hence, we investigated the effect of US combined with MBs on the collagen network of the ECM. Two tumor types that differed in vascular density and stromal contents were grown as xenografts in a mammary fat pad and sonicated with US at MIs of 0.4 or 0.8 after injection of a commercial contrast agent. The amount, anisotropy and organization of the collagen fibers before and after US sonication were quantitatively analyzed from SHG images. No changes in collagen content and structure for either of the tumor models were found independent of the MI applied. The result indicates that the increase in the penetration of NPs due to US combined with MBs (at the same MIs we tested) found in the previous studies is not due to a change in collagen in the ECM.

PAPER III:-*Effect of acoustic radiation force on the distribution of nanoparticles in solid tumors*

The focus of this work was to investigate the influence of acoustic radiation force (ARF) on improving the transport and microdistribution of NPs in tumors. For this study, tumors grown in mice were exposed to high-frequency (10 MHz or 5 MHz) FUS after injection of silica NPs. The US-mediated displacement of NPs from blood vessels

was measured quantitatively from confocal microscopy images of frozen tumor sections. Using the same experimental exposure parameters, ARF was simulated and compared to the experimental data. Enhanced extravasation and interstitial transport of NPs in tumor tissues were observed. Larger displacement was found upon FUS (10 MHz, acoustic intensity 234 W/cm^2, 3.3% duty cycle) exposure than upon FUS (5 MHz, acoustic intensity 337 W/cm^2, 0.6% duty cycle) exposure. Simulation of ARF shows that the FUS (10 MHz) produced a peak ARF per unit volume of 2.0 x 10^6 N/m^3 and therefore indicates that such a force can enhance the penetration and microdistribution of NPs. Simulation of the displacement of a single NP based on the Stokes drag equation shows a significantly lower displacement than the median increase in displacement found experimentally, indicating that the direct force on the particle has a small effect on enhancing the penetration and microdistribution. The simulations also suggest that acoustic streaming was the dominant mechanism for the observed enhancement. Our results are important to obtain new knowledge of the underlying mechanisms for US-mediated delivery of NPs and the impact of ARF.

PAPER IV:-*Effect of acoustic radiation force on displacement of nanoparticles in collagen gels*

In this paper, collagen gel, as a tissue-mimicking phantom, was developed to study the effect of ARF on the penetration of NPs in collagen gels and deformation of collagen gels under different US parameters (by varying the pressure and duty cycle) both experimentally and computationally. The penetration of NPs and deformation of the collagen gel were measured quantitatively from confocal microscopy images before and after US exposure. ARF was simulated based on the experimental parameters. The numerically estimated penetration of the NPs and deformation of the gel were compared with the experimental data. We found that ARF has little effect on the penetration of the NPs into the collagen gels for the US parameters used in our model. Moreover, the experimental and theoretical results were consistent, showing that ARF had a much higher impact on gel deformation than on the displacement of NPs in the gel. The simulation also revealed that ARF was the dominant mechanism for the deformation of the collagen gel in the model.

5 GENERAL DISCUSSION AND FUTURE OUTLOOK

The ability to deliver macromolecular anticancer agents (nanocarriers, antibodies and viral vectors) across biological barriers such as vessel walls, the ECM, or cell membranes is highly important for their therapeutic efficacy against cancer. The use of US alone or in the presence of MBs has attracted attention as a method to enhance drug delivery by inducing several bioeffects on barriers to facilitate penetration of macromolecular agents across biological barriers (section 1.4). The effects of US combined with MBs on the biological barriers, focusing on the vasculature and ECM, to enhance the extravasation, penetration, and accumulation of NPs in tumors were studied in **Paper I-II**. In addition, the potential of ARF for affecting the transport and distribution of the NPs in tumors and in collagen gel as a tissue-mimicking phantom was studied in **Paper III-IV**.

Previously, several preclinical studies have demonstrated that MB combined with US treatment can enhance the delivery of drugs and NPs to solid tumors [18, 26, 77, 78], and an encouraging treatment response was found, i.e., reduced tumor growth and improved animal survival [26, 115, 126, 190, 191]. Although many efforts have been made to study the mechanisms by which US exposure in the presence of MBs enhanced the delivery of NPs to solid tumors, there remains considerable uncertainty about the specific mechanisms. To gain new insight into these mechanisms, we imaged the effect of US combined with MB on the enhancement in nanoscale particle extravasation, penetration, and accumulation into the ECM in real ime during US exposure (**Paper I**). The tumor model was selected based on vascular density. OHS tumors are well vascularized throughout the tumor and have no necrotic core [192].

Paper I revealed the importance of real-time imaging of US-induced effects on the vasculature and of the behavior of nanoscale particles or molecules during US sonication using multiphoton microscopy. To our knowledge, this work is the first reported real-time imaging study in solid tumors *in vivo*. However, multiphoton imaging of the opening of the blood-brain barrier has previously been conducted [193–195]. The results obtained from the multiphoton images (**Paper I**) therefore provided direct evidence for therapeutically relevant effects of US and MB and revealed extravasation of nanoscale particles into the extravascular space, which indicates an enhancement in blood vessel permeability. Interestingly, at lower pressures, relatively slower extravasation of the agents, mainly due to stable cavitation-induced mechanical forces, was found in the larger blood vessels than in the blood vessels with a smaller diameter, where burst-like extravasation occurred due to higher pressures. The main mechanism for this violent extravasation at higher pressures is most likely inertial cavitation-induced biophysical effects. Both the stable and inertial cavitation mechanisms create pores in the vessel wall, causing materials to extravasate from the vessel depending on the pore size created. The relationship between acoustic pressure and vessel diameter was reported for the first time in this work (**Paper I**). However, Sassaroli and Hynynen have previously reported that the resonance frequency of a bubble confined in a blood vessel depends not only on the size of the bubble but also on blood vessel parameters, such as radius and length [103]. The results from **Paper I** suggested that in addition to the US and MB parameters, the likelihood

of cavitation-induced vascular opening depends on the vessel diameter. Importantly, the majority of extravasation occurred at vessel branching points independent of the pressure applied. This phenomenon is probably due to MBs being more easily trapped at such locations [194]. The proximity to the vessel wall and the availability of space for the MBs have been shown to have great importance for the effect of cavitation on the vessel both *in vitro* [196–199] and *ex vivo* [200–202]. Hence, the distance between the vessel wall and MB as well as the space available for MBs to oscillate might also have an influence on the observed results.

Another interesting observation in **Paper I** is the change in blood flow. We assessed the change in blood flow and direction as well as the flow rate of the NPs by real-time imaging, and we found that US sonication causes a local reduction in flow rate and change in directions and that these changes correlate with the acoustic pressure. This finding is consistent with other reports that US combined with MB induced shutdown of blood flow, and reduction in perfusion has been shown in tumors, brains and other tissues [194, 203–205]. However, locally enhanced perfusion has also been reported [206]. The mechanism responsible for the change in flow during US is not yet fully understood. However, it might be due to one or a combination of the following mechanisms: inertial cavitation, aggregation and activation of platelets in the regions where destruction of MBs occurred, and vasoconstriction induced in arterioles [104, 194, 204]. This knowledge may provide valuable information for the development of a strategy aimed at optimizing the effects of cavitation. Blood flow can cause fluctuations in the amount of MBs in the target region, thereby affecting the onset of extravasation and the outcome of cavitation-induced bioeffects for drug or drug carrier delivery. On the other hand, the reduction in blood flow might be beneficial if the purpose was to induce a direct therapeutic effect by cutting or shutting down the blood supply and killing the cells by means of apoptosis or necrosis, as has been reported in previous works [191, 207].

Two treatment groups representing different strategies for US-assisted MB drug delivery were used, with the aim of comparing the in-house-made NPMBs with the commercial MBs (**Paper I**). The first strategy was incorporating the NPs on the bubble itself (NPMB), and the second is a coinjection strategy (NPs with commercial MBs). The results showed a faster penetration of the NPs into the ECM when using NPMBs than when coinjecting the NPs with the MBs. This finding is consistent with the suggestion by others that integrating NPs onto MBs was more efficient in US- and MB-induced enhancement of tumor uptake than coinjecting NPs with MBs [126].

A large variation between the individual extravasations was found. The relatively large variation in penetration and accumulation into the extracellular matrix between individual extravasations was probably caused by the size differences in the pores created in the blood vessel wall due to polydisperse MBs exerting different shear stresses on the blood vessel wall, which has been shown by other studies as well [208].

Importantly, there is no doubt that extravasation events were highly associated with the acoustic cavitation of MBs. The occurrence of extravasation was heterogeneous in time and position. The number of extravasation events may be extended by sustaining the cavitation process with appropriate pulse sequence and/or MB parameters [9]. When

polydisperse MB were administered, for instance, US pulses of increasing pressure can be delivered sequentially to activate MBs of specific sizes with each pulse. In addition, this approach can also open various blood vessel walls with different blood vessel diameters. This strategy could effectively sustain cavitation and exert various effects on the different-sized vessels at the target site.

The penetration of NP drugs through the extracellular matrix (ECM) of tumors is another limiting factor for the sufficient and uniform delivery of NPs or drugs to tumor cells. This is because of the composition and structure of the ECM in tumors [59, 209] and because of the insufficient convective and diffusive forces, which are limited by the high interstitial fluid pressure and the large size of the NPs, respectively. **Paper II- IV** investigate the effect of ARF and cavitation on improving transport through the ECM. Theoretically, enhanced microdistribution can be accomplished by enhancing the convection by altering the component and structure in the ECM, which results in a reduction in interstitial fluid pressure; by generating a local pressure gradient; by using inertial cavitation-induced microstreaming; or by introducing events that promote diffusion.

It was reported that microstreaming can facilitate the convective transport of substances across biological barriers by orders of magnitude over diffusive transport [9, 210]. The convective transport of particles could also be promoted by ARF and acoustic streaming (**Paper III**).

Modulating the ECM has been shown to increase the interstitial transport of large agents [63, 65, 66]. In **Paper I**, it was found that US combined with MBs improved delivery into the ECM. Next, we wanted to study whether the improved penetration into the ECM could be due to a change in the collagen network, either changes in the amount of collagen or structural changes (**Paper II**). Because collagen is the most abundant protein in the ECM [58] and because of its unique feature for visualization by SHG, we focused in **Paper II** on the effect of US combined with commercially available MBs on the collagen fiber network of the ECM. Intravital microscopy and an *in vivo* model were chosen for optical imaging of the collagen before and after US exposure. Analysis of the SHG images showed that there was no change in collagen content or structure in the ECM due to US combined with MB exposure in the two tumor types for the pressures applied. This finding is consistent with another recent study [68].

The main limitation of the study in **Paper II** is that few animals were used for one of the tumor types; however, the reproducibility of the results was demonstrated by using two different tumor types. However, several factors can also explain the results in **Paper II**. In **Paper II**, we aimed to induce cavitation to cause extravasation and change the collagen network, probably mainly in the proximity of the capillary wall. From **Paper I**, we found that the occurrence of extravasation was heterogeneous both in numbers and in position and that extravasation might not occur in the field of view during US exposure. Hence, the size of the area imaged might affect the results because the probability of observing a cavitation event and detecting changes in the collagen network in the imaged area might be limited. Due to skin flap surgery, blood vessels might also be disrupted. This might affect the concentration of MBs present in the region, which could result in

a reduction in cavitation activity in the region. Hence, this reduction might minimize the bioeffect on the collagen network. In addition, it should also be emphasized that the lack of observed changes in the collagen network does not rule out that changes can occur on a length scale not detectable optically. The lateral resolution of optical imaging using near infrared wavelengths is typically approximately 500 nm. Other methods, such as electron microscopy, which has a resolution of 50 pm, might also be needed for further investigation in the future [211]. However, other components of the ECM, such as glycosaminoglycans, might be influenced by US irradiation, which was not investigated in this study. This study is ongoing, so more experiments could be conducted to investigate changes in these components. The collagen network in the ECM is embedded in a hydrophilic gel of glycosaminoglycans; hence, more focus will be given to hyaluronan. Moreover, due to their very short circulation time and large size, commercial MBs are restricted from extravasation and accumulation in tumor tissue [29]; thus, their application is limited to intravascular systems [105]. Therefore, nanobubbles or nanodroplets may extravasate and accumulate beyond the vessel wall into the tumor ECM and affect the ECM upon sonication with US, so these materials would be interesting to investigate in future studies.

Intravital microscopy and *in vivo* models will be useful for the continuing development of techniques for optical observation of US and MB effects on the vasculature and ECM in real time during US exposure (**Paper I-II**). Intravital microscopy may be used for direct observations of the MB behavior in the blood vessels and the dynamics of the collagen network if a high imaging frame rate is used. The findings presented in **Paper I** may also encourage investigators to consider the importance of the vasculature when developing strategies for the applications of US and MBs. This experimental result may also provide references for developing better models to simulate the penetration of nanoscale particles into the ECM as well as the behavior of MBs in the vasculature. In the future, the experimental setup could be optimized to provide better results. One main challenge in setting up the optical system is the low imaging frame rate, which limited observation of the MB dynamics and the dynamics of the collagen fibers due to cavitation in **Paper I** and **II**, respectively. One major limitation is that due to the lack of sufficient space present in our experimental setup (**Paper I** and **II**), cavitation detection was not included. Stable and inertial cavitation produce subharmonics of driving frequency and broadband white noise, respectively. Cavitation monitoring would provide further understanding of the role and variation of cavitation in drug delivery. For cavitation-induced treatment, the implementation of real-time cavitation monitoring is important to ensure optimal sonication conditions over the treatment period.

Another mechanism that was investigated besides the cavitation (**Paper I-II**) that might have a potential to use for drug delivery application was ARF. This is the focus of **Paper III-IV**.

To have successful ARF-mediated therapeutic applications, the effect of ARF needs to be understood. A growing line of evidence suggests that ARF from pulsed HIFU has great potential to enhance the penetration of NPs, drugs, and genes into various tissues [28, 164, 169, 171–173]. ARF is the transfer of momentum from a US propagating wave

into the medium and is proportional to the attenuation of the wave in the medium, the frequency of the wave, and the intensity of the propagated wave and is inversely proportional to the speed of the wave in the medium. High-intensity US can also act on a bulk fluid, which can induce acoustic streaming that can indirectly affect the NPs and increase NP displacement in the tumor tissue [165, 212]. In **Paper III**, we investigated the effect of high-frequency (10 MHz and 5 MHz) FUS on the transport and distribution of NPs in tumors.

The results in **Paper III** show an increase in extravasation and interstitial transport of NPs in tumor tissues after insonication with US compared with those in the nontreated tumor tissue. When applying US exposure a few minutes after injection of the NPs, the concentration of NPs in the circulation is high, and the enhancement in the transport of the NPs is believed to result from the ARF having an impact on the NPs' ability to cross the blood vessel wall. On the other hand, when performing US exposure within a few hours after injection of the NPs, the entry of NPs into the extravascular compartment may be increased due to the EPR effect, and the increase in interstitial transport of the NPs, based on the distance to the nearest blood vessel, as measured from confocal microscopy images of tumor sections, is likely due to the effect of US exposure-induced ARF. Previously, our group found a similar enhancement [213]. Simulation revealed that the main mechanism responsible for the enhanced microdistribution of the NPs in the exposed tumor tissue was ARF-induced acoustic streaming (**Paper III**).

In **Paper III**, the large variation in NP transport and distribution found among the tumors was likely due to the difference in vascularization of the different tumors, which have varying perfusion and vascular density, blood vessel permeability and necrosis within the tumor tissues.

In **Paper III**, the effect of FUS on the transport of NPs across the blood vessel wall and through the ECM of the treated and untreated tumors was studied with a confocal microscope. Tumor sections were imaged to quantify NP transport and microdistribution in the tumor tissue. An inherent limitation of the method used to assess the effect is that it is not possible to know exactly which area of the tumors were treated after excision and sectioning of the tumors. Due to the small focal spot of the transducer, the exposure was performed by moving the transducer using a step motor to scan across the tumor in horizontal and vertical patterns and by keeping the transducer fixed for several minutes at each point. Nevertheless, only a small part of the tissue was exposed to US; hence, untreated tissue was added to the analysis, which could underestimate the effect estimated from the analysis. To better evaluate the effect of ARF in the future, one possibility could be imaging the treated volume of the tumor in real time using other imaging modalities such as multiphoton microscopy during sonication. Another study on ARF was performed in our group and showed a slight increase in the penetration distance of NPs in brain tissue in a few animals after exposure to a high frequency (7.8 MHz) in addition to the displacement caused by blood-brain barrier opening using a low-frequency (1.1 MHz) transducer combined with NPMBs [27]. The opening was likely due to cavitation. Such a multistage delivery platform, first increasing the permeability of the vessel wall using cavitation and then applying ARF once the NPs are in the ECM

to improve penetration further away from the vessels into the ECM, might be interesting for further advancement. For such multistage applications, the development of a dual-frequency transducer is important.

The improved distribution of NPs in tumors after US treatment in **Paper III** was further tested in collagen gel as a tissue-mimicking model (**Paper IV**). It is important to develop such a *in vitro* model to reduce the number of mice used. Similar US exposure was used in both **Paper III** and **IV**, and both papers compare the experimental results with the simulation of ARF and predicted displacement of NPs. The collagen gel concentration was chosen based on the collagen % in tissue, and the gel displays several properties resembling collagen found in the tumor ECM. When the collagen gel is exposed to US, both the NPs and the collagen gel itself will experience ARF due to the propagation of the acoustic field. The *in vitro* study revealed that deformation of collagen was observed, whereas ARF had little effect on the penetration of NPs into the gel. The experimental and numerical methods were also consistent with each other. One explanation is that although the collagen gel displays several properties resembling the ECM in **Paper IV**, the frequency-dependent attenuation coefficients of the collagen gel (concentration of 2.5 mg/ml) were smaller than those other tissues [214]. This may result in a small ARF and acoustic streaming in the gel. In addition, the penetration of the NPs also depends on the hydraulic conductivity of the collagen gel; hence, the estimated deformation could have an impact on the uncertainty of this parameter. Furthermore, we found that the gel showed plastic deformation, and simulation shows that the dominant mechanism for the deformation of the collagen gel is likely due to ARF. This plastic behavior of the collagen network has also been reported by others [215, 216].

In **Paper III** and **IV**, the thermal and cavitation effects are negligible, although they cannot completely be excluded. However, at high frequency (10 MHz) and at the pressure used, generation of cavitation is less likely. Modifications of the US and microscopy setup in **Paper IV** that can enable imaging of the collagen and fluorescent NPs to observe the effects in real time during US exposure will be a next step to study.

ARF has the potential to improve the penetration and microdistribution of macromolecular agents (**Paper III**), and theoretically, an endless number of treatment periods can be applied. However, the smaller focal depth at high frequencies makes this approach more suitable for superficial tumors. The capacity to generate maximum power from the transducer is another limiting factor for not getting enough ARF in the region of interest. Developing new efficient transducers is therefore necessary. **Paper III-IV** indicate that the enhancement in NP distribution through ARF depends on the US parameters. Parameter optimization is necessary to achieve the best clinical outcome.

The key to successful treatment of tumors depends on the more effective penetration of a sufficient amount of chemotherapeutic agent without causing significant toxicity to normal tissue. The concentration of systematically administered chemotherapeutic agents has been reported to decrease exponentially with distance from the tumor blood vessels. Therefore, effective penetration of intravenously administered chemotherapeutic agents is needed to reach viable malignant cells. In **Paper I** and **III**, the penetration and accumulation of the nanoscale agents were analyzed. The maximum penetration

distances induced by cavitation at lower pressures (**Paper I**) and by ARF (**Paper III**) are similar. The distance from the blood vessels to the onset of necrosis has been reported to be between 80 and 200 μm [217]. The penetration distance found in **Paper I** is relevant for clinical applications because the distance may make drugs available to more cancer cells to eradicate every fatal cell. In another study in our group using similar parameters as in **Paper I**, enhanced NP accumulation and distribution were found after US combined with NPMB treatment and were further confirmed by the promising therapeutic results obtained after subcutaneous tumors were treated with FUS combined with NPMB encapsulating the drug cabazitaxel [26]. However, the result from **Paper III** initiates an important question that remains to be answered: whether the number of NPs distributed to the solid tumors in this study is sufficient to achieve a therapeutic effect. Hence, this aspect should be investigated in the future by following tumor growth over time or by using other methods.

Comparing cavitation and ARF reveals that cavitation, particularly at higher pressures, resulted in deeper penetration of NPs than did ARF. Hence, it is likely that cavitation has a larger impact on the enhancement in the extravasation, penetration and distribution of NPs into the tumor.

In addition to the content and structure of the collagen network, US-mediated enhancement in NP transport depends on NP properties such as size and density [163, 218, 219]. The importance of size was demonstrated in **Paper I** using two different-sized NPs. The results in **Paper I** show that smaller-sized NPs penetrated farther into the ECM than did the larger NPs. The size of the NPs used in **Paper III** was similar to that of the smaller NPs used in **Paper I**. Moreover, PEGylation of NPs increases their circulation time and is important for diffusion in gels [220]. The PEG density used in **Paper IV** may affect the NP diffusivity in the collagen gel. In addition, it was reported that denser particles induced greater US transport than did particles with lower density [219]. Therefore, cavitation and ARF could play an important role in overcoming the barriers created by the ECM if the NPs' physical properties are well optimized.

Subcutaneous tumor xenografts were used in this thesis (**Paper I- III**). This is because they are easy to implant, monitor, access with US, and integrate with other imaging modalities, such as an optical microscope. Other tumor models such as orthotopic and spontaneous tumors in mice may be used before moving onto large animals. Such studies are also ongoing in our group. In addition, *in vitro* approaches are essential and expected to significantly minimize the costs and time of medicinal trials by offering cheap and reliable information before advancing to a limited number of *in vivo* experiments. Furthermore, mathematical and simulation models should be developed to predict or verify the clinical outcome of a parameter in order to optimize the deterministic parameters. This approach can also minimize the time, cost and animal lives lost for conducting *in vivo* studies.

Safety is a topic of importance. In line with past studies [221], a microhemorrhage in the tumor tissue at MI=0.8 was found in **Paper I**, and no tissue damage was observed from our histologic evaluation in **Paper III**. In blood-brain barrier disruption studies, inflammation reactions have also been observed in the sonicated area by others [181, 182],

but such reactions were not investigated in this thesis. Optimizing sonication parameters to achieve the desired effect with careful analysis of tissue damage, including hemorrhages and acute inflammation, is highly important. This was highlighted in work by Miller et al. [154] and was recently to be especially important for BBB opening in work done by Kovacs et al. [182] and McMahon and Hynynen et al. [181]. Another safety concern is that US increases temperature in the focal area of the beam and therefore has the potential to cause unintended thermal changes in tissues [222]; thus, the applied acoustic pressure has to be well calibrated and controlled.

6 CONCLUDING REMARKS

US alone or combined with MBs is a promising strategy to enhance the penetration and distribution of nanoscale particles across biological barriers, enhancing drug delivery to tumors and the brain. This effect is achieved through multiple US-induced mechanisms. The application of US can directly change the permeability of biological barriers. US combined with commercial MBs and clinically approved drugs has shown encouraging results in patients. By understanding the mechanisms of US-induced effects and optimizing the US parameters and the properties of MBs and nanocarriers, drug efficacy could be improved, and unwanted side effects could be minimized.

In this thesis, using several experimental investigations, important insights were gained concerning the impact of the nonthermal effects of US (cavitation and ARF) on enhancing drug delivery. The study involved investigation the performance of the combination of US with NPs, NPMBs or a commercial US contrast agent in overcoming the barriers to the extravasation and penetration of NPs as a drug carrier model into solid tumors. We applied US alone or in combination with MBs to improve NP extravasation, penetration, and accumulation in both tumors and tissue-mimicking collagen gel. Using cavitation, extravasation, transport, and accumulation of NPs in tumors were observed. The results also demonstrate the impact of vascular properties, such as vessel diameter and branching points in the tumor, on the onset of cavitation and the influence of cavitation on blood flow. In addition, the results suggest that imaging techniques, such as multiphoton microscopy, may provide the information needed to optimize treatment for individual tumor characteristics. Moreover, neither the collagen content nor the structure or alignment of the collagen fibrils was changed significantly after sonication with the US parameters applied in the presence of MBs.

In addition, we found that ARF and acoustic streaming enhanced NP penetration and microdistribution in tumors, whereas they had little effect on the transport of NPs in the collagen gel; by contrast, ARF induced large deformation of the collagen gel.

These findings are supplementary to the previous studies on the relationship between various US parameters or MB activities and the outcome of cavitation and ARF and could deepen our understanding of the impact of cavitation and ARF on vessel walls and the ECM. Finally, this work shows that a stronger impact on the extravasation, transport, and distribution of NPs can be obtained and that the nonthermal effect of US will have beneficial effects on cancer treatment. There is overlap in the physical basis by which the ARF and acoustic steaming mechanisms occur, so it may be that a combination of these mechanisms provides the means for US to affect drug delivery. However, comparing the cavitation and ARF mechanisms reveals that it is more likely that cavitation has a stronger effect on the penetration and distribution of NPs in tumor tissues than does ARF. Continuing the advancement, improvement, and careful study of US by itself or combined with MB for enhancing drug and gene delivery is important for translating these applications into the clinic.

References

1. Bray, F. *et al.* Global cancer statistics 2018: GLOBOCAN estimates of incidence and mortality worldwide for 36 cancers in 185 countries. *CA: a cancer journal for clinicians* **68,** 394–424 (2018).
2. Peer, D. *et al.* Nanocarriers as an emerging platform for cancer therapy. *Nature nanotechnology* **2,** 751 (2007).
3. Lammers, T., Kiessling, F., Hennink, W. E. & Storm, G. Drug targeting to tumors: principles, pitfalls and (pre-) clinical progress. *Journal of controlled release* **161,** 175–187 (2012).
4. Danhier, F., Feron, O. & Préat, V. To exploit the tumor microenvironment: passive and active tumor targeting of nanocarriers for anti-cancer drug delivery. *Journal of controlled release* **148,** 135–146 (2010).
5. Raavé, R., van Kuppevelt, T. H. & Daamen, W. F. Chemotherapeutic drug delivery by tumoral extracellular matrix targeting. *Journal of Controlled Release* **274,** 1–8 (2018).
6. Blanco, E., Shen, H. & Ferrari, M. Principles of nanoparticle design for overcoming biological barriers to drug delivery. *Nature biotechnology* **33,** 941 (2015).
7. Wilhelm, S. *et al.* Analysis of nanoparticle delivery to tumours. *Nature Reviews Materials* **1,** 16014 (2016).
8. Chauhan, V. P., Stylianopoulos, T., Boucher, Y. & Jain, R. K. Delivery of molecular and nanoscale medicine to tumors: transport barriers and strategies. *Annual review of chemical and biomolecular engineering* **2,** 281–298 (2011).
9. Wang, T.-Y., E Wilson, K., Machtaler, S. & K Willmann, J. Ultrasound and microbubble guided drug delivery: mechanistic understanding and clinical implications. *Current pharmaceutical biotechnology* **14,** 743–752 (2013).
10. Baronzio, G., Parmar, G. & Baronzio, M. Overview of methods for overcoming hindrance to drug delivery to tumors, with special attention to tumor interstitial fluid. *Frontiers in oncology* **5,** 165 (2015).
11. Anchordoquy, T. J. *et al. Mechanisms and barriers in cancer nanomedicine: addressing challenges, looking for solutions* 2017.
12. Chowdhury, S. M., Lee, T. & Willmann, J. K. Ultrasound-guided drug delivery in cancer. *Ultrasonography* **36,** 171 (2017).
13. Prabhakar, U. *et al. Challenges and key considerations of the enhanced permeability and retention effect for nanomedicine drug delivery in oncology* 2013.
14. Bertrand, N., Wu, J., Xu, X., Kamaly, N. & Farokhzad, O. C. Cancer nanotechnology: the impact of passive and active targeting in the era of modern cancer biology. *Advanced drug delivery reviews* **66,** 2–25 (2014).
15. Mura, S., Nicolas, J. & Couvreur, P. Stimuli-responsive nanocarriers for drug delivery. *Nature materials* **12,** 991 (2013).

16. Ojha, T. *et al.* Pharmacological and physical vessel modulation strategies to improve EPR-mediated drug targeting to tumors. *Advanced drug delivery reviews* **119,** 44–60 (2017).

17. Hernot, S. & Klibanov, A. L. Microbubbles in ultrasound-triggered drug and gene delivery. *Advanced drug delivery reviews* **60,** 1153–1166 (2008).

18. Afadzi, M. *et al.* Mechanisms of the ultrasound-mediated intracellular delivery of liposomes and dextrans. *IEEE transactions on ultrasonics, ferroelectrics, and frequency control* **60,** 21–33 (2012).

19. Bazan-Peregrino, M. *et al.* Cavitation-enhanced delivery of a replicating oncolytic adenovirus to tumors using focused ultrasound. *Journal of Controlled Release* **169,** 40–47 (2013).

20. Dasgupta, A. *et al.* Ultrasound-mediated drug delivery to the brain: principles, progress and prospects. *Drug Discovery Today: Technologies* **20,** 41–48 (2016).

21. Chen, Y. *et al.* Near-infrared light triggered drug delivery system for higher efficacy of combined chemo-photothermal treatment. *Acta biomaterialia* **51,** 374–392 (2017).

22. McBain, S. C., Yiu, H. H. & Dobson, J. Magnetic nanoparticles for gene and drug delivery. *International journal of nanomedicine* **3,** 169 (2008).

23. Tachibana, K. & Tachibana, S. The use of ultrasound for drug delivery. *Echocardiography* **18,** 323–328 (2001).

24. Frenkel, V. Ultrasound mediated delivery of drugs and genes to solid tumors. *Advanced drug delivery reviews* **60,** 1193–1208 (2008).

25. Carlisle, R. *et al.* Enhanced tumor uptake and penetration of virotherapy using polymer stealthing and focused ultrasound. *Journal of the National Cancer Institute* **105,** 1701–1710 (2013).

26. Snipstad, S. *et al.* Ultrasound Improves the Delivery and Therapeutic Effect of Nanoparticle-Stabilized Microbubbles in Breast Cancer Xenografts. *Ultrasound in Medicine and Biology* **43,** 2651–2669 (2017).

27. Baghirov, H. *et al.* Ultrasound-mediated delivery and distribution of polymeric nanoparticles in the normal brain parenchyma of a metastatic brain tumour model. *PloS one* **13,** e0191102 (2018).

28. Hersh, D. S. *et al.* MR-guided transcranial focused ultrasound safely enhances interstitial dispersion of large polymeric nanoparticles in the living brain. *PloS one* **13,** e0192240 (2018).

29. Dimcevski, G. *et al.* A human clinical trial using ultrasound and microbubbles to enhance gemcitabine treatment of inoperable pancreatic cancer. *Journal of Controlled Release* **243,** 172–181 (2016).

30. Lyon, P. C. *et al.* Safety and feasibility of ultrasound-triggered targeted drug delivery of doxorubicin from thermosensitive liposomes in liver tumours (TARDOX): a single-centre, open-label, phase 1 trial. *The Lancet Oncology* **19,** 1027–1039 (2018).

31. Etheridge, M. L. *et al.* The big picture on nanomedicine: the state of investigational and approved nanomedicine products. *Nanomedicine: nanotechnology, biology and medicine* **9,** 1–14 (2013).
32. Farokhzad, O. C. & Langer, R. Impact of nanotechnology on drug delivery. *ACS nano* **3,** 16–20 (2009).
33. Brigger, I., Dubernet, C. & Couvreur, P. Nanoparticles in cancer therapy and diagnosis. *Advanced drug delivery reviews* **64,** 24–36 (2012).
34. Ferrari, M. Cancer nanotechnology: opportunities and challenges. *Nature reviews cancer* **5,** 161 (2005).
35. MacEwan, S. R., Callahan, D. J. & Chilkoti, A. Stimulus-responsive macromolecules and nanoparticles for cancer drug delivery. *Nanomedicine* **5,** 793–806 (2010).
36. Kamaly, N., Xiao, Z., Valencia, P. M., Radovic-Moreno, A. F. & Farokhzad, O. C. Targeted polymeric therapeutic nanoparticles: design, development and clinical translation. *Chemical Society Reviews* **41,** 2971–3010 (2012).
37. Boissenot, T., Bordat, A., Fattal, E. & Tsapis, N. Ultrasound-triggered drug delivery for cancer treatment using drug delivery systems: from theoretical considerations to practical applications. *Journal of Controlled Release* **241,** 144–163 (2016).
38. Anselmo, A. C. & Mitragotri, S. Nanoparticles in the clinic. *Bioengineering & translational medicine* **1,** 10–29 (2016).
39. Kumari, A., Yadav, S. K. & Yadav, S. C. Biodegradable polymeric nanoparticles based drug delivery systems. *Colloids and surfaces B: Biointerfaces* **75,** 1–18 (2010).
40. Vauthier, C. in *Polymer Nanoparticles for Nanomedicines* 327–341 (Springer, 2016).
41. Ventola, C. L. Progress in nanomedicine: approved and investigational nanodrugs. *Pharmacy and Therapeutics* **42,** 742 (2017).
42. Mørch, Ý. *et al.* Nanoparticle-stabilized microbubbles for multimodal imaging and drug delivery. *Contrast Media & Molecular Imaging* **10,** 356–366 (2015).
43. Hobbs, S. K. *et al.* Regulation of transport pathways in tumor vessels: role of tumor type and microenvironment. *Proceedings of the National Academy of Sciences* **95,** 4607–4612 (1998).
44. Danhier, F. To exploit the tumor microenvironment: since the EPR effect fails in the clinic, what is the future of nanomedicine? *Journal of Controlled Release* **244,** 108–121 (2016).
45. Nichols, J. W. & Bae, Y. H. EPR: Evidence and fallacy. *Journal of Controlled Release* **190,** 451–464 (2014).
46. Miller, M. A. & Weissleder, R. Imaging the pharmacology of nanomaterials by intravital microscopy: toward understanding their biological behavior. *Advanced drug delivery reviews* **113,** 61–86 (2017).

47. Li, F., Lu, J., Kong, X., Hyeon, T. & Ling, D. Dynamic nanoparticle assemblies for biomedical applications. *Advanced Materials* **29,** 1605897 (2017).

48. Jain, R. K. Barriers to drug delivery in solid tumors. *Scientific American* **271,** 58–65 (1994).

49. Jain, R. K. Normalization of tumor vasculature: an emerging concept in antiangiogenic therapy. *Science* **307,** 58–62 (2005).

50. McKee, T. D. *et al.* Degradation of fibrillar collagen in a human melanoma xenograft improves the efficacy of an oncolytic herpes simplex virus vector. *Cancer research* **66,** 2509–2513 (2006).

51. Boucher, Y., Baxter, L. T. & Jain, R. K. Interstitial pressure gradients in tissue-isolated and subcutaneous tumors: implications for therapy. *Cancer research* **50,** 4478–4484 (1990).

52. Seymour, L. Passive tumor targeting of soluble macromolecules and drug conjugates. *Critical reviews in therapeutic drug carrier systems* **9,** 135–187 (1992).

53. Jain, R. K. & Stylianopoulos, T. Delivering nanomedicine to solid tumors. *Nature reviews Clinical oncology* **7,** 653 (2010).

54. Fukumura, D. & Jain, R. K. Tumor microenvironment abnormalities: causes, consequences, and strategies to normalize. *Journal of cellular biochemistry* **101,** 937–949 (2007).

55. Vakoc, B. J. *et al.* Three-dimensional microscopy of the tumor microenvironment in vivo using optical frequency domain imaging. *Nature medicine* **15,** 1219 (2009).

56. Jain, R. K. Transport of molecules in the tumor interstitium: a review. *Cancer research* **47,** 3039–3051 (1987).

57. Rejniak, K. A. *et al.* The role of tumor tissue architecture in treatment penetration and efficacy: an integrative study. *Frontiers in oncology* **3,** 111 (2013).

58. Canty, E. G. & Kadler, K. E. Procollagen trafficking, processing and fibrillogenesis. *Journal of cell science* **118,** 1341–1353 (2005).

59. Netti, P. A., Berk, D. A., Swartz, M. A., Grodzinsky, A. J. & Jain, R. K. Role of extracellular matrix assembly in interstitial transport in solid tumors. *Cancer research* **60,** 2497–2503 (2000).

60. Wang, Y. & Yuan, F. Delivery of viral vectors to tumor cells: extracellular transport, systemic distribution, and strategies for improvement. *Annals of biomedical engineering* **34,** 114–127 (2006).

61. Brekken, C., Bruland, Ø. S., *et al.* Interstitial fluid pressure in human osteosarcoma xenografts: significance of implantation site and the response to intratumoral injection of hyaluronidase. *Anticancer research* **20,** 3503–3512 (2000).

62. Eikenes, L., Bruland, Ø. S., Brekken, C. & de Lange Davies, C. Collagenase increases the transcapillary pressure gradient and improves the uptake and distribution of monoclonal antibodies in human osteosarcoma xenografts. *Cancer research* **64,** 4768–4773 (2004).

63. Diener, B., Carrick, L. & Berk, R. S. In vivo studies with collagenase from Pseudomonas aeruginosa. *Infection and immunity* **7,** 212–217 (1973).

64. Shukla, G. S. & Krag, D. N. Selective delivery of therapeutic agents for the diagnosis and treatment of cancer. *Expert opinion on biological therapy* **6,** 39–54 (2006).

65. Lee, S. *et al.* Extracellular matrix remodeling in vivo for enhancing tumor-targeting efficiency of nanoparticle drug carriers using the pulsed high intensity focused ultrasound. *Journal of Controlled Release* **263,** 68–78 (2017).

66. Goss, S. & Dunn, F. Ultrasonic propagation properties of collagen. *Physics in Medicine & Biology* **25,** 827 (1980).

67. Perentes, J. Y. *et al.* Low-dose vascular photodynamic therapy decreases tumor interstitial fluid pressure, which promotes liposomal doxorubicin distribution in a murine sarcoma metastasis model. *Translational oncology* **7,** 393–399 (2014).

68. Zhang, Q. *et al.* Effect of Ultrasound Combined With Microbubble Therapy on Interstitial Fluid Pressure and VX2 Tumor Structure in Rabbit. *Frontiers in pharmacology* **10** (2019).

69. Minchinton, A. I. & Tannock, I. F. Drug penetration in solid tumours. *Nature Reviews Cancer* **6,** 583 (2006).

70. Leighton, T. G. What is ultrasound? *Progress in biophysics and molecular biology* **93,** 3–83 (2007).

71. Szabo, T. L. *Diagnostic ultrasound imaging: inside out* (Academic Press, 2004).

72. Solovchuk, M. A., Sheu, T. W., Thiriet, M. & Lin, W.-L. On a computational study for investigating acoustic streaming and heating during focused ultrasound ablation of liver tumor. *Applied Thermal Engineering* **56,** 62–76 (2013).

73. Dalecki, D. Mechanical bioeffects of ultrasound. *Annu. Rev. Biomed. Eng.* **6,** 229–248 (2004).

74. Blackmore, J., Shrivastava, S., Sallet, J., Butler, C. R. & Cleveland, R. O. Ultrasound Neuromodulation: A Review of Results, Mechanisms and Safety. *Ultrasound in medicine & biology* (2019).

75. Barnett, S. B. *et al.* International recommendations and guidelines for the safe use of diagnostic ultrasound in medicine. *Ultrasound in medicine & biology* **26,** 355–366 (2000).

76. Holland, C. K. & Apfel, R. E. Thresholds for transient cavitation produced by pulsed ultrasound in a controlled nuclei environment. *The Journal of the Acoustical Society of America* **88,** 2059–2069 (1990).

77. Lentacker, I., De Cock, I., Deckers, R., De Smedt, S. & Moonen, C. Understanding ultrasound induced sonoporation: definitions and underlying mechanisms. *Advanced drug delivery reviews* **72,** 49–64 (2014).

78. Lipsman, N. *et al.* Blood–brain barrier opening in Alzheimer's disease using MR-guided focused ultrasound. *Nature communications* **9,** 2336 (2018).

79. Snipstad, S. *et al.* Sonopermeation to improve drug delivery to tumors: from fundamental understanding to clinical translation. *Expert opinion on drug delivery* **15,** 1249–1261 (2018).

80. O'Reilly, M. A. & Hynynen, K. Blood-brain barrier: Real-time feedback-controlled focused ultrasound disruption by using an acoustic emissions–based controller. *Radiology* **263,** 96–106 (2012).

81. Rooney, J. A. & Nyborg, W. L. Acoustic radiation pressure in a traveling plane wave. *American Journal of Physics* **40,** 1825–1830 (1972).

82. Torr, G. The acoustic radiation force. *American Journal of Physics* **52,** 402–408 (1984).

83. Palmeri, M. L., McAleavey, S. A., Trahey, G. E. & Nightingale, K. R. Ultrasonic tracking of acoustic radiation force-induced displacements in homogeneous media. *IEEE transactions on ultrasonics, ferroelectrics, and frequency control* **53,** 1300–1313 (2006).

84. Doherty, J. R., Trahey, G. E., Nightingale, K. R. & Palmeri, M. L. Acoustic radiation force elasticity imaging in diagnostic ultrasound. *IEEE transactions on ultrasonics, ferroelectrics, and frequency control* **60,** 685–701 (2013).

85. Wood, R. W. & Loomis, A. L. XXXVIII. The physical and biological effects of high-frequency sound-waves of great intensity. *The London, Edinburgh, and Dublin philosophical magazine and journal of science* **4,** 417–436 (1927).

86. Sarvazyan, A. P., Rudenko, O. V., Swanson, S. D., Fowlkes, J. B. & Emelianov, S. Y. Shear wave elasticity imaging: a new ultrasonic technology of medical diagnostics. *Ultrasound in medicine & biology* **24,** 1419–1435 (1998).

87. Sarvazyan, A. P., Rudenko, O. V. & Nyborg, W. L. Biomedical applications of radiation force of ultrasound: historical roots and physical basis. *Ultrasound in medicine & biology* **36,** 1379–1394 (2010).

88. Nightingale, K. R., Kornguth, P. J., Walker, W. F., McDermott, B. A. & Trahey, G. E. A novel ultrasonic technique for differentiating cysts from solid lesions: preliminary results in the breast. *Ultrasound in medicine & biology* **21,** 745–751 (1995).

89. Sarvazyan, A. & Ostrovsky, L. Stirring and mixing of liquids using acoustic radiation force. *The Journal of the Acoustical Society of America* **125,** 3548–3554 (2009).

90. Hariharan, P. *et al.* Characterization of high intensity focused ultrasound transducers using acoustic streaming. *The Journal of the Acoustical Society of America* **123,** 1706–1719 (2008).

91. Faez, T. *et al.* 20 years of ultrasound contrast agent modeling. *IEEE transactions on ultrasonics, ferroelectrics, and frequency control* **60,** 7–20 (2013).

92. Feinstein, S. B. *et al.* Safety and efficacy of a new transpulmonary ultrasound contrast agent: initial multicenter clinical results. *Journal of the American College of Cardiology* **16,** 316–324 (1990).

93. Miller, A. P. & Nanda, N. C. Contrast echocardiography: new agents. *Ultrasound in medicine & biology* **30,** 425–434 (2004).

94. Sirsi, S. & Borden, M. Microbubble compositions, properties and biomedical applications. *Bubble Science, Engineering & Technology* **1,** 3–17 (2009).

95. Paefgen, V., Doleschel, D. & Kiessling, F. Evolution of contrast agents for ultrasound imaging and ultrasound-mediated drug delivery. *Frontiers in pharmacology* **6,** 197 (2015).

96. Galema, T. *et al.* Clinical usefulness of SonoVue contrast echocardiography: the Thoraxcentre experience. *Netherlands Heart Journal* **15,** 55–60 (2007).

97. Postema, M., van Wamel, A., ten Cate, F. J. & de Jong, N. High-speed photography during ultrasound illustrates potential therapeutic applications of microbubbles. *Medical physics* **32,** 3707–3711 (2005).

98. Church, C. C. A theoretical study of cavitation generated by an extracorporeal shock wave lithotripter. *The Journal of the Acoustical Society of America* **86,** 215–227 (1989).

99. Morgan, K. E. *et al.* Experimental and theoretical evaluation of microbubble behavior: Effect of transmitted phase and bubble size. *IEEE transactions on ultrasonics, ferroelectrics, and frequency control* **47,** 1494–1509 (2000).

100. Bouakaz, A., Versluis, M. & de Jong, N. High-speed optical observations of contrast agent destruction. *Ultrasound in medicine & biology* **31,** 391–399 (2005).

101. Ferrara, K., Pollard, R. & Borden, M. Ultrasound microbubble contrast agents: fundamentals and application to gene and drug delivery. *Annual review of biomedical engineering* **9** (2007).

102. De Jong, N., Emmer, M., Van Wamel, A. & Versluis, M. Ultrasonic characterization of ultrasound contrast agents. *Medical & biological engineering & computing* **47,** 861–873 (2009).

103. Sassaroli, E. & Hynynen, K. Resonance frequency of microbubbles in small blood vessels: a numerical study. *Physics in Medicine & Biology* **50,** 5293 (2005).

104. Goertz, D. E. An overview of the influence of therapeutic ultrasound exposures on the vasculature: high intensity ultrasound and microbubble-mediated bioeffects. *International Journal of Hyperthermia* **31,** 134–144 (2015).

105. Sirsi, S. R. & Borden, M. A. State-of-the-art materials for ultrasound-triggered drug delivery. *Advanced drug delivery reviews* **72,** 3–14 (2014).

106. Dellian, M., Yuan, F., Trubetskoy, V., Torchilin, V. & Jain, R. Vascular permeability in a human tumour xenograft: molecular charge dependence. *British journal of cancer* **82,** 1513 (2000).

107. Wu, H. *et al.* Acoustic characterization and pharmacokinetic analyses of new nanobubble ultrasound contrast agents. *Ultrasound in medicine & biology* **39,** 2137–2146 (2013).

108. Mannaris, C. *et al.* Gas-Stabilizing Gold Nanocones for Acoustically Mediated Drug Delivery. *Advanced healthcare materials* **7,** 1800184 (2018).

109. Gao, Y. *et al.* Ultrasound molecular imaging of ovarian cancer with CA-125 targeted nanobubble contrast agents. *Nanomedicine: Nanotechnology, Biology and Medicine* **13,** 2159–2168 (2017).

110. Perera, R. H. *et al.* Improving performance of nanoscale ultrasound contrast agents using N, N-diethylacrylamide stabilization. *Nanomedicine: Nanotechnology, Biology and Medicine* **13,** 59–67 (2017).

111. Zullino, S., Argenziano, M., Stura, I., Guiot, C. & Cavalli, R. From micro-to nano-multifunctional theranostic platform: effective ultrasound imaging is not just a matter of scale. *Molecular imaging* **17,** 1536012118778216 (2018).

112. Mannaris, C. *et al.* Microbubbles, Nanodroplets and Gas-Stabilizing Solid Particles for Ultrasound-Mediated Extravasation of Unencapsulated Drugs: An Exposure Parameter Optimization Study. *Ultrasound in medicine & biology* **45,** 954–967 (2019).

113. Feinstein, S. B. The powerful microbubble: from bench to bedside, from intravascular indicator to therapeutic delivery system, and beyond. *American Journal of physiology-heart and circulatory physiology* **287,** H450–H457 (2004).

114. Ibsen, S., Schutt, C. E. & Esener, S. Microbubble-mediated ultrasound therapy: a review of its potential in cancer treatment. *Drug design, development and therapy* **7,** 375 (2013).

115. Lee, H. J., Yoon, Y. I. & Bae, Y. J. Theragnostic ultrasound using microbubbles in the treatment of prostate cancer. *Ultrasonography* **35,** 309 (2016).

116. Unger, E. C. *et al.* Therapeutic applications of microbubbles. *European journal of Radiology* **42,** 160–168 (2002).

117. Unger, E. C. *et al.* Therapeutic applications of lipid-coated microbubbles. *Advanced drug delivery reviews* **56,** 1291–1314 (2004).

118. Hynynen, K., McDannold, N., Vykhodtseva, N. & Jolesz, F. A. Noninvasive MR imaging–guided focal opening of the blood-brain barrier in rabbits. *Radiology* **220,** 640–646 (2001).

119. Konofagou, E. E. Optimization of the ultrasound-induced blood-brain barrier opening. *Theranostics* **2,** 1223 (2012).

120. Ghoshal, G. & Oelze, M. L. Enhancing cell kill in vitro from hyperthermia through pre-sensitizing with ultrasound-stimulated microbubbles. *The Journal of the Acoustical Society of America* **138,** EL493–EL497 (2015).

121. Escoffre, J.-M. *et al.* Doxorubicin liposome-loaded microbubbles for contrast imaging and ultrasound-triggered drug delivery. *IEEE transactions on ultrasonics, ferroelectrics, and frequency control* **60,** 78–87 (2012).

122. Lammertink, B. H. *et al.* Sonochemotherapy: from bench to bedside. *Frontiers in pharmacology* **6,** 138 (2015).

123. Suzuki, R. & Klibanov, A. L. in *Therapeutic Ultrasound* 205–220 (Springer, 2016).

124. Lentacker, I., De Smedt, S. C. & Sanders, N. N. Drug loaded microbubble design for ultrasound triggered delivery. *Soft Matter* **5,** 2161–2170 (2009).

125. Kooiman, K., Vos, H. J., Versluis, M. & de Jong, N. Acoustic behavior of microbubbles and implications for drug delivery. *Advanced drug delivery reviews* **72,** 28–48 (2014).

126. Burke, C. W., Alexander IV, E., Timbie, K., Kilbanov, A. L. & Price, R. J. Ultrasound-activated agents comprised of 5FU-bearing nanoparticles bonded to microbubbles inhibit solid tumor growth and improve survival. *Molecular Therapy* **22,** 321–328 (2014).

127. Burke, C. W., Hsiang, Y.-H. J., Alexander IV, E., Kilbanov, A. L. & Price, R. J. Covalently Linking Poly (lactic-co-glycolic acid) Nanoparticles to Microbubbles Before Intravenous Injection Improves their Ultrasound-Targeted Delivery to Skeletal Muscle. *Small* **7,** 1227–1235 (2011).

128. De Cock, I., Lajoinie, G., Versluis, M., De Smedt, S. C. & Lentacker, I. Sonoprinting and the importance of microbubble loading for the ultrasound mediated cellular delivery of nanoparticles. *Biomaterials* **83,** 294–307 (2016).

129. Koczera, P. *et al.* PBCA-based polymeric microbubbles for molecular imaging and drug delivery. *Journal of controlled release* **259,** 128–135 (2017).

130. Van Wamel, A. *et al.* Acoustic Cluster Therapy (ACT) enhances the therapeutic efficacy of paclitaxel and Abraxane® for treatment of human prostate adenocarcinoma in mice. *Journal of controlled release* **236,** 15–21 (2016).

131. Klibanov, A. L. Targeted delivery of gas-filled microspheres, contrast agents for ultrasound imaging. *Advanced drug delivery reviews* **37,** 139–157 (1999).

132. Kiessling, F., Fokong, S., Koczera, P., Lederle, W. & Lammers, T. Ultrasound microbubbles for molecular diagnosis, therapy, and theranostics. *Journal of nuclear medicine* **53,** 345–348 (2012).

133. Ahmed, M. *et al.* Cellular uptake of plain and SPION-modified microbubbles for potential use in molecular imaging. *Cellular and molecular bioengineering* **10,** 537–548 (2017).

134. Prosperetti, A. Nonlinear oscillations of gas bubbles in liquids. Transient solutions and the connection between subharmonic signal and cavitation. *The Journal of the Acoustical Society of America* **57,** 810–821 (1975).

135. Gyöngy, M. & Coussios, C.-C. Passive spatial mapping of inertial cavitation during HIFU exposure. *IEEE Transactions on Biomedical Engineering* **57,** 48–56 (2009).

136. Shung, K. K. Diagnostic ultrasound: Past, present, and future. *J Med Biol Eng* **31,** 371–4 (2011).

137. Dubinsky, T. J., Cuevas, C., Dighe, M. K., Kolokythas, O. & Hwang, J. H. High-intensity focused ultrasound: current potential and oncologic applications. *American journal of roentgenology* **190,** 191–199 (2008).

138. Ter Haar, G. & Coussios, C. High intensity focused ultrasound: physical principles and devices. *International journal of hyperthermia* **23,** 89–104 (2007).

139. Miller, D. L. *et al.* Overview of therapeutic ultrasound applications and safety considerations. *Journal of Ultrasound in Medicine* **31,** 623–634 (2012).

140. May, P. C., Bailey, M. R. & Harper, J. D. Ultrasonic propulsion of kidney stones. *Current opinion in urology* **26,** 264 (2016).

141. Ninet, J. *et al.* Surgical ablation of atrial fibrillation with off-pump, epicardial, high-intensity focused ultrasound: results of a multicenter trial. *The Journal of thoracic and cardiovascular surgery* **130,** 803–e1 (2005).

142. Vaezy, S. *et al.* Liver Hemostasis With High-Intensity Ultrasound: Repair and Healing. *Journal of ultrasound in medicine* **23,** 217–225 (2004).

143. Kennedy, J. E. High-intensity focused ultrasound in the treatment of solid tumours. *Nature reviews cancer* **5,** 321 (2005).

144. Hsiao, Y.-H., Kuo, S.-J., Tsai, H.-D., Chou, M.-C. & Yeh, G.-P. Clinical application of high-intensity focused ultrasound in cancer therapy. *Journal of cancer* **7,** 225 (2016).

145. Voogt, M. *et al.* Volumetric feedback ablation of uterine fibroids using magnetic resonance-guided high intensity focused ultrasound therapy. *European radiology* **22,** 411–417 (2012).

146. Staruch, R., Chopra, R. & Hynynen, K. Localised drug release using MRI-controlled focused ultrasound hyperthermia. *International Journal of Hyperthermia* **27,** 156–171 (2011).

147. Bing, C. *et al.* Longer heating duration increases localized doxorubicin deposition and therapeutic index in Vx2 tumors using MR-HIFU mild hyperthermia and thermosensitive liposomal doxorubicin. *International Journal of Hyperthermia* **36,** 196–203 (2019).

148. Couture, O., Foley, J., Kassell, N. F., Larrat, B. & Aubry, J.-F. Review of ultrasound mediated drug delivery for cancer treatment: updates from pre-clinical studies. *Translational Cancer Research* **3,** 494–511 (2014).

149. Nesbitt, H. *et al.* Gemcitabine loaded microbubbles for targeted chemo-sonodynamic therapy of pancreatic cancer. *Journal of controlled release* **279,** 8–16 (2018).

150. Chowdhury, S. M. *et al.* Ultrasound-guided therapeutic modulation of hepatocellular carcinoma using complementary microRNAs. *Journal of Controlled Release* **238,** 272–280 (2016).

151. Kinoshita, M., McDannold, N., Jolesz, F. A. & Hynynen, K. Noninvasive localized delivery of Herceptin to the mouse brain by MRI-guided focused ultrasound-induced blood–brain barrier disruption. *Proceedings of the National Academy of Sciences* **103,** 11719–11723 (2006).

152. Kotopoulis, S., Dimcevski, G., Helge Gilja, O., Hoem, D. & Postema, M. Treatment of human pancreatic cancer using combined ultrasound, microbubbles, and gemcitabine: a clinical case study. *Medical physics* **40,** 072902 (2013).

153. Carpentier, A. *et al.* Clinical trial of blood-brain barrier disruption by pulsed ultrasound. *Science translational medicine* **8,** 343re2–343re2 (2016).

154. Miller, D. L. *et al.* Bioeffects considerations for diagnostic ultrasound contrast agents. *Journal of Ultrasound in Medicine* **27,** 611–632 (2008).

155. O'Brien Jr, W. D. Ultrasound–biophysics mechanisms. *Progress in biophysics and molecular biology* **93,** 212–255 (2007).

156. Jones, E. L. *et al.* Randomized trial of hyperthermia and radiation for superficial tumors. *Journal of Clinical Oncology* **23,** 3079–3085 (2005).

157. Dewhirst, M. W., Viglianti, B., Lora-Michiels, M., Hanson, M. & Hoopes, P. Basic principles of thermal dosimetry and thermal thresholds for tissue damage from hyperthermia. *International journal of hyperthermia* **19,** 267–294 (2003).

158. Watson, K. D. *et al.* Ultrasound increases nanoparticle delivery by reducing intratumoral pressure and increasing transport in epithelial and epithelial–mesenchymal transition tumors. *Cancer research* **72,** 1485–1493 (2012).

159. Lizzi, F. L. *et al.* Radiation-force technique to monitor lesions during ultrasonic therapy. *Ultrasound in medicine & biology* **29,** 1593–1605 (2003).

160. Hancock, H. A. *et al.* Investigations into pulsed high-intensity focused ultrasound–enhanced delivery: preliminary evidence for a novel mechanism. *Ultrasound in medicine & biology* **35,** 1722–1736 (2009).

161. Lawrie, A. *et al.* Ultrasound enhances reporter gene expression after transfection of vascular cells in vitro. *Circulation* **99,** 2617–2620 (1999).

162. Frenkel, V., Kimmel, E. & Iger, Y. Ultrasound-induced intercellular space widening in fish epidermis. *Ultrasound in medicine & biology* **26,** 473–480 (2000).

163. Hersh, D. S. *et al.* Pulsed ultrasound expands the extracellular and perivascular spaces of the brain. *Brain research* **1646,** 543–550 (2016).

164. O'Neill, B. E. *et al.* Pulsed high intensity focused ultrasound mediated nanoparticle delivery: mechanisms and efficacy in murine muscle. *Ultrasound in medicine & biology* **35,** 416–424 (2009).

165. Dymling, S. O., Persson, H. W., Hertz, T. G. & Lindström, K. A new ultrasonic method for fluid property measurements. *Ultrasound in medicine & biology* **17,** 497–500 (1991).

166. Dayton, P., Klibanov, A., Brandenburger, G. & Ferrara, K. Acoustic radiation force in vivo: a mechanism to assist targeting of microbubbles. *Ultrasound in Medicine and Biology* **25,** 1195–1201 (1999).

167. Dayton, P. A., Allen, J. S. & Ferrara, K. W. The magnitude of radiation force on ultrasound contrast agents. *The Journal of the Acoustical Society of America* **112,** 2183–2192 (2002).

168. Lum, A. F. *et al.* Ultrasound radiation force enables targeted deposition of model drug carriers loaded on microbubbles. *Journal of Controlled Release* **111,** 128–134 (2006).

169. Yuh, E. L. *et al.* Delivery of systemic chemotherapeutic agent to tumors by using focused ultrasound: study in a murine model. *Radiology* **234,** 431–437 (2005).

170. Frenkel, V. *et al.* Delivery of liposomal doxorubicin (Doxil) in a breast cancer tumor model: investigation of potential enhancement by pulsed-high intensity focused ultrasound exposure. *Academic radiology* **13,** 469–479 (2006).

171. Bednarski, M. D., Lee, J. W., Callstrom, M. R. & Li, K. C. In vivo target-specific delivery of macromolecular agents with MR-guided focused ultrasound. *Radiology* **204,** 263–268 (1997).

172. Dittmar, K. M. *et al.* Pulsed high-intensity focused ultrasound enhances systemic administration of naked DNA in squamous cell carcinoma model: initial experience. *Radiology* **235,** 541–546 (2005).

173. Zhou, Y. *et al.* Enhancement of small molecule delivery by pulsed high-intensity focused ultrasound: A parameter exploration. *Ultrasound in medicine & biology* **42,** 956–963 (2016).

174. Humphrey, V. F. Ultrasound and matter—Physical interactions. *Progress in biophysics and molecular biology* **93,** 195–211 (2007).

175. Unger, E., Porter, T., Lindner, J. & Grayburn, P. Cardiovascular drug delivery with ultrasound and microbubbles. *Advanced drug delivery reviews* **72,** 110–126 (2014).

176. Mitragotri, S. Healing sound: the use of ultrasound in drug delivery and other therapeutic applications. *Nature reviews Drug discovery* **4,** 255 (2005).

177. De Cock, I. *et al.* Ultrasound and microbubble mediated drug delivery: acoustic pressure as determinant for uptake via membrane pores or endocytosis. *Journal of controlled release* **197,** 20–28 (2015).

178. Helfield, B., Chen, X., Watkins, S. C. & Villanueva, F. S. Biophysical insight into mechanisms of sonoporation. *Proceedings of the National Academy of Sciences* **113,** 9983–9988 (2016).

179. Bazan-Peregrino, M., Arvanitis, C. D., Rifai, B., Seymour, L. W. & Coussios, C.-C. Ultrasound-induced cavitation enhances the delivery and therapeutic efficacy of an oncolytic virus in an in vitro model. *Journal of controlled release* **157,** 235–242 (2012).

180. Fan, C.-H. *et al.* Detection of intracerebral hemorrhage and transient blood-supply shortage in focused-ultrasound-induced blood–brain barrier disruption by ultrasound imaging. *Ultrasound in medicine & biology* **38,** 1372–1382 (2012).

181. McMahon, D. & Hynynen, K. Acute Inflammatory Response Following Increased Blood-Brain Barrier Permeability Induced by Focused Ultrasound is Dependent on Microbubble Dose. *Theranostics* **7,** 3989 (2017).

182. Kovacs, Z. I., Burks, S. R. & Frank, J. A. Focused ultrasound with microbubbles induces sterile inflammatory response proportional to the blood brain barrier opening: Attention to experimental conditions. *Theranostics* **8,** 2245 (2018).

183. Weng, J.-C., Wu, S.-K., Yang, F.-Y., Lin, W.-L. & Tseng, W.-Y. I. Pulse sequence and timing of contrast-enhanced MRI for assessing blood–brain barrier disruption after transcranial focused ultrasound in the presence of hemorrhage. *Journal of Magnetic Resonance Imaging* **31,** 1323–1330 (2010).

184. Olive, K. P. *et al.* Inhibition of Hedgehog signaling enhances delivery of chemotherapy in a mouse model of pancreatic cancer. *Science* **324,** 1457–1461 (2009).

185. Djabourov, M., Lechaire, J.-P. & Gaill, F. Structure and rheology of gelatin and collagen gels. *Biorheology* **30,** 191–205 (1993).

186. Chen, X., Nadiarynkh, O., Plotnikov, S. & Campagnola, P. J. Second harmonic generation microscopy for quantitative analysis of collagen fibrillar structure. *Nature protocols* **7,** 654 (2012).

187. Brown, E. & McKee, T. E. diTomaso, A. Pluen, B. Seed, Y. Boucher, and RK Jain,"Dynamic imaging of collagen and its modulation in tumors in vivo using second-harmonic generation,". *Nat. Med* **9,** 796–801 (2003).

188. Campagnola, P. *Second harmonic generation imaging microscopy: applications to diseases diagnostics* 2011.

189. Cicchi, R. *et al.* From molecular structure to tissue architecture: collagen organization probed by SHG microscopy. *Journal of biophotonics* **6,** 129–142 (2013).

190. Kotopoulis, S. *et al.* Sonoporation-enhanced chemotherapy significantly reduces primary tumour burden in an orthotopic pancreatic cancer xenograft. *Molecular imaging and biology* **16,** 53–62 (2014).

191. Burke, C. W., Klibanov, A. L., Sheehan, J. P. & Price, R. J. Inhibition of glioma growth by microbubble activation in a subcutaneous model using low duty cycle ultrasound without significant heating. *Journal of neurosurgery* **114,** 1654–1661 (2011).

192. Sulheim, E. *et al.* Multi-modal characterization of vasculature and nanoparticle accumulation in five tumor xenograft models. *Journal of controlled release* **279,** 292–305 (2018).

193. Cho, E. E., Drazic, J., Ganguly, M., Stefanovic, B. & Hynynen, K. Two-Photon Fluorescence Microscopy Study of Cerebrovascular Dynamics in Ultrasound-Induced Blood—Brain Barrier Opening. *Journal of Cerebral Blood Flow & Metabolism* **31,** 1852–1862 (2011).

194. Raymond, S. B., Skoch, J., Hynynen, K. & Bacskai, B. J. Multiphoton imaging of ultrasound/Optison mediated cerebrovascular effects in vivo. *Journal of Cerebral Blood Flow & Metabolism* **27,** 393–403 (2007).

195. Burgess, A., Nhan, T., Moffatt, C., Klibanov, A. & Hynynen, K. Analysis of focused ultrasound-induced blood–brain barrier permeability in a mouse model of Alzheimer's disease using two-photon microscopy. *Journal of controlled release* **192,** 243–248 (2014).

196. Garbin, V. *et al.* Changes in microbubble dynamics near a boundary revealed by combined optical micromanipulation and high-speed imaging. *Applied physics letters* **90,** 114103 (2007).

197. Kudo, N., Okada, K. & Yamamoto, K. Sonoporation by single-shot pulsed ultrasound with microbubbles adjacent to cells. *Biophysical journal* **96,** 4866–4876 (2009).

198. Fan, Z., Liu, H., Mayer, M. & Deng, C. X. Spatiotemporally controlled single cell sonoporation. *Proceedings of the National Academy of Sciences* **109,** 16486–16491 (2012).

199. Helfield, B. L., Leung, B. Y. & Goertz, D. E. The effect of boundary proximity on the response of individual ultrasound contrast agent microbubbles. *Physics in Medicine & Biology* **59,** 1721 (2014).

200. Caskey, C. F., Stieger, S. M., Qin, S., Dayton, P. A. & Ferrara, K. W. Direct observations of ultrasound microbubble contrast agent interaction with the microvessel wall. *The Journal of the Acoustical Society of America* **122,** 1191–1200 (2007).

201. Chen, H., Brayman, A. A., Bailey, M. R. & Matula, T. J. Blood vessel rupture by cavitation. *Urological research* **38,** 321–326 (2010).

202. Chen, H., Kreider, W., Brayman, A. A., Bailey, M. R. & Matula, T. J. Blood vessel deformations on microsecond time scales by ultrasonic cavitation. *Physical review letters* **106,** 034301 (2011).

203. Goertz, D. E. *et al.* Antitumor effects of combining docetaxel (taxotere) with the antivascular action of ultrasound stimulated microbubbles. *PloS one* **7,** e52307 (2012).

204. Hu, X. *et al.* Insonation of targeted microbubbles produces regions of reduced blood flow within tumor vasculature. *Investigative radiology* **47,** 398 (2012).

205. Keravnou, C. P., De Cock, I., Lentacker, I., Izamis, M.-L. & Averkiou, M. A. Microvascular injury and perfusion changes induced by ultrasound and microbubbles in a machine-perfused pig liver. *Ultrasound in medicine & biology* **42,** 2676–2686 (2016).

206. Belcik, J. T. *et al.* Augmentation of limb perfusion and reversal of tissue ischemia produced by ultrasound-mediated microbubble cavitation. *Circulation: Cardiovascular Imaging* **8,** e002979 (2015).

207. Wood, A. K., Schultz, S. M., Lee, W. M., Bunte, R. M. & Sehgal, C. M. Antivascular ultrasound therapy extends survival of mice with implanted melanomas. *Ultrasound in medicine & biology* **36,** 853–857 (2010).

208. Vlachos, F., Tung, Y.-S. & Konofagou, E. Permeability dependence study of the focused ultrasound-induced blood–brain barrier opening at distinct pressures and microbubble diameters using DCE-MRI. *Magnetic resonance in medicine* **66,** 821–830 (2011).

209. De L Davies, C., Berk, D., Pluen, A. & Jain, R. Comparison of IgG diffusion and extracellular matrix composition in rhabdomyosarcomas grown in mice versus in vitro as spheroids reveals the role of host stromal cells. *British journal of cancer* **86,** 1639 (2002).

210. Wang, C., Jalikop, S. V. & Hilgenfeldt, S. Size-sensitive sorting of microparticles through control of flow geometry. *Applied Physics Letters* **99,** 034101 (2011).

211. Erni, R., Rossell, M. D., Kisielowski, C. & Dahmen, U. Atomic-resolution imaging with a sub-50-pm electron probe. *Physical review letters* **102,** 096101 (2009).

212. Dayton, P. A. *et al.* Application of ultrasound to selectively localize nanodroplets for targeted imaging and therapy. *Molecular imaging* **5,** 7290–2006 (2006).

213. Eggen, S. *et al.* Ultrasound improves the uptake and distribution of liposomal Doxorubicin in prostate cancer xenografts. *Ultrasound in medicine & biology* **39,** 1255–1266 (2013).

214. Mercado, K. P., Helguera, M., Hocking, D. C. & Dalecki, D. Noninvasive quantitative imaging of collagen microstructure in three-dimensional hydrogels using high-frequency ultrasound. *Tissue Engineering Part C: Methods* **21,** 671–682 (2015).

215. Chandran, P. L. & Barocas, V. H. Microstructural mechanics of collagen gels in confined compression: poroelasticity, viscoelasticity, and collapse. *Journal of biomechanical engineering* **126,** 152–166 (2004).

216. Knapp, D. M. *et al.* Rheology of reconstituted type I collagen gel in confined compression. *Journal of Rheology* **41,** 971–993 (1997).

217. Forster, J. C., Harriss-Phillips, W. M., Douglass, M. J. & Bezak, E. A review of the development of tumor vasculature and its effects on the tumor microenvironment. *Hypoxia* **5,** 21 (2017).

218. Mo, S. *et al.* Increasing the density of nanomedicines improves their ultrasound-mediated delivery to tumours. *Journal of Controlled Release* **210,** 10–18 (2015).

219. Lea-Banks, H., Teo, B., Stride, E. & Coussios, C. C. The effect of particle density on ultrasound-mediated transport of nanoparticles. *Physics in Medicine & Biology* **61,** 7906 (2016).

220. Lélu, S., Strand, S. P., Steine, J. & Davies, C. d. L. Effect of PEGylation on the diffusion and stability of chitosan–DNA polyplexes in collagen gels. *Biomacromolecules* **12,** 3656–3665 (2011).

221. Wu, S.-K. *et al.* Characterization of different microbubbles in assisting focused ultrasound-induced blood-brain barrier opening. *Scientific reports* **7,** 46689 (2017).

222. Miller, M. W. & Ziskin, M. C. Biological consequences of hyperthermia. *Ultrasound in medicine & biology* **15,** 707–722 (1989).

Paper I

This paper was published in UMB, July 2019.

Ultrasound in Med. & Biol., Vol. 45, No. 11, pp. 3028–3041, 2019

0301-5629/$ - see front matter

https://doi.org/10.1016/j.ultrasmedbio.2019.07.683

● *Original Contribution*

EFFECT OF ULTRASOUND ON THE VASCULATURE AND EXTRAVASATION OF NANOSCALE PARTICLES IMAGED IN REAL TIME

Petros T. Yemane,* Andreas K.O. Åslund,*,†,‡ Sofie Snipstad,*,†,§ Astrid Bjørkøy,* Kristin Grendstad,* Sigrid Berg,§,¶,‖ Yrr Mørch,† Sverre H. Torp,#,** Rune Hansen,¶,‖ and Catharina de Lange Davies*

* Department of Physics, Norwegian University of Science and Technology, Trondheim, Norway; † Department of Biotechnology and Nanomedicine, SINTEF Industry, Trondheim, Norway; ‡ Stroke Unit, Department of Internal Medicine, St. Olav's Hospital, Trondheim, Norway; § Cancer Clinic, St. Olav's Hospital, Trondheim, Norway; ¶ Department of Circulation and Medical Imaging, Norwegian University of Science and Technology, Trondheim, Norway; ‖ Department of Health Research, SINTEF Digital, Trondheim, Norway; # Department of Pathology, St. Olav's Hospital, Trondheim, Norway; and ** Department of Clinical and Molecular Medicine, Norwegian University of Science and Technology, Trondheim, Norway

(*Received* 3 *June* 2019; *revised* 31 *July* 2019; *in final from* 31 *July* 2019)

Abstract—Ultrasound and microbubbles have been found to improve the delivery of drugs and nanoparticles to tumor tissue. To obtain new knowledge on the influence of vascular parameters on extravasation and to elucidate the effect of acoustic pressure on extravasation and penetration of nanoscale particles into the extracellular matrix, real-time intravital multiphoton microscopy was performed during sonication of tumors growing in dorsal window chambers. The impact of vessel diameter, vessel structure and blood flow was characterized. Fluorescein isothiocyanate–dextran (2 MDa) was injected to visualize blood vessels. Mechanical indexes (MI) of 0.2–0.8 and in-house-made, nanoparticle-stabilized microbubbles or Sonovue were applied. The rate and extent of penetration into the extracellular matrix increased with increasing MI. However, to achieve extravasation, smaller vessels required MIs (0.8) higher than those of blood vessels with larger diameters. Ultrasound changed the blood flow rate and direction. Interestingly, the majority of extravasations occurred at vessel branching points. (E-mail: Catharina.davies@ntnu.no)

Key Words: **Ultrasound, Microbubbles, Real-time imaging, Multiphoton microscope, Cavitation, Blood flow, Vascular structure, Nanoparticle delivery.**

INTRODUCTION

Intravenous delivery of therapeutic agents to tumors in patients in optimal quantities with limited exposure to normal tissue is challenging (Tannock et al. 2002). The administered drugs cause severe side effects because of their accumulation in healthy tissue (Coates et al. 1983). Encapsulating therapeutic drugs into nanoparticles (NPs) might enhance the tumor uptake of drugs and reduce the toxic effects on healthy tissue through the enhanced permeability and retention effect (Maeda et al. 2000). However, an improved therapeutic response has not been reported in the clinic (Lammers et al. 2012). A recent meta-analysis of pre-clinical studies in the last 10 y found that only 0.7% of the injected NPs accumulated in tumors (Wilhelm et al. 2016). The primary reason for this finding is that the NPs must pass several physiologic barriers before reaching the diseased cells (Anchordoquy et al. 2017; Mullick Chowdhury et al. 2017; Wang et al. 2014a).

The distribution of NPs in tumors is notably heterogeneous, and NPs are mainly located close to the capillary wall (Boissenot et al. 2016; Eggen et al. 2014; Lammers et al. 2012). Thus, a more efficient method for delivering therapeutic agents is needed.

Focused ultrasound (FUS) and systemic administration of microbubbles (MBs) have been reported to improve the delivery and therapeutic response of drugs

Address correspondence to: Catharina de Lange Davies, Department of Physics, Norwegian University of Science and Technology, Høgskoleringen 5, 7491 Trondheim Norway. E-mail: Catharina.davies@ntnu.no

and NPs in pre-clinical studies (Kotopoulis et al. 2014; Lammertink et al. 2015; Snipstad et al. 2017; Treat et al. 2012; van Wamel et al. 2016). A clinical study in which patients with non-resectable pancreatic tumors were treated with gemcitabine combined with FUS and MBs reported improved therapeutic response in a subgroup of patients (Dimcevski et al. 2016). FUS and MBs have also been found to open the blood–brain barrier, both in pre-clinical studies (Åslund et al. 2015; Hynynen et al. 2001; Liu et al. 2010; Nhan et al. 2013; Wei et al. 2013) and in humans (Carpentier et al. 2016; Mainprize et al. 2019).

The exact mechanisms underlying FUS- and MB-mediated drug delivery have not been thoroughly elucidated to date. Ultrasound (US)-induced bio-effects can be divided into thermal and non-thermal effects. The thermal effect is generally not considered to play a major role in microbubble-assisted treatments at relatively low mechanical indexes (MIs). The non-thermal effects are due to mechanical effects through acoustic radiation force and cavitation which is considered to be the most important mechanism for therapeutic applications when US is used in combination with MBs (Hernot and Klibanov 2008). The acoustic radiation force is the transfer of momentum from the US wave, which causes the translation of particles (Antonios and James 2016) and MBs (Dayton et al. 1999) in the direction of US wave propagation. Cavitation is the formation and volumetric oscillation of MBs in response to the pressure amplitude of the US wave. A stable volumetric oscillation of MBs at equilibrium radius for many acoustic cycles is called *stable cavitation*, whereas a large and unstable expansion of the bubble during the acoustic wave at higher pressures, which results in violent collapse, is known as *inertial cavitation*.

Cavitation in a medium depends strongly on the acoustic parameters and the presence and size of MBs. Acoustic parameters such as pressure and frequency can alter the MB response from stable cavitation to inertial cavitation. It has been reported that pulse duration is also highly important for the onset of the stable and inertial cavitation of MBs (Wang et al. 2015). In addition, MB concentration and size will significantly affect cavitation activity (McMahon and Hynynen 2017; Wang et al. 2014b). In addition, the space available for the MBs to oscillate and the proximity to the vessel wall are of great importance for the effect of cavitation on the vessel wall and, thus, the outcome of US-mediated drug delivery (Garbin et al. 2007; Helfield et al. 2014).

Cavitation-induced bio-effects caused by MBs oscillating close to the vessel wall include acoustic microstreaming, shock waves and microjetting, the latter caused by the violent collapse of bubbles; all create temporary and/or permanent gaps in the blood vessel walls (Chen et al. 2010, 2011). Cavitation-induced mechanical force that can distend and invaginate the vessel wall could also enhance vascular permeability (Caskey et al. 2007; Chen et al. 2011). These cavitation-induced bio-effects can also create unwanted and unintended permanent damage to the blood vessel. However, cavitation can be exploited for drug delivery if the US parameters are well optimized.

To understand in more detail how US and MBs enhance the permeability of biological barriers, direct observation of the behavior of the bubbles in real time is necessary (Caskey et al. 2007; Chen et al. 2011; Helfield et al. 2016; Raymond et al. 2007). Thus, tumors were grown in dorsal window chambers, which enabled us to simultaneously apply US and image the vasculature by intravital multiphoton microscopy. We compared two different MBs: in-house-made MBs stabilized by polymeric NPs (NPMBs) (Mørch et al. 2015) and Sonovue co-administered with the same polymeric NPs during FUS. NPs were administered with Sonovue to compare the efficacy of the two MBs on the extravasation of the NPs. Because the fluorescence from the NPs is not homogenous enough to delineate the blood vessels, dextran (2 MDa) was injected to visualize the blood vessel and to study the extravasation of the dextran. The aim was to reveal vascular parameters as well as NP and MB behavior influencing extravasation and the effect of different MIs on extravasation and penetration of NPs into the extracellular matrix. In particular, we imaged whether the blood flow, the vascular structure and the size of the vessel influenced where extravasations could be detected. Moreover, histologic examination of paraffin sections of the tissue was performed to evaluate tissue damage.

METHODS

Cell culture

A human osteosarcoma cell line (OHS) was used (Fodstad et al. 1986). Cells were grown in Roswell Park Memorial Institute-1640 medium (Gibco Thermo-Fisher, 21875-034, Oslo, Norway) supplemented with 10% fetal bovine serum (Sigma-Aldrich, Oslo, Norway), 100 U/mL penicillin and 100 μg/mL streptomycin (Sigma-Aldrich) at 37°C and 5% CO_2.

Animal model and dorsal window chamber implantation

A previous study had found that OHS tumors are well vascularized throughout the tumor and have no necrotic core (Sulheim et al. 2018). The OHS tumors were grown as xenografts in male BALB/c nude mice (weight: 23–30 g, Janvier, Le Genest-Saint-Isle, France) in dorsal skinfold window chambers (Fig. 1a).

Dorsal skinfold window chamber surgery was carried out as previously described by Hak et al. (2010). Briefly, the double layer of the skin was sandwiched between two symmetric frames, and a circular area

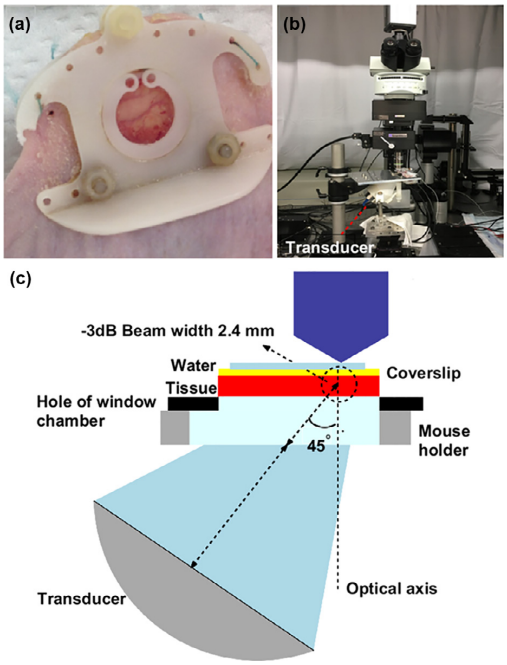

Fig. 1. Schematic of the US and multiphoton microscope setup for US–microbubble-mediated drug delivery in a skin flap dorsal window chamber. (a) Dorsal window chamber. (b) Experimental setup. (c) US and objective/light beam alignment (not drawn to scale). US = ultrasound.

15 mm in diameter was removed from the skin on one side of the fold. The remaining layers of the other skinfold (thin striated skin muscle, subcutaneous tissue, dermis and epidermis) were covered with a glass coverslip, which was incorporated into one of the chamber frames and formed a window to the tissue. The next day, 30 μL containing 5×10^6 OHS cells were implanted in the window chamber. Tumors were grown for 2 wk before treatment. The tumor thickness was limited by the window chamber, while the diameter in the longest direction was typically 5–10 mm. The animals tolerated the chambers well and exhibited no signs of discomfort. The water for the animals was supplemented with 25 mg/mL Baytril (Bayer, Oslo, Norway), and they were kept in separate cages after the window chamber was implanted. All surgical and imaging procedures were performed with the animal anesthetized by a subcutaneous injection of fentanyl (0.05 mg/kg, Actavis Group HF)/medetomidine (0.5 mg/kg, Orion Pharma)/midazolam (5 mg/kg Accord Healthcare Limited)/water (2:1:2:5) at a dose of 0.1 mL per 10 g weight. All animal experiments were approved by the Norwegian Animal Research Authorities, that is, the Norwegian Food Safety Authority.

Nanoparticles and microbubbles

In-house self-assembled NP-stabilized MBs (mean diameter of 2.4 ±0.2 μm, SINTEF, Trondheim, Norway) and the commercial phospholipid-shelled Sonovue (mean diameter = 2.5 μm, Bracco, Milan, Italy) were used. The size distribution of the two MB types is illustrated in Supplementary Figure S1 (online only). Briefly, poly(2-ethylbutyl cyanoacrylate) [PEBCA] NPs were synthesized by mini-emulsion polymerization and contained the dye NR668 (2%, modified Nile Red, custom synthesis) (Klymchenko et al. 2012; Mørch et al. 2015), which possess excitation and emission maxima of 548 and 621 nm, respectively. The PEBCA NPs were used to make NPMBs by mixing casein and perfluoropropane gas using an Ultra-Turrax at 24,000 rpm for 4 min. The resulting NPMB solution contained an excess of free NPs.

Before each sonication, 30 μL (4 mg/mL, diluted in saline) of 2 MDa fluorescein isothiocyanate (FITC)–dextran (Sigma-Aldrich) was injected through the tail vein to visualize the blood vessels. Mice in the NPMB groups were given a bolus injection of 50 μL of NPMBs ($2–5 \times 10^8$ MBs/mL, 10 mg/mL NPs), whereas mice in the Sonovue groups received 25 μL (20 mg/mL, diluted in 0.01 M phosphate buffer) of free PEBCA NPs before injection of 50 μL of Sonovue ($2–5 \times 10^8$ MBs/mL).

Ultrasound exposure setup

An experimental setup that enabled the application of US while imaging the dorsal window chamber with multiphoton microscopy was established. Figure 1 (b, c) is a schematic of the experimental setup. The US beam (at the region of interest [ROI]) was aligned with the focus of the objective using a custom-built 3D printed cone and calibrated fiberoptic hydrophone system (Precision Acoustics Ltd, Dorchester, UK) by monitoring the output pressure on an oscilloscope (TDS 210, Tektronix, Bracknell, UK). The cone was manufactured with inner diameters at top and bottom of 15 and 68 mm, respectively, and a cone length of 74 mm. The transducer was mounted on the bottom of the cone, and the cone was filled with distilled and degassed water. The axis of the US beam was 45° with respect to the imaging plane to minimize reflections from the glass of the window chamber and reduce standing wave formation. An ultrasonic coupling gel filled the gap between the tip of the cone and the skin of the mice.

Ultrasound parameters

A single-element focused transducer (Precision Acoustics Ltd,) with a 1-MHz center frequency, 60-mm diameter and 75-mm curvature was used. US pulses were generated by an arbitrary waveform generator (AWFG, 33522 A, Agilent Technologies, Santa Clara, CA, USA) and amplified by a 50-dB power amplifier

Table 1. Overview of the treated groups and number of observed extravasations

Group	NPMBs					Sonovue	
MI	0.2	0.4	0.6*	0.8	0.2†	0.4	0.8
Number of animals with PRF = 0.5 Hz (0.1 Hz)	5 (1)	5 (4)	3 (0)	9 (1)	4 (0)	6 (2)	5 (4)
Total number of treatments with PRF = 0.5 Hz (0.1 Hz)	7 (2)	9 (8)	6 (0)	15 (1)	4 (0)	9 (4)	9 (8)
Percentage of treatments in which extravasation occurred within the five regions imaged per total number of treatments with PRF = 0.5 Hz (0.1 Hz)	14% (100%)	56% (38%)	33% (0%)	73% (100%)	0%	22% (100%)	44% (88%)
Percentage of treatments in which extravasations were observed live during treatment per total number of treatments with PRF = 0.5 Hz (0.1 Hz)	14% (100%)	11% (38%)	17% (0%)	40% (100%)	0%	11% (50%)	0% (63%)
Total number of extravasations within the five regions imaged with PRF = 0.5 Hz (0.1 Hz)‡	2 (10)	5 (17)	5 (0)	45 (2)	0	10 (6)	9 (20)
Total number of extravasations observed during live imaging with PRF = 0.5 Hz (0.1 Hz)‡	2 (3)	1 (7)	3 (0)	15 (2)	0	2 (3)	0 (10)

MI = mechanical index; NPMBs = in-house-made MBs stabilized by polymeric nanoparticles; PRF = pulse repetition frequency.
Note: Some animals were treated at two MIs (low and high) at one position if no extravasation was observed at the lower MI.
* Few animals were treated and exhibited only three extravasations during live imaging at an MI of 0.6 combined with NPMBs (data are used only for analysis of vessel diameter and time of extravasation).
† Few animals were treated at a MI of 0.2, and no extravasation was observed during live imaging.
‡ In one treatment, multiple extravasations occurred.

(2100 L amplifier, ENI, USA). The transducer was characterized in a water tank measurement system (AIMS-III, Onda Corp.), and the pressure and −3-dB beam width at the ROI were measured with a calibrated HGL-0200 hydrophone (Onda Corp.) using an AH-2010 preamplifier (Onda Corp.). The −3-dB beam width at the target was 2.4 mm. The transducer was characterized both with and without the cone, and no differences in beam profile or pressure were found.

The tumor was sonicated with US pulses with a center frequency of 1 MHz, pulse length of 10 ms and pulse repetition frequency (PRF) of 0.5 or 0.1 Hz to allow MBs to reperfuse into the treatment area in the time between transmit pulses. The total duration of sonication was 5 min and was chosen based on the circulation half-life of the MBs. The circulation half-time of NPMBs is approximately 1.5−2 times longer than for Sonovue, which is 1 min (Schneider 1999; Wu et al. 2017). Peak negative pressure amplitudes of 0.2, 0.4, 0.6 and 0.8 MPa, which were measured in water, were applied.

Treatment groups and controls

An overview of the different treatment groups and the number of mice treated is provided in Table 1. In total, 36 mice (18 mice each for the NPMB and Sonovue groups) were used. Eight mice (5 for the NPMB group and 3 for the Sonovue group) received two different MIs (low MI [0.2 and 0.4] and high MI [0.6 and 0.8]) at the same position, and each mouse was treated in two different positions (Fig. 2b). Thus, in Table 1, a single mouse is counted in multiple different MI groups in some cases. Every mouse received US, and pre-images were recorded as control before US was applied for every treatment (Fig. 2a). To study blood flow and possible extravasation before US and MB injection, mice (n = 16) received an intravenous injection of FITC−dextran and were imaged for 3−5 min. Subsequently, NPMBs (n = 4) or NPs and Sonovue (n = 3) were injected, and the tumor was imaged at the same field of view (FOV) for an additional 5 min before sonication. The remaining mice (n = 9) received US immediately after NPs and MBs were injected; that is,

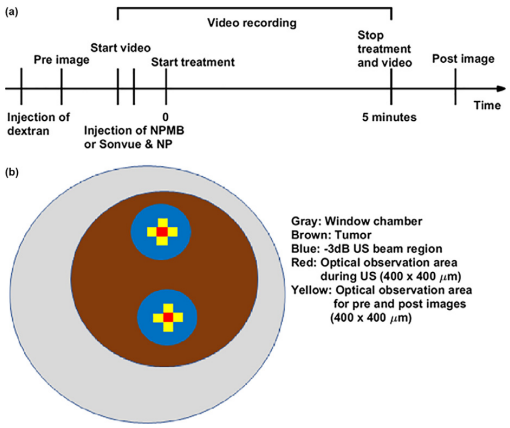

Fig. 2. (a) Treatment and imaging schedule. (b) Two treatment areas and imaging areas where images were acquired before, during and after US. After 2-MDa fluorescein isothiocyanate−dextran was injected, multiphoton pre-images were acquired (*yellow*), video recording started (*red*) and NPMBs or Sonovue MB and NPs were injected before sonication started (*blue*). After US, post-images were acquired. MB = microbubbles; NP = nanoparticles; NPMB = nanoparticle-stabilized microbubbles; US = ultrasound.

the effects of NPs and MBs on blood flow and extravasation were not imaged before US exposure.

Real-time multiphoton microscope imaging during ultrasound exposure

Mice with dorsal window chambers were anesthetized and positioned on a custom-designed microscope stage with a heating device maintaining the body temperature at 37°C, as illustrated in Figure 1. The tail vein was cannulated for intravenous administration. The treatment and imaging schedule are illustrated in Figure 2a.

The multiphoton microscope (*in vivo* SliceScope, Scientifica, Uckfield, UK) was equipped with a 20 × water dipping objective (XLUMPLFLN20 XW from Olympus, numerical aperture (NA) = 1.0 working distance 2 mm) and a pulsed MaiTai DeepSee (Spectra-Physics, Mountain View CA, USA) laser. The excitation wavelength was 790 nm. Images were acquired in resonant scanning mode at 31 frames per second (fps; 512 × 512 pixels) with a FOV of 400 × 400 μm. The filters in front of the two GaAsp detectors were long pass 590 nm and bandpass 525/50 nm for the detection of NPs with NR668 and FITC−dextran, respectively.

After pre-images of the vessels were acquired at the five neighboring positions (one red and four yellow) illustrated in Figure 2b, video-rate imaging started at the red area immediately before NPMBs or Sonovue and NPs were injected. US exposure started immediately after injection of the MBs. The video was recorded during the 5-min sonication.

After sonication, images were immediately recorded in the four yellow areas to observe any change during US exposure. Because the diameter of the tumor and the −3-dB US beam width are 5−10 and 2.4 mm, respectively, US exposure was performed in two different areas in each window chamber (Fig. 2b).

Histologic evaluation

All mice were euthanized by cervical dislocation. The tumor tissue was harvested and fixed in 4% buffered formaldehyde and embedded in paraffin. Finally, 5-μm-thick sections of the tissues from three different depths separated by 100 μm were prepared. The tissue was stained with hematoxylin, erythrosine and saffron (HES) to evaluate tissue damage after US treatment. A pathologist blinded to the study evaluated the tissue sections.

Image analysis

Images were analyzed using ImageJ (National Institutes of Health, Bethesda, MD, USA) and MATLAB (The MathWorks, Natick, MA, USA). To enhance the quality of the images, video frame averaging of several consecutive images was performed in ImageJ, as explained below. Then, the images were loaded into MATLAB. First, the images were median filtered (3 × 3 neighborhood) and segmented automatically.

Vascular masks (Supplementary Fig. S2, online only) were created using the first frame of the video of the FITC−dextran signal. In videos where extensive extravasation of NPs and dextran was observed, three consecutive images were averaged (compromise between the quality of the image and the time resolution). Then, a circle with the radius of the blood vessel and concentric circles spaced by 3 pixels (2.23 μm) starting from the center of the blood vessel were drawn. The normalized signal intensity (with respect to the maximum intensity in the whole image) of NPs and dextran within the blood vessel and in the different annuli over both time and distance were computed with the background subtracted. Then, the penetration of the NPs and dextran was estimated. Moreover, intravascular and extravascular accumulation (from the blood vessel wall until 50 μm into the extracellular matrix) of average fluorescence intensities of NPs and dextran were determined with the background subtracted. During extravascular analysis, video frame averaging of 15 consecutive images was performed. Some vessels were excluded from analysis of extravasation and penetration of the dextran and NPs if the source of the extravasation was uncertain. In addition, the average diameter of the blood vessel where extravasation was observed was computed from the pre-images (from both the *red* and *yellow* regions in Fig. 2b). The speed of NPs was estimated by tracking the distance NPs moved inside the vessels between subsequent frames. From 60 to 80 NPs were analyzed for each group. The occurrence of change in blood flow direction was determined by visual observations both before and during US. Any change in flow direction observed during the live imaging was counted as one occurrence; in other words, the total number of changes in blood flow direction is not given. The change in the flux of dextran in the blood vessels before and during US was estimated by measuring the intensity of FITC−dextran in a circular ROI drawn in blood vessels. A supplement is provided for detailed description of the method and some supplementary results (online only).

Statistical analysis

Data are presented as the mean value ± standard deviation. Analysis of variance was used for comparisons of differences between treatment groups in a confirmatory test. The Tukey−Kramer test (p value ≤ 0.05) was used to determine which pairwise comparisons were significant.

RESULTS

The effect of US combined with MBs on the extravasation of 2-MDa dextran and NPs was imaged in real time by intravital multiphoton microscopy during US sonication.

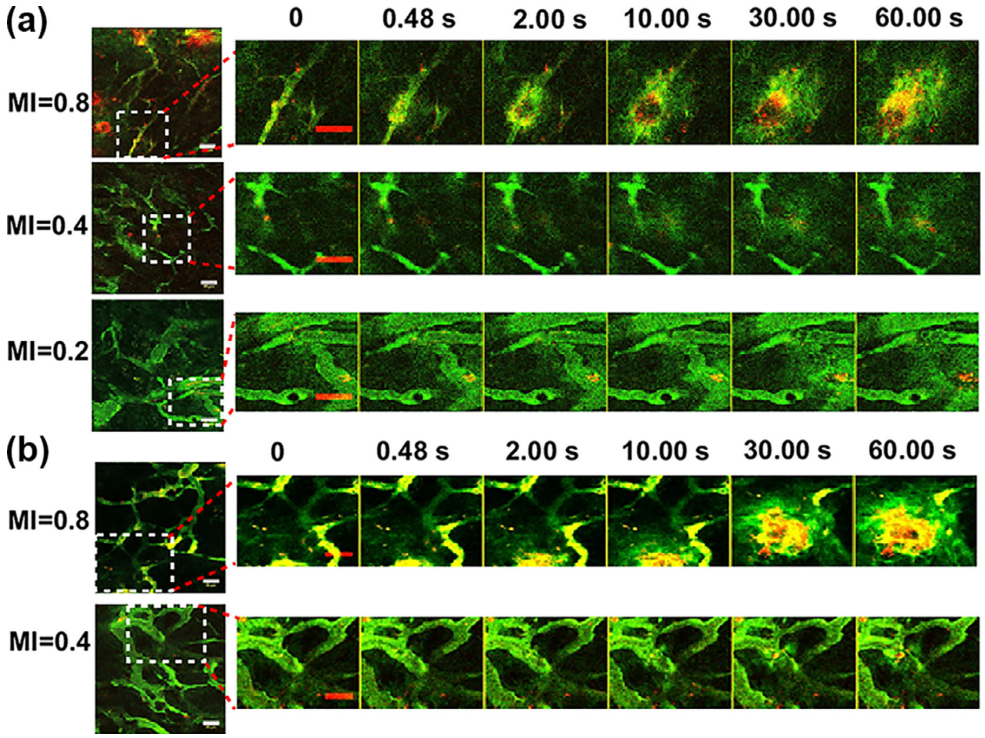

Fig. 3. Examples of extravasation and distribution of nanoparticles (*red*) and dextran (*green*) as a function of time after opening of the blood vessel wall by ultrasound and microbubbles with (a) nanoparticle-stabilized microbubbles at MIs of 0.8, 0.4 and 0.2 and (b) Sonovue at MIs of 0.8 and 0.4. Zero time corresponds to the time immediately before the extravasation event occurred. Bar = 50 μm. MI = mechanical index.

We observed extravasation and penetration of dextran and NPs into the extracellular matrix at all MIs tested and found a correlation between blood vessel diameter at which extravasation of NPs and dextran occurred and MI. Changes in flow rate and flow direction were observed, and occasionally, the blood flow stopped for short periods.

US-Induced extravasation of 2-MDa dextran and NPs

Representative images of extravasation of NPs (*red*) and dextran (*green*) from the blood vessel into the extracellular matrix as a function of time are shown in Figure 3, Supplementary Figure S3 (online only) and Supplementary Videos S1−S5 (online only). Extravasation of NPs and dextran was observed after sonication at MIs of 0.8, 0.4 and 0.2 when injecting NPMBs (Fig. 3a) and at MIs of 0.8 and 0.4 when injecting Sonovue (Fig. 3b). No extravasation of NPs and dextran was observed using an MI of 0.2 after administration of Sonovue. Because the NPMB solution also contains free NPs, the red signal observed in the videos could be NPMBs, free NPs or aggregated NPs.

The number and percentage of extravasation events (both NPs and dextran) per total number of treatments are given in Table 1. Both the number of extravasations in the FOV during US imaging and the number of extravasations counted in the five areas imaged after treatment are presented. Comparison of the two MBs reveals that the percentage of extravasation occurrence per total number of treatments at a PRF of 0.5 is higher for NPMBs than Sonovue at MIs of 0.8 (73% vs. 44%) and 0.4 (56% vs. 22%). After use of a lower PRF at 0.1 Hz, the total number of treatments in which extravasation occurred in the FOV (during live imaging) and in the five areas imaged after US exposure increased substantially.

The observed extravasation of NPs and dextran occurred at different time points and locations and occurred within milliseconds to minutes after the onset of US exposure (Fig. 4). The number of extravasation events was not particularly high immediately after administration of MBs when the concentration of MBs was highest. However, most of the extravasations occurred within the circulation half-life of the two MBs at higher MIs (3/3

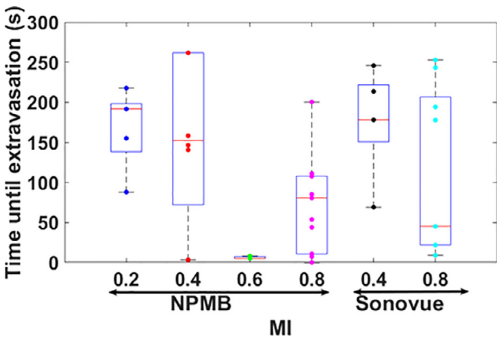

Fig. 4. Time point at which extravasation occurred after onset of US exposure. Both the data points and box-and-whisker plots are shown. Each point represents one blood vessel where extravasation was observed, and the *red line* in box-and-whisker plots represents the median. For NPMBs at MI = 0.2 (n = 5), MI = 0.4 (n = 8), MI = 0.6 (n=3) and MI = 0.8 (n = 17), and for Sonovue at MI = 0.4 (n=5) and MI = 0.8 (n=10) where n = number of blood vessels. Note: Because more than one extravasation could occur at the same time point in different vessels, two or more circles could be merged together. MI = mechanical index; NPMB = nanoparticle-stabilized microbubbles.

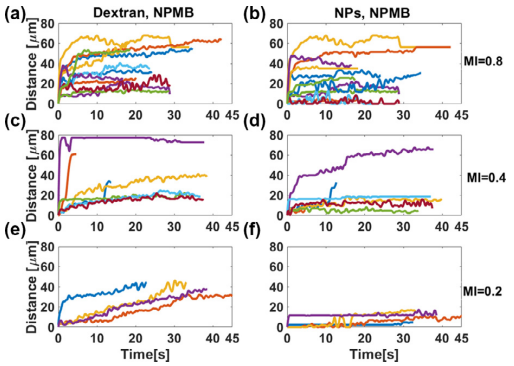

Fig. 5. Penetration of dextran and NPs for NPMBs at various MIs. MI = 0.8 for dextran (a) and NPs (b) (n = 12). MI = 0.4 for dextran (c) and NPs (d) (n = 7). MI = 0.2 for dextran (e) and NPs (f) (n = 4). Zero time corresponds to the time immediately before opening of the blood vessel by the ultrasound/MBs, and zero distance is inside the blood vessel where extravasation occurred. Each color represents one blood vessel in which extravasation occurred. MI = mechanical index; NPs = nanoparticles; NPMB = nanoparticle-stabilized microbubbles.

and 16/17 at MIs of 0.6 and 0.8, respectively, for NPMBs and 6/10 for Sonovue at an MI of 0.8).

A representative color map plot of mean fluorescence intensity as a function of both time after extravasation and distance from the blood vessel is provided in Supplementary Figure S4 (online only) for dextran (Supplementary Fig. S4a) and NPs (Supplementary Fig. S4b). Based on such color map plots, the intravascular intensity (Supplementary Figs. S5–S6) (online only), as well as the penetration and accumulation of NPs and dextran into the extravascular matrix (ROI in Supplementary Fig. S7) (online only), were determined (Figs. 5–8).

Interestingly, after extravasation, inside the blood vessels at the origin of extravasation, an immediate accumulation of dextran and NPs was observed followed by a slow decrease in dextran and NP fluorescence intensity. This effect occurred mainly at the higher MIs (0.8 and 0.4), whereas in some cases, for an MI of 0.2, dextran and NP fluorescence intensities inside blood vessels increased until the end of the treatment (Supplementary Figs. S5 and S6).

For both NPs and dextrans, there was a large variation in the extent of extravasation and subsequent penetration into the extracellular matrix between the individual extravasations, as illustrated in Figure 5 for NPMBs and in Figure 6 for Sonovue. The variation was more pronounced at MI = 0.8 for both MBs. Sonication at an MI of 0.8 induced more pronounced extravasation than sonication at the lower MIs, and in a few cases, it appeared immediately after a reduction or even full stop in blood flow, and change in blood flow direction occurred. The rate of penetration of both dextran and NPs into the extracellular matrix increased with increasing MI, as illustrated in Figures 5 and 6 for NPMBs and Sonovue, respectively. At an MI of 0.8 (for most cases), the penetration distance of the agents increased rapidly, as indicated by the steep initial slope (Figs. 5a, 5b and

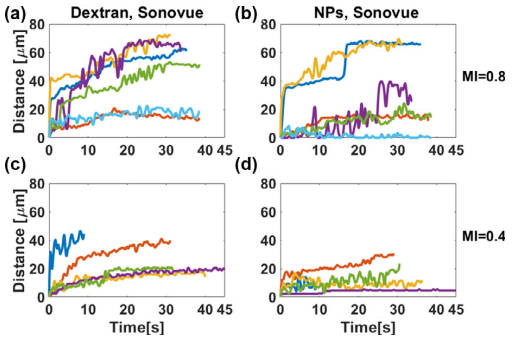

Fig. 6. Penetration of dextran and NPs for Sonovue at various MIs. MI = 0.8 for dextran (a) and NPs (b) (n = 6). MI = 0.4 for dextran (c) and NPs (d) (n = 5). Zero time corresponds to the time immediately before opening of the blood vessel by the ultrasound/MBs, and zero distance is inside the blood vessel where extravasation of agents occurred. Each color represents one blood vessel where extravasation occurred. MI = mechanical index; NPs = nanoparticles; NPMB = nanoparticle-stabilized microbubbles.

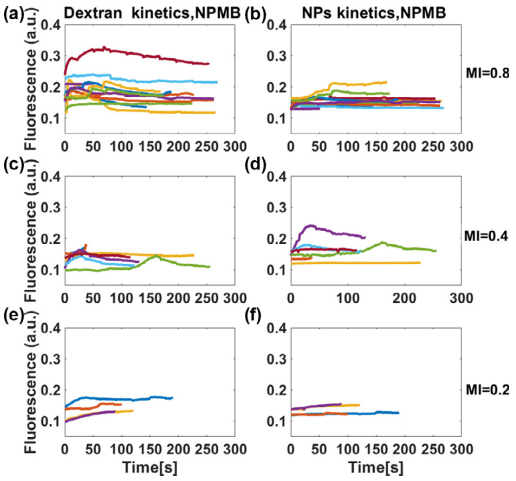

Fig. 7. Extravascular accumulation within 50 μm from the blood vessel of dextran and NPs as a function of time for NPMBs. MI = 0.8 for dextran (a) and NPs (b) (n = 12). MI = 0.4 for dextran (c) and NPs (d) (n = 7). MI = 0.2 for dextran (e) and NPs (f) (n = 4). Zero time corresponds to the time immediately before the extravasation. These curves are ratios to their respective maximum (whole image). Each color represents one blood vessel in which extravasation occurred. MI = mechanical index; NPs = nanoparticles; NPMB = nanoparticle-stabilized microbubbles.

6a, 6b). At the lower MIs (0.4 and 0.2) and at an MI of 0.4 using Sonovue, the rates of penetration of dextran and NPs were slower in most cases (Fig. 5c–f and 6c,

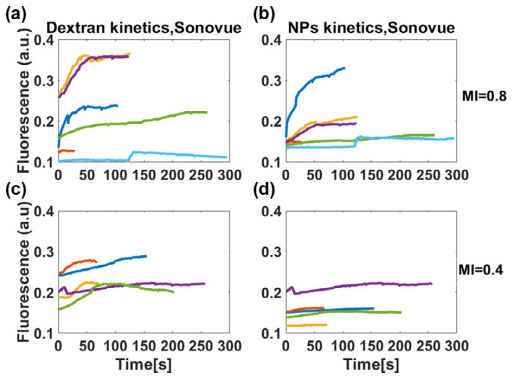

Fig. 8. Extravascular accumulation within 50 μm from the blood vessel of dextran and NPs as a function of time for Sonovue. MI = 0.8 for dextran (a) and NPs (b) (n = 6). MI = 0.4 for dextran (c) and NPs (d) (n = 5). Zero time corresponds to the time immediately before extravasation. These curves are ratios to their respective maximum (whole image). Each color represents one blood vessel where extravasation occurred. MI = mechanical index; NPs = nanoparticles; NPMB = nanoparticle-stabilized microbubbles.

6d). When rapid and deep penetration into the extracellular matrix occurred (as illustrated by the *purple curve* in Figure 5c (MI = 0.4) and the *blue curve* in Figure 5e (MI = 0.2), a large aggregate of NPs or NPMBs was present intravascularly immediately before the onset of extravasation. Representative images for such large aggregates are provided in Supplementary Figure S8 (online only, for MI = 0.4) and Figure 3a (for MI = 0.2).

The maximum penetration distances of the two agents within 40 s after the extravasation event varied considerably (Fig. 5 for NPMBs, Fig. 6 for Sonovue). At an MI of 0.8, the maximum penetration of dextran and NPs (in most of the extravasations) was in the ranges 38–70 and 23–70 μm, respectively, when NPMBs or Sonovue was injected (Figs. 5a, 5b and 6a, 6b).

At the lower MIs, when NPMBs were injected, the maximum penetration of dextran was in the ranges 34–77 and 38–46 μm at MIs of 0.4 and 0.2, respectively (Fig. 5c, 5e), while NPs penetrated in the ranges 16–77 μm at MI = 0.4 and 10–17 μm at MI = 0.2 (Fig. 5d, 5f). With Sonovue at MI = 0.4, the maximum penetration of dextran was in the range 31–46 μm, and for the NPs, it was in the range 17–30 μm (Fig. 6c, d).

Next, the accumulation of dextran and NPs within 50 μm of the blood vessel wall as a function of time was determined (Figs. 7 and 8) and exhibited a large variation between the individual extravasations. The extravascular mean fluorescence intensity increased with MI. For NPMBs at MIs of 0.8 and 0.4, the mean fluorescence intensity for dextran (for most extravasations) increased immediately after the onset of the extravasation and reached a peak before a gradual decrease in intensity was observed, whereas the NP fluorescence intensity increased more slowly in the beginning and leveled out thereafter (Fig. 7a, 7b). At an MI of 0.2, the increase in the mean intensity of both dextran and NPs was low (Fig. 7e, 7f). For Sonovue at MI = 0.8, both dextran and NPs exhibited a gradual increase in fluorescence intensity (in most cases) followed by a slow increase (Fig. 8a, 8b), whereas the increase was much less at MI = 0.4 (Fig. 8a, 8b and 7c, 7d).

Blood vessel diameter, branching point and extravasation

The vessel diameter was important for extravasation. At lower MIs (0.2–0.4), extravasation of NPs and dextran occurred in vessels with larger diameters as compared with that at MIs of 0.8 and 0.6 (Fig. 9a). Statistical analysis revealed significant differences between MIs of 0.8 and 0.2 and between MIs of 0.8 and 0.4 (Fig. 9a). Furthermore, for all MIs tested, 80% of the extravasation of NPs and dextran occurred at the vessel branching points, as outlined in Table 2, Figure 9b and Supplementary Videos S1 and S3 (online only). “At

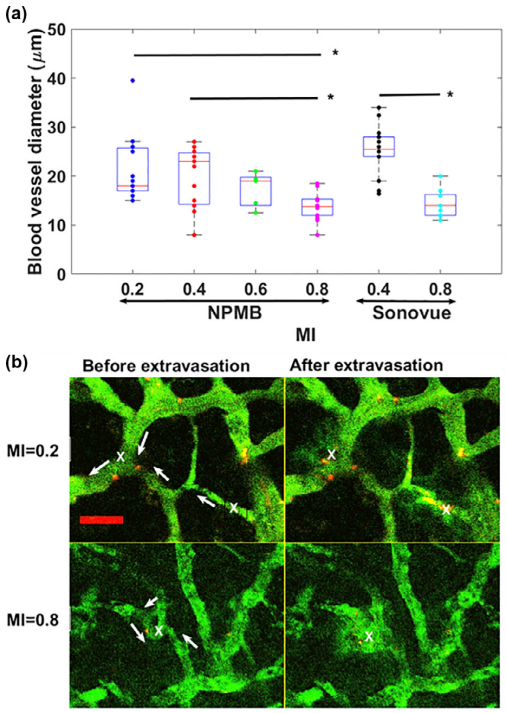

Fig. 9. (a) Blood vessel diameter versus MI. Both the data points and box-and-whisker plot are shown. Each circle represents one blood vessel in which extravasation was observed, and the *red line* in the box-and-whisker plot represents the median. For NPMBs at MI = 0.2 (n = 15), MI = 0.4 (n = 16), MI = 0.6 (n = 5) and MI = 0.8 (n = 17) and for Sonovue at MI = 0.4 (n = 15) and MI = 0.8 (n = 11). n is number of blood vessels. *Statistically significant difference between the groups. B) Examples of positions where extravasation occurred. *Arrows* indicate the flow direction, × indicates the position where extravasation occurred for MI = 0.2 (NPMBs) and MI = 0.8 (NPMBs). Bar = 50 μm. MI = mechanical index; NPs = nanoparticles; NPMB = nanoparticle-stabilized microbubbles.

vessel branching points" means a maximum of 9 μm from the vessel wall plus the radius of the vessel.

Change in blood flow caused by US and MBs

Before injection of MBs and application of US, a homogeneous FITC−dextran fluorescence signal was observed (Fig. 10a). During US exposure, many vessels exhibited heterogeneous and more granular FITC−dextran fluorescence signals (Fig. 10b). This appearance was more pronounced when the blood flow stopped and/or changed direction (Supplementary Video S3). We did not observe such effects in the control groups (without US) (Supplementary Videos S6 and S7). A reduction in mean fluorescence intensity inside the blood vessel was observed immediately when US was applied. This reduction increased with increasing MI and might be due to a slight change of focus of imaging caused by displacement of the tissue by acoustic radiation force.

The speed of NPs in untreated and US-treated tumors is illustrated in Figure 10c. Before application of US (controls), after injection of NPMBs, the speed was 117 ± 40 μm/s. When free NPs and Sonovue were injected, the speed was significantly lower, that is, 91 ± 30 μm/s. After US, the speed of NPs decreased by approximately 41%, 63% and 89% at MIs of 0.2, 0.4 and 0.8, respectively, for the NPMB groups, and by approximately 70% for both Sonovue groups. The difference between NP speed before US and that during US was statistically significant at all MIs and for both MBs. Moreover, statistical analysis revealed significant differences between all NPMB groups, but no significant difference between MIs of 0.4 and 0.8 for Sonovue groups.

Moreover, US combined with MBs altered the blood flow direction, as illustrated in Figure 10d and Supplementary Video S3. The percentage of occurrence of changes in blood flow direction for each group increased with MI (Fig. 10d). At the highest MI, approximately 50% of the recordings revealed a change in the flow direction. We did not observe any change in flow direction for the groups injected with Sonovue only and Sonovue plus free NPs without US.

Blood vessel damage caused by US and MBs

Histologic HES-stained sections were imaged and evaluated for US-induced damage by an experienced pathologist. In Figure 11 are representative images of tumors treated with Sonovue at an MI of 0.4 (Fig. 11a) and NPMBs at an MI of 0.8 (Fig. 11b). Microhemorrhages (extravasation of red blood cells out of the blood vessel) were observed at MI = 0.8 (Fig. 11c) in 2 of 5 mice in the NPMB group and 1 of 4 mice in the Sonovue group. No

Table 2. Numbers of extravasations that occurred at branching point of a blood vessel

	NPMBs				Sonovue		Total
	MI = 0.2	MI = 0.4	MI = 0.6	MI = 0.8	MI = 0.4	MI = 0.8	
At branching point	3	7	2	13	4	9	38
Not close to branching point	2	1	1	4	1	1	10

MI = mechanical index; NPMB = in-house-made microbubbles stabilized by polymeric nanoparticles.

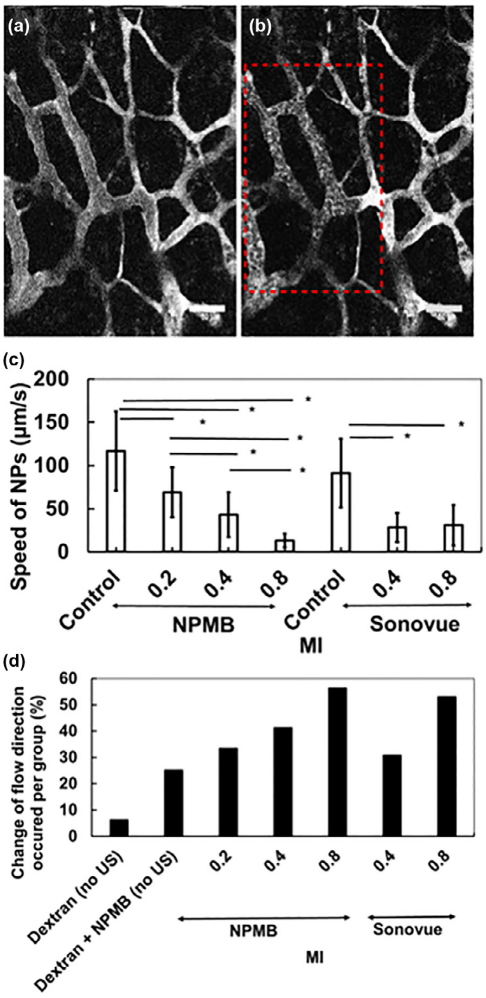

Fig. 10. Change in blood flow and speed of NPs. Representative image of homogenous fluorescein isothiocyanate–dextran signal intensity before (a) and after (b) US exposure. Change in blood flow rate and direction during US exposure (17.4 s after NPMB injection and US exposure). (c) Speed of the NPs as function of MI for control (no US) and during US for both NPMBs and Sonovue. (d) Percentage occurrence of change in blood flow direction observed per total recordings versus MI for both MBs. Results (c) are from four mice for NPMB control and three mice each for the other groups; error bars are for total number of particles analyzed. Results (d) are for n = 16 for dextran (no US), n = 4 for dextran + NPMB-US, n = 3 each for Sonovue (no US) and Sonovue + NPs, where n is number of animals. See Table 1 for NPMB + US and Sonovue + US groups for number of treatments in each group. *Statistically significant difference between the groups. Bar = 50 μm. MI = mechanical index; NPs = nanoparticles; NPMB = nanoparticle-stabilized microbubbles; US = ultrasound.

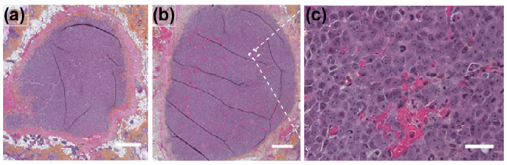

Fig. 11. Representative histologic sections from the OHS tumors grown in dorsal window chambers treated with MB and US stained with hematoxylin, erythrosine and saffron. (a) Treated at MI = 0.4. (b) Treated at MI = 0.8. (c) Higher-magnification image from the *white box* in (b). Images were taken at 10 × (a, b) and 40 × (c) magnification. Bar = 1 mm (a, b) and 50 μm (c).

severe vascular damage was observed *per se.* No hemorrhages were observed at the lower MIs (0 of 4 mice each at MI = 0.4 for NPMB and Sonovue groups, and 0 of 2 mice each at MI = 0.2 for NPMB and Sonovue groups).

DISCUSSION

Real-time imaging of US-induced effects on the vasculature and behavior of various molecules and nanoscale particles is a powerful method. Multiphoton imaging of the opening of the blood–brain barrier has previously been performed (Burgess et al. 2014; Cho et al. 2011; Raymond et al. 2007). However, to our knowledge, real-time imaging of US-induced extravasation of nanoscale agents in solid tumors *in vivo* has not been reported before. In our study, imaging the vasculature by intravital multiphoton microscopy during US sonication revealed extravasation of NPs and dextran, which indicates opening of the blood vessel. There was a correlation between blood vessel size where extravasation occurred and MI. Furthermore, the majority of the extravasations occurred at vessel branching points. Moreover, US-induced changes in flow rate and flow direction were observed, and occasionally, the blood flow stopped for short periods.

One interesting observation is that in most cases where extravasation occurred, it occurred close to vessel branching points. This could partly be due to the chaotic and disorganized tumor vessels, which had trifurcations and branches with uneven diameters (Fukumura and Jain 2007), and the fragility of the branching points. It has been reported that the organization of the vessels can create differences in sensitivity to sonication (Hu et al. 2012) and that branching points of the tumor vessels could be more susceptible to sonication. It was also reported that microdisruption occurred more often at branching points, which could be due to MBs being more easily trapped at such locations (Raymond et al. 2007). Moreover, the blood flow pattern is different at

the branching point (Malek et al. 1999). The flow might influence the number of bubbles in contact with endothelial cells and the average bubble−cell distance, which can enhance the interaction between the bubbles and endothelial cells.

The diameter of the blood vessel was also found to affect US-induced extravasation. After sonication at higher MIs (0.8 and 0.6), extravasation was typically observed in vessels with diameters of approximately 10−20 μm, whereas at lower MIs (0.2 and 0.4), the diameter ranged from 20−40 μm. Such a correlation between MI and vessel diameter has been reported in other studies (Nhan et al. 2013; Raymond et al. 2007). The boundary conditions imposed by the vessel wall influence the resonance frequency and the oscillation of a MB (Goertz 2015; Qin and Ferrara 2007; Sassaroli and Hynynen 2005). If the effect is a reduction in bubble resonance frequency compared with a free space situation and the bubble resonance frequency falls below the sonication frequency in the smallest vessels (diameter 10−20 μm), a higher MI will typically be required to obtain the same effect from cavitation. This requirement might explain why we did not observe extravasation in the smallest vessels, except at the highest MI.

Another interesting observation is that the extravasations appeared within milliseconds to minutes after the onset of US exposure, which indicates that the MBs could be present in the circulation for 5 min. However, we did not observe a higher number of extravasations immediately after the bolus injection when the MB concentration was highest. The differences in tumor characteristics, such as blood vessel density, branching, vessel organization and blood flow velocity (Wilhelm et al. 2016), can cause fluctuations in the amount of MBs in the target region, thereby affecting the onset time of the extravasation (Choi et al. 2014). Furthermore, there may not be adequate time for reperfusion between US pulses after the US destruction of the MBs, which occurs in a considerably larger region than the FOV.

Sonication at MI = 0.8 induced more violent extravasation and a higher number of extravasation events than that at lower MI. The main mechanism for this violent extravasation could be inertial cavitation, which occurs at higher peak negative pressures, as bubbles respond with a large and unstable expansion and, finally, a violent collapse (Kooiman et al. 2014). The opening of the blood vessel wall is most likely due to mechanical forces induced on the vessel wall during the oscillation of the MBs and subsequent collapse, causing shear forces and secondary effects, such as microstreaming, shock waves and jetting. At the lower MIs (0.4 and 0.2), in most cases, slower extravasation was observed. At lower MIs, stable volumetric oscillation of MBs might induce mechanical forces and acoustic streaming, resulting in shear stress on the vessel wall that can be sustained during the entire pulse duration (Kooiman et al. 2014). These mechanisms can create pores in the vessel wall, causing material to extravasate from the vessel. Larger shear stresses are reported to create larger pore sizes or more prolonged pore openings (Helfield et al. 2016). For monodisperse MBs, in the healthy vasculature of the brain, the opening volume is proportional to the acoustic pressure (Vlachos et al. 2011). This finding indicates that the shear stress may be larger at higher MIs than at lower MIs, and larger openings are probably created.

A large variation in penetration and accumulation into the extracellular matrix between individual extravasations was observed for both MBs and at all MIs applied. The reason might be owing mainly to the following factors: 1) The size differences in the pores created on the blood vessel wall caused by polydisperse MBs exerting different shear stresses on the blood vessel wall: The diameter of monodisperse MBs has been reported to correlate with the volume of blood−brain barrier opening in the healthy vasculature of the brain (Vlachos et al. 2011). In our study, both MBs are polydisperse populations, and for the NPMB, the excess of free NPs or the NPMBs can aggregate, increasing the polydispersity. 2) Blood flow velocity variability within and between tumors: This variation will not only affect the amount of MBs within the target region but also the amount of NPs (and, to a lesser extent, dextran) within the target region. In some cases, arrival of few NPs was observed in the region in which extravasation was observed. 3) Properties of the extracellular matrix, such as the heterogeneity in tumor cell density, interstitial fluid pressure and stromal content, might also influence the penetration of the agents.

A PRF of 0.5 Hz was initially chosen based on the velocity of blood in capillaries of mice, which is 2.03 ±1.42 mm/s (Unekawa et al. 2010), and our previous *in vivo* study (Snipstad et al. 2017). However, reducing the PRF from 0.5 to 0.1 Hz caused an increase in the number of extravasations at an MI of 0.8 when Sonovue was used and an MI of 0.4 when NPMBs were injected. With the higher PRF, MBs could possibly be destroyed before they reach the FOV, as the size of the −3-dB US beam is considerably larger than the FOV. Hence, new MBs would not replace the destroyed MBs, and subsequent US pulses would be ineffective. With a PRF of 0.1 Hz, the MBs get more time to replace the destroyed MBs before the next US pulse arrives, hence improving the interaction between US and MBs in the FOV.

The total numbers of extravasation events induced by the two MBs differed. It has been reported that the type of MB has a significant effect on cavitation activity (McMahon and Hynynen 2017; Wang et al. 2014a). When US and Sonovue are combined, considerably

fewer extravasations and numbers of blood vessels affected were observed in the FOV (during live imaging) compared with what was observed when US and NPMBs were combined. The difference in inducing extravasation is probably due to differences in the properties and behavior of the two MBs. The average diameter and concentration injected are quite similar for the two MBs. The size distributions of the two MBs are rather similar; however, the NPMBs are a small population with a diameter larger than 10 μm. In addition, the circulation half-time of the NPMBs is 1.5−2 times longer than that of Sonovue; hence, the amount of MBs reaching the tumor tissue could be different. The shell and gas core of the two MBs differ. NPMBs have an NP/protein shell and perfluoropropane core, whereas Sonovue has a lipid shell and sulfur hexafluoride (SF_6) core. The NP/protein shell is thicker and stiffer compared with the lipid shell, which is soft and elastic. The shell composition is important to the behavior of the MBs, and its importance was described in a study comparing Optison with a shell of denatured albumin and lipid-shelled Definity, where Optison induced greater destruction of the blood−brain barrier than Definity (McDannold et al. 2007). These researchers also suggest that the lipid-shelled Definity may be more difficult to break than Optison. However, our findings suggest that NPs/protein-shelled NPMBs may be more difficult to break than the lipid-shelled Sonovue and thus resilient at higher MIs. Therefore, the cavitation activity can persist longer for NPMBs than for Sonovue, causing more microstreaming and microjets affecting the capillary walls.

At an MI of 0.8, penetration of NPs into the extracellular matrix was faster for NPMBs than for Sonovue. This could be due to the presence of NPs on the bubble shell for the NPMBs which, upon violent destruction of MBs, are spread more efficiently than circulating particles (Burke et al. 2011a, 2014). Dextran penetrated faster than NPs for both MBs and at all MIs applied. The difference in the rate of penetration between NPs and dextran could be due to their sizes. The diameter of the NPs is approximately 160 nm, whereas the diameter of 2-MDa dextran is reported to be approximately 60 nm (Lammers et al. 2015). Moreover, the extravascular mean fluorescence intensity of dextran and NPs increases with MI, reflecting the correlation between MI and amount of NPs and dextrans extravasating.

Changes in blood flow rate and direction were also assessed from real-time imaging. Interestingly, changes in flow rate and direction were observed at all MIs applied, but the changes in both flow rate and direction were more pronounced at higher MI (0.8). As previously reported (Raymond et al. 2007), we observed heterogeneous and a granulation or streak of the FITC−dextran fluorescence in many vessels when the blood flow stopped and/or changed flow direction during US exposure. The black structures within the vessels in the heterogeneous FITC−dextran fluorescence could be red blood cells and became more apparent when the flow rate decreased. No changes in blood flow direction were observed during the 5 min of imaging after injection of Sonovue or Sonovue plus NPs before exposure to US. However, without US, the NP flow speed was significantly lower when injecting Sonovue plus free NPs than NPMBs (91 ± 30 μm/s vs. 117 ± 40 μm/s). However, the mechanisms responsible for change of flow during US are not fully understood. A reduction of blood velocity and perfusion caused by US combined with MBs (at 1-MHz peak negative pressure in the range 0.74−1.6 MPa) was also reported in previous studies (Burke et al. 2011b; Goertz et al. 2008, 2012). In these studies, the effects are associated with inertial cavitation (Goertz 2015). In our study, the change in blood flow was also found at an MI of 0.2, where inertial cavitation can be ruled out. This indicates that other mechanisms are involved. For example, (i) aggregation and activation of platelets can apparently occur very rapidly after an injury to the endothelial cells because of rapid destruction of MBs at the surface of tumor vasculature, which reduces the blood flow (Hu et al. 2012); and (ii) there might be significant cavitation activity going on in nearby arterioles outside the FOV that potentially can induce vasoconstriction and affect the flow within the FOV. The occurrence of vasoconstriction has been reported to induce a reduction and transiently stop blood flow (Raymond et al. 2007).

From histologic evaluation, the tissue was not damaged at MIs of 0.4 and 0.2, as also reported in our previous study (Snipstad et al. 2017). At an MI of 0.8, microhemorrhage was observed in the tumor tissue and was considered to be minimal. Similar effects have been reported previously for Sonovue at an MI of 0.8 (Wu et al. 2017). The microhemorrhages could be caused by the fragile neoangiogenic vessels of the tumors.

CONCLUSIONS

Multiphoton microscopy was used for real-time intravital imaging during US to investigate the effects of US and MBs in enhancing the permeability of tumor blood vessels and improving the delivery of NPs. Large variations in the rate and extent of penetration into the extracellular matrix were observed. Interestingly, at the higher MI, the extravasation occurred in smaller vessels and extravasation generally occurred close to vessel branching points. US also altered NP flow velocity and blood flow direction in an MI-dependent manner.

Results gained from intravital multiphoton microscopy help to elucidate the temporal and spatial extravasation of nanoscale particles during US exposure, which is highly useful in understanding the mechanisms underlying US-mediated delivery of NPs and optimizing them.

Acknowledgments—The authors are grateful to Spiros Kotopoulis for his assistance in designing the transducer cone, Anne Rein Hatletveit (SINTEF) for producing NPs and NPMBs and Annemieke Van Wamel for assisting in handling the animals. The project is supported by The Research Council of Norway (Project No. 240316). Additional funding from the Central Norway Regional Health Authority is much appreciated. Housing and care of animals were provided by the Comparative Medicine Core Facility (CoMed), and sectioning and HES staining were provided by the Cellular and Molecular Imaging Core Facility (CMIC), both at Norwegian University of Science and Technology (NTNU), funded by the Faculty of Medicine and Health Sciences at NTNU and Central Norway Regional Health Authority.

Conflict of interest disclosure—The authors declare no competing interests.

SUPPLEMENTARY DATA

Supplementary data related to this article can be found online at doi:10.1016/j.ultrasmedbio.2019.07.683.

REFERENCES

Anchordoquy TJ, Barenholz Y, Boraschi D, Chorny M, Decuzzi P, Dobrovolskaia MA, Farhangrazi ZS, Farrell D, Gabizon A, Ghandehari H, Godin B, La-Beck NM, Ljubimova J, Moghimi SM, Pagliaro L, Park JH, Peer D, Ruoslahti E, Serkova NJ, Simberg D. Mechanisms and barriers in cancer nanomedicine: Addressing challenges, looking for solutions. ACS Nano 2017;11:12–18.

Antonios NP, James JC. Superharmonic microbubble Doppler effect in ultrasound therapy. Phys Med Biol 2016;61:6154.

Åslund AKO, Berg S, Hak S, Mørch Ý, Torp SH, Sandvig A, Widerøe M, Hansen R, Davies CDL. Nanoparticle delivery to the brain—By focused ultrasound and self-assembled nanoparticle-stabilized microbubbles. J Control Release 2015;220:287–294.

Boissenot T, Bordat A, Fattal E, Tsapis N. Ultrasound-triggered drug delivery for cancer treatment using drug delivery systems: From theoretical considerations to practical applications. J Control Release 2016;241:144–163.

Burgess A, Nhan T, Moffatt C, Klibanov AL, Hynynen K. Analysis of focused ultrasound-induced blood–brain barrier permeability in a mouse model of Alzheimer's disease using two-photon microscopy. J Control Release 2014;192:243–248.

Burke CW, Hsiang YHJ, Alexander IVE, Kilbanov AL, Price RJ. Covalently Linking poly(lactic-co-glycolic acid) nanoparticles to microbubbles before intravenous injection improves their ultrasound-targeted delivery to skeletal muscle. Small 2011a;7:1227–1235.

Burke CW, Klibanov AL, Sheehan JP, Price RJ. Inhibition of glioma growth by microbubble activation in a subcutaneous model using low duty cycle ultrasound without significant heating. J Neurosurg 2011b;114:1654–1661.

Burke CW, Alexander E, Timbie K, Kilbanov AL, Price RJ. Ultrasound-activated agents comprised of 5 FU-bearing nanoparticles bonded to microbubbles inhibit solid tumor growth and improve survival. Mol Ther 2014;22:321–328.

Carpentier A, Canney M, Vignot A, Reina V, Beccaria K, Horodyckid C, Karachi C, Leclercq D, Lafon C, Chapelon JY, Capelle L, Cornu P, Sanson M, Hoang-Xuan K, Delattre JY, Idbaih A. Clinical trial of blood–brain barrier disruption by pulsed ultrasound. Sci Transl Med 2016;8:343. re2.

Caskey CF, Stieger SM, Qin S, Dayton PA, Ferrara KW. Direct observations of ultrasound microbubble contrast agent interaction with the microvessel wall. J Acoust Soc Am 2007;122:1191–1200.

Chen H, Brayman AA, Bailey MR, Matula TJ. Blood vessel rupture by cavitation. Urol Res 2010;38:321–326.

Chen H, Kreider W, Brayman AA, Bailey MR, Matula TJ. Blood vessel deformations on microsecond time scales by ultrasonic cavitation. Phys Rev Lett 2011;106 034301.

Cho EE, Drazic J, Ganguly M, Stefanovic B, Hynynen K. Two-photon fluorescence microscopy study of cerebrovascular dynamics in ultrasound-induced blood–brain barrier opening. J Cereb Blood Flow Metab 2011;31:1852–1862.

Choi JJ, Carlisle RC, Coviello C, Seymour L, Coussios CC. Non-invasive and real-time passive acoustic mapping of ultrasound-mediated drug delivery. Phys Med Biol 2014;59:4861–4877.

Coates A, Abraham S, Kaye SB, Sowerbutts T, Frewin C, Fox RM, Tattersall MHN. On the receiving end—Patient perception of the side-effects of cancer chemotherapy. Eur J Cancer Clin Oncol 1983;19:203–208.

Dayton P, Klibanov A, Brandenburger G, Ferrara K. Acoustic radiation force in vivo: A mechanism to assist targeting of microbubbles. Ultrasound Med Biol 1999;25:1195–1201.

Dimcevski G, Kotopoulis S, Bjånes T, Hoem D, Schjøtt J, Gjertsen BT, Biermann M, Molven A, Sorbye H, McCormack E, Postema M, Gilja OH. A human clinical trial using ultrasound and microbubbles to enhance gemcitabine treatment of inoperable pancreatic cancer. J Control Rel 2016;243:172–181.

Eggen S, Fagerland SM, Mørch Ý, Hansen R, Søvik K, Berg S, Furu H, Bøhn AD, Lilledahl MB, Angelsen A, Angelsen B, Davies CDL. Ultrasound-enhanced drug delivery in prostate cancer xenografts by nanoparticles stabilizing microbubbles. J Control Rel 2014;187:39–49.

Fodstad Ø, Brøgger A, Bruland Ø, Solheim OP, Nesland JM, Pihl A. Characteristics of a cell line established from a patient with multiple osteosarcoma, appearing 13 years after treatment for bilateral retinoblastoma. Int J Cancer 1986;38:33–40.

Fukumura D, Jain RK. Tumor microenvironment abnormalities: Causes, consequences, and strategies to normalize. J Cell Biochem 2007;101:937–949.

Garbin V, Cojoc D, Ferrari E, Di Fabrizio E, Overvelde MLJ, van der Meer SM, de Jong N, Lohse D, Versluis M. Changes in microbubble dynamics near a boundary revealed by combined optical micromanipulation and high-speed imaging. Appl Phys Lett 2007;90 114103.

Goertz DE. An overview of the influence of therapeutic ultrasound exposures on the vasculature: High intensity ultrasound and microbubble-mediated bioeffects. Int J Hyperthermia 2015;31:134–144.

Goertz DE, Karshafian R, Hynynen K. Antivascular effects of pulsed low intensity ultrasound and microbubbles in mouse tumors. Proc IEEE Int Ultrason Symp 2008;670–673.

Goertz DE, Todorova M, Mortazavi O, Agache V, Chen B, Karshafian R, Hynynen K. Antitumor effects of combining docetaxel (Taxotere) with the antivascular action of ultrasound stimulated microbubbles. PLoS One 2012;7:e52307.

Hak S, Reitan NK, Haraldseth O, Davies CDL. Intravital microscopy in window chambers: A unique tool to study tumor angiogenesis and delivery of nanoparticles. Angiogenesis 2010;13:113–130.

Helfield BL, Leung BYC, Goertz DE. The effect of boundary proximity on the response of individual ultrasound contrast agent microbubbles. Phys Med Biol 2014;59:1721–1745.

Helfield B, Chen X, Watkins SC, Villanueva FS. Biophysical insight into mechanisms of sonoporation. Proc Natl Acad Sci USA 2016;113:9983.

Hernot S, Klibanov AL. Microbubbles in ultrasound-triggered drug and gene delivery. Adv Drug Deliv Rev 2008;60:1153–1166.

Hu X, Kheirolomoom A, Mahakian LM, Beegle JR, Kruse DE, Lam KS, Ferrara KW. Insonation of targeted microbubbles produces regions of reduced blood flow within tumor vasculature. Invest Radiol 2012;47:398–405.

Hynynen K, McDannold N, Vykhodtseva N, Jolesz FA. Noninvasive MR imaging−guided focal opening of the blood−brain barrier in rabbits. Radiology 2001;220:640–646.
Klymchenko AS, Roger E, Anton N, Anton H, Shulov I, Vermot J, Mely Y, Vandamme TF. Highly lipophilic fluorescent dyes in nano-emulsions: Towards bright non-leaking nano-droplets. RSC Adv 2012;2:11876–11886.
Kooiman K, Vos HJ, Versluis M, de Jong N. Acoustic behavior of microbubbles and implications for drug delivery. Adv Drug Deliv Rev 2014;72:28–48.
Kotopoulis S, Delalande A, Popa M, Mamaeva V, Dimcevski G, Gilja OH, Postema M, Gjertsen BT, McCormack E. Sonoporation-enhanced chemotherapy significantly reduces primary tumour burden in an orthotopic pancreatic cancer xenograft. Mol Imaging Biol 2014;16:53–62.
Lammers T, Kiessling F, Hennink WE, Storm G. Drug targeting to tumors: Principles, pitfalls and (pre-) clinical progress. J Control Release 2012;161:175–187.
Lammers T, Koczera P, Fokong S, Gremse F, Ehling J, Vogt M, Pich A, Storm G, van Zandvoort M, Kiessling F. Theranostic USPIO-loaded microbubbles for mediating and monitoring blood−brain barrier permeation. Adv Funct Mater 2015;25:36–43.
Lammertink B, Bos C, Deckers R, Storm G, Moonen C, Escoffre JM. Sonochemotherapy: From bench to bedside. Front Pharmacol 2015;6:138.
Liu HL, Hua MY, Chen P-Y, Chu PC, Pan CH, Yang HW, Huang CY, Wang JJ, Yen TC, Wei KC. Blood−brain barrier disruption with focused ultrasound enhances delivery of chemotherapeutic drugs for glioblastoma treatment. Radiology 2010;255:415–425.
Maeda H, Wu J, Sawa T, Matsumura Y, Hori K. Tumor vascular permeability and the EPR effect in macromolecular therapeutics: A review. J Control Rel 2000;65:271–284.
Mainprize T, Lipsman N, Huang Y, Meng Y, Bethune A, Ironside S, Heyn C, Alkins R, Trudeau M, Sahgal A, Perry J, Hynynen K. Blood−brain barrier opening in primary brain tumors with non-invasive MR-guided focused ultrasound: A clinical safety and feasibility study. Sci Rep 2019;9:321.
Malek AM, Alper SL, Izumo S. Hemodynamic shear stress and its role in atherosclerosis. JAMA 1999;282:2035–2042.
McDannold N, Vykhodtseva N, Hynynen K. Use of ultrasound pulses combined with Definity for targeted blood−brain barrier disruption: A feasibility study. Ultrasound Med Biol 2007;33:584–590.
McMahon D, Hynynen K. Acute inflammatory response following increased blood−brain barrier permeability induced by focused ultrasound is dependent on microbubble dose. Theranostics 2017;7:3989–4000.
Mullick Chowdhury S, Lee T, Willmann JK. Ultrasound-guided drug delivery in cancer. Ultrasonography 2017;36:171–184.
Mørch Ý, Hansen R, Berg S, Åslund AKO, Glomm WR, Eggen S, Schmid R, Johnsen H, Kubowicz S, Snipstad S, Sulheim E, Hak S, Singh G, McDonagh BH, Blom H, Davies CDL, Stenstad PM. Nanoparticle-stabilized microbubbles for multimodal imaging and drug delivery. Contrast Media Mol Imaging 2015;10:356–366.
Nhan T, Burgess A, Cho EE, Stefanovic B, Lilge L, Hynynen K. Drug delivery to the brain by focused ultrasound induced blood−brain barrier disruption: Quantitative evaluation of enhanced permeability of cerebral vasculature using two-photon microscopy. J Control Release 2013;172:274–280.
Qin S, Ferrara KW. The natural frequency of nonlinear oscillation of ultrasound contrast agents in microvessels. Ultrasound Med Biol 2007;33:1140–1148.
Raymond SB, Skoch J, Hynynen K, Bacskai BJ. Multiphoton imaging of ultrasound/Optison mediated cerebrovascular effects in vivo. J Cereb Blood Flow Metab 2007;27:393–403.
Sassaroli E, Hynynen K. Resonance frequency of microbubbles in small blood vessels: A numerical study. Phys Med Biol 2005;50:5293–5305.
Schneider M. Characteristics of SonoVue™. Echocardiography 1999;16:743–746.
Snipstad S, Berg S, Mørch Ý, Bjørkøy A, Sulheim E, Hansen R, Grimstad I, van Wamel A, Maaland AF, Torp SH, Davies CDL. Ultrasound improves the delivery and therapeutic effect of nanoparticle-stabilized microbubbles in breast cancer xenografts. Ultrasound Med Biol 2017;43:2651–2669.
Sulheim E, Kim J, van Wamel A, Kim E, Snipstad S, Vidic I, Grimstad IH, Widerøe M, Torp SH, Lundgren S, Waxman DJ, Davies CDL. Multi-modal characterization of vasculature and nanoparticle accumulation in five tumor xenograft models. J Control Release 2018;279:292–305.
Tannock IF, Lee CM, Tunggal JK, Cowan DSM, Egorin MJ. Limited penetration of anticancer drugs through tumor tissue. Clin Cancer Res 2002;8:878.
Treat LH, McDannold N, Zhang Y, Vykhodtseva N, Hynynen K. Improved anti-tumor effect of liposomal doxorubicin after targeted blood−brain barrier disruption by MRI-guided focused ultrasound in rat glioma. Ultrasound Med Biol 2012;38:1716–1725.
Unekawa M, Tomita M, Tomita Y, Toriumi H, Miyaki K, Suzuki N. RBC velocities in single capillaries of mouse and rat brains are the same, despite 10-fold difference in body size. Brain Res 2010;1320:69–73.
van Wamel A, Sontum PC, Healey A, Kvåle S, Bush N, Bamber J, de Lange Davies C. Acoustic Cluster Therapy (ACT) enhances the therapeutic efficacy of paclitaxel and Abraxane for treatment of human prostate adenocarcinoma in mice. J Control Rel 2016;236:15–21.
Vlachos F, Tung YS, Konofagou E. Permeability dependence study of the focused ultrasound-induced blood−brain barrier opening at distinct pressures and microbubble diameters using DCE-MRI. Magn Reson Med 2011;66:821–830.
Wang S, Samiotaki G, Olumolade O, Feshitan JA, Konofagou EE. Microbubble type and distribution dependence of focused ultrasound-induced blood−brain barrier opening. Ultrasound Med Biol 2014a;40:130–137.
Wang TY, Wilson KE, Machtaler S, Willmann JK. Ultrasound and microbubble guided drug delivery: Mechanistic understanding and clinical implications. Curr Pharm Biotechnol 2014b;14:743–752.
Wang TY, Choe JW, Pu K, Devulapally R, Bachawal S, Machtaler S, Chowdhury SM, Luong R, Tian L, Khuri-Yakub B, Rao J, Paulmurugan R, Willmann JK. Ultrasound-guided delivery of microRNA loaded nanoparticles into cancer. J Control Release 2015;203:99–108.
Wei KC, Chu PC, Wang HYJ, Huang CY, Chen PY, Tsai HC, Lu YJ, Lee PY, Tseng IC, Feng LY, Hsu PW, Yen TC, Liu HL. Focused ultrasound-induced blood−brain barrier opening to enhance temozolomide delivery for glioblastoma treatment: A preclinical study. PLoS One 2013;8:e58995.
Wilhelm S, Tavares AJ, Dai Q, Ohta S, Audet J, Dvorak HF, Chan WC. Analysis of nanoparticle delivery to tumours. Nat Rev Mater 2016;1:16014.
Wu SK, Chu PC, Chai WY, Kang ST, Tsai CH, Fan CH, Yeh CK, Liu HL. Characterization of different microbubbles in assisting focused ultrasound-induced blood−brain barrier opening. Sci Rep 2017;7:46689.

SUPPLEMENTARY DATA

Image processing

Images were analyzed in ImageJ (National Institutes of Health, Bethesda, MD, USA) and MATLAB (MathWorks, Natick, MA, USA). The first frame (Fig. S1A) was used to create a vessel mask using automatic segmentation. Examples of such images are shown in Fig. S1. Fig. S1A represents the first frame image from the dextran signal, and Fig. S1B shows a vessel mask created.

Penetration kinetics of dextran and NPs into the extracellular matrix

To evaluate the penetration and distribution of the NPs and dextran into the extracellular matrix, the video frame averaging three consecutive images (compromising the temporal resolution and the quality of the image) were used. First, the blood vessels were masked, and subsequently, a circular ROI with radius equal to the vessel was drawn followed by concentric circles around the vessel spaced by 3 pixels (2.23 μm) from the blood vessel wall until reaching approximately 60 to 100 μm in depth in the extracellular matrix (Fig. S2). Inside the blood vessel and within the concentric rings, the mean fluorescence intensity values of dextran and NPs as a function of depth and time were computed as shown in Fig. S3.

From these mean fluorescence intensities, the penetration of the two agents was computed by registering the distance and time at which the mean signal intensity was greater than 10% of the background intensity value and are depicted in Fig. 5-6

Intravascular accumulation

Representative images indicating the ROIs are shown in Fig. S4. The mean fluorescence intensity of dextran and NPs as a function of time were computed (Fig. S5-S6 and Fig. 7-8). Figs. S5 and S6 show the intravascular, whereas the extravascular accumulation of dextran and NPs were shown in Figs 7 and 8, respectively.

Large NPMB or aggregate NPs

Fig. S7 shows the presence of large MB or aggregate NPs in the region of the vessel immediately before extravasation (t=0). The tumor was exposed to MI of 0.4, and the figure shows how the NPMB/aggregates of NPs are increasing and extravasating during the first minutes of US. These images correspond to the extravasation accumulation shown by the cyan color curve in Fig. 5C.

Supplementary movies

Examples of video recorded by intravital microcopy in real time during US. The video shows a composite image of both dextran (green) and NP (red) channels. To enhance the quality of the images, video frame averaging fifteen consecutive images was performed, and image brightness was adjusted to aid visualization of the two agents. The first 5 videos show the onset of extravasations as well as the penetration and distribution of dextran and NPs into the extracellular matrix after the blood vessel opening. In addition, the videos also demonstrate changes in the blood flow rate and direction after US was applied. Treatment started immediately after injection of MBs. The last two videos are controls without US.

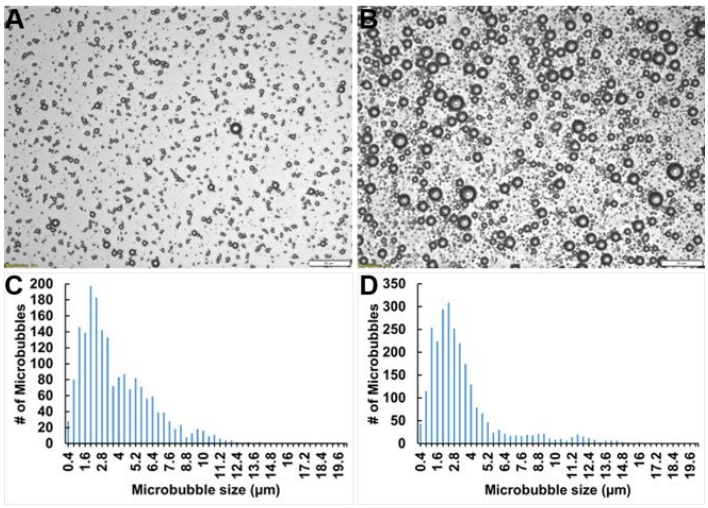

Fig. S1. MB sizing using microscopy. Typical bright field optical microscope image of: A) Sonovue suspension, and B) NPMB suspension. Histogram illustrating the size distribution as: C) number of particles of Sonovue, and D) number of particles of NPMB. Scale bar = 50 μm.

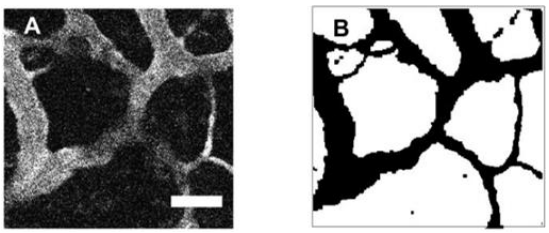

Fig. S2. (A) Representative image from dextran signal used for creating the vessel mask. (B) Resulting vessel mask. Scale bare=50 μm.

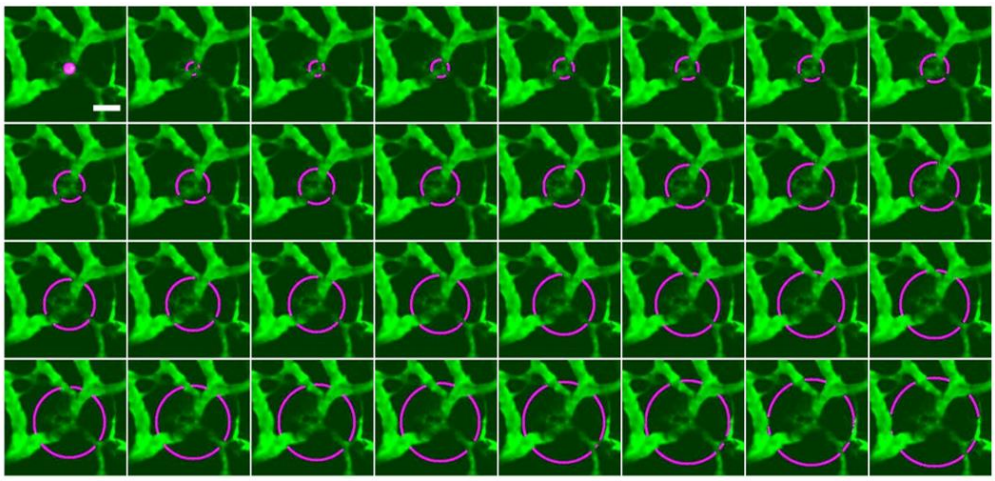

Fig. S3. Representative images showing the circular ROI inside the blood vessel and concentric circle ROIs (outside the blood vessel) spacing 3 pixels (2.23 µm) from the blood vessel wall until 60 to 100 µm into the interstitium. The mean fluorescence intensity within each ROIs were computed. Scale bar = 50 µm.

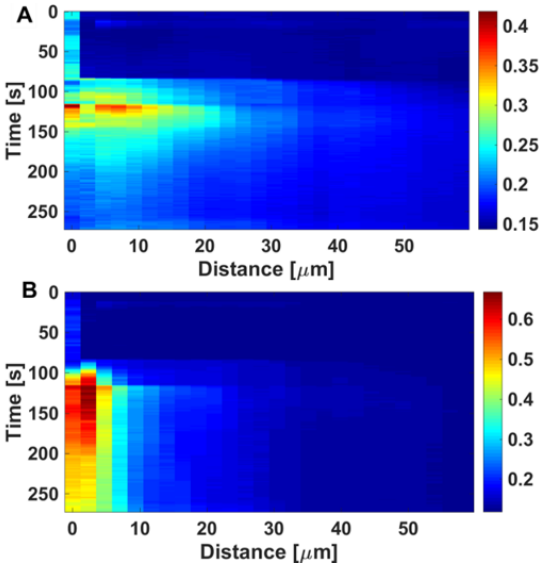

Fig. S4. Representative color map plot of mean fluorescence intensity as a function of both time and distance from the blood vessel for NPMBs at MI 0.8.:- (A) for dextran and (B) for NPs. Similar plots were drawn for all data presented in Fig. 5-6.

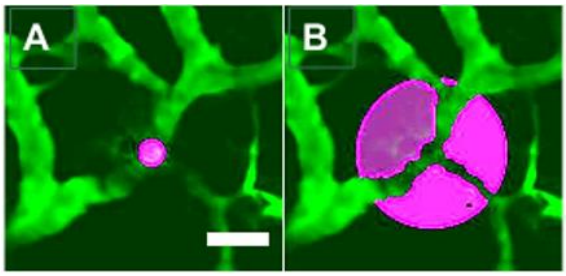

Fig. S5. Representative images showing circular ROI: (A) inside the blood vessel and (B) within 50 µm from the blood vessel surface (extravascular accumulation). Scale bar = 50 µm.

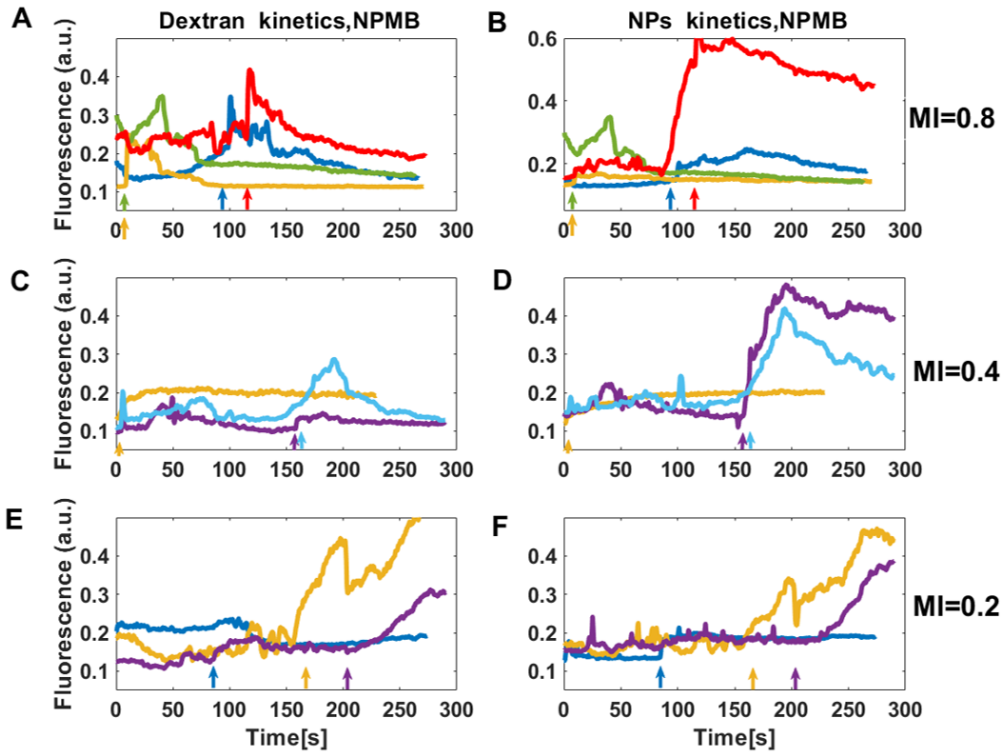

Fig. S6. Representative plots of intravascular accumulation of dextran and NPs as function of time for various MIs for NPMB. MI=0.8 for dextran (A) and NPs (B) (n=4), MI=0.4 for dextran (C) and NPs (D) (n=3), and MI=0.2 for dextran (E) and NPs (F) (n=3). Zero time corresponds to the time where imaging started. The colored arrows indicate the onset of extravasation for each curve with corresponding color code. These curves are ratio to their respective maximum (of the whole image). Each color represents one blood vessel where extravasation occurred.

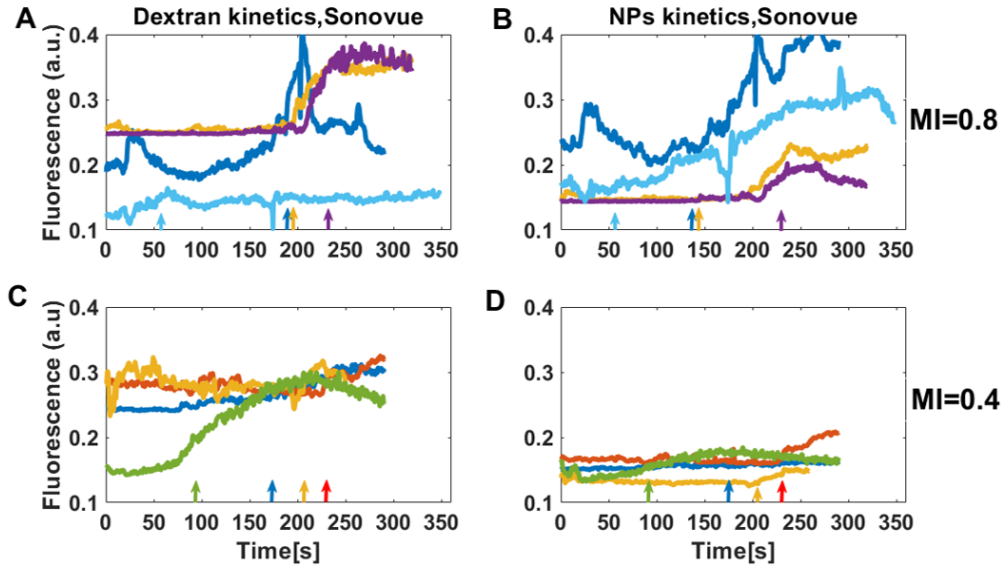

Fig. S7. Representative plots of intravascular accumulation of dextran and NPs as function of time for various MIs for Sonovue. MI=0.8 for dextran (A) and NPs (B) (n=4), and MI=0.4 for dextran (C) and NPs (D) (n=4). Zero time corresponds to the time where imaging started. The colored arrows in x-axis indicate the onset of extravasation for each curve with corresponding color code. These curves are ratio to their respective maximum (whole image). Each color represents one blood vessel where extravasation occurred.

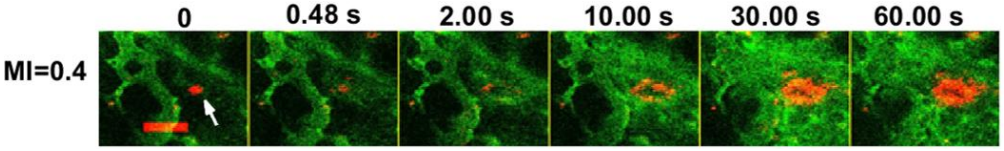

Fig. S8. Examples of extravasation and distribution of NPs (red) and dextran (green) as a function of time after opening of the blood vessel wall by US and MB with MI 0.4 to illustrate NPMB or aggregate of NPs at the vessel site immediately before onset of extravasation. The arrow indicates the large MB or aggregated NP. Zero time represents to the time immediately before opening of the vessel. Scale bar = 50 µm.

Paper II

This paper is in preparation for publication.

Due to awaiting publication this paper is not included in NTNU Open

Paper III

Paper IV

This paper is in preparation for publication.

Due to awaiting publication this paper is not included in NTNU Open